GROWTH AND REMODELING IN ENGINEERED SOFT TISSUE

by

Joseph E. Olberding

A dissertation submitted in partial fulfillment
of the requirements for the degree of
Doctor of Philosophy
(Biomedical Engineering)
in The University of Michigan
2010

Doctoral Committee:

        Associate Professor Krishnakumar R. Garikipati, Co-Chair
        Professor Karl Grosh, Co-Chair
        Professor Ellen M. Arruda
        Professor Scott J. Hollister
        Associate Research Professor Lisa M. Larkin

"Everything should be made as simple as possible, but not simpler."

— Albert Einstein, on Occam's Razor

ACKNOWLEDGEMENTS

Unlike many doctoral students, I have had the unique privilege of working with multiple mentors from my very first day in Ann Arbor. My co-chairs are Krishna Garikipati, Ph.D. and Karl Grosh, Ph.D., but from day one I felt part of the family along with Ellen M. Arruda, Ph.D in our growth and remodeling mechanics group. I consider myself lucky to have in them approachable, accessible, patient, flexible, down-to-earth, funny, and crazy-smart supervisors. It is no accident that we were all on the same page almost without exception. The same goes for Lisa M. Larkin, Ph.D., who later welcomed me into her Skeletal Tissue Engineering Laboratory (STEL) when my cell and tissue culture work became full-swing. Their insight, support and motivation have made my time at the University of Michigan quite likely the most *intellectually* enjoyable and stimulating six years of my life. I thank Prof. Scott Hollister, Ph.D. for his scope and depth of knowledge as well as his diligent

my six years in Ann Arbor. More than a few were established immediately during recruitment weekend before even deciding on Michigan. As a son of the Midwest leaving my singular undergraduate experience in New Orleans, I absolutely did not expect that I would be echoing more than one of my fellow UM graduate students when I say that these were some of the most *personally* enjoyable and fun years of my life. Few of my undergraduate classmates have said the same about their postgraduate studies.

Finally, I thank my parents Donna and Ed Olberding and sister Emily for their unwavering love and steadfast support for my doctoral studies. I said this six years ago when finishing my master's thesis, but I truly believe that without them my persistent efforts would not be possible. I thank God for them and all those who helped me reach this milestone.

TABLE OF CONTENTS

LIST OF FIGURES

Figure

LIST OF TABLES

LIST OF ABBREVIATIONS

Abbreviation

CHAPTER 1

Introduction

This initial chapter provides some context for this work (§1.1–§1.5) and an overview of the topics considered in the remainder of the dissertation (§1.6).

1.1 Clinical perspectives

Left to their own devices, the parallel-fibered ligaments and tendons repair slowly due to characteristically low blood flow and cell content [210]. Taking the case of anterior cruciate ligament (anterior cruciate ligament (ACL)) rupture, even in contrast to medial collateral ligament (MCL) injury [162, 185, 207], no stable blood clot can form to constitute the necessary scaffold for fibroblasts to bridge the torn ends [69]. Together, ACL and MCL injuries constitute 90 % of sports-related ligament injuries [121]. Indeed, the ACL is the most frequently injured knee ligament, with some 200,000 ruptures [150] and 100,000 surgical reconstructions per year in the United States [146], and a panel of associated sequelae, the most debilitating of which is tibiofemoral osteoarthritis (OA). While recent studies suggest OA rates in those with isolated ACL injury may be only be 0 %–13 % (lower than previously thought) [134], OA may develop regardless of treatment strategy [109]. One study reported infrequent OA among ACL rupture patients with an intact meniscus treated with activity modification and physical therapy [130]. Not surprisingly, however, patients actively engaged in sports prior to injury but who choose a conservative

neuromuscular rehabilitation program in place of surgery are relatively dissatisfied with quality of life outcomes at 15 years [93]. These morbidities are only partially resolved by the use of surgical autologous tendon graft repair, be it donor-site morbidity, inferior mechanical knee stability (compared to pre-injury), or insufficient secretory potential of re-populating cartilage cells. Taken together, these issues motivate an alternative 'autologous' intervention strategy. However, like other tissues to date, engineered ligaments have been inferior in terms of mechanical properties [62]. Without the possible drawbacks of bio-incompatibility or implant resorption, an approach which does not use an exogenous biological or synthetic scaffold may yield superior long-term stiffness and strength [21, 65, 73, 92, 97, 100, 110, 179].

Almost by definition, ligament tissue engineering requires fibroblastic cells. Bone marrow stromal cells (MSCs) are ideal for this purpose, as they contain a sub-fraction of *mesenchymal stem cells* and (mesenchymal progenitor cells (MPCs)) multipotent to non-epithelial connective tissues [22, 57], are readily available as autologous, immunocompatible iliac crest aspirates in the adult [156], and, based on clinical precedent, do not challenge any ethical or safety norms. Moreover, due to the immunocompatible properties of mesenchymal stem cells [81], MSCs may be uniquely suitable as an "off-the-shelf" allograft. Through a variety of proposed mechanisms, they also appear to be immunosuppressive, leading to enhanced allogenic hematopoietic stem cell engraftment and inhibition of graft-versus-host-disease [101]. Compare this to primary fibroblasts, which, while not only having less proliferative and differentiation potential than most MSCs [55], require a solid-tissue biopsy (skin, tendon, ligament, etc.) for use as a cell-based therapy. Intuitively, MSCs are inherently more able than differentiated fibroblasts to restore the *biochemical* role of the native ligament in order to provide the necessary paracrine signaling for healthy repair of the entire

joint and delay the onset of OA. MSC biology research and the tissue engineering efforts it feeds, however, have focused on the osteo-chondrogenic differentiation axis of the MPC sub-population [103] and, more recently, on the evidence of these cells to exhibit germ-layer plasticity [9] in neurogenesis [17, 119]. Rat MSCs have been used to engineer self-assembling, scaffold-less 3-D constructs with both fibrogenic and osteogenic properties in the Skeletal Tissue Engineering Laboratory (STEL) [110, 179, 189]. However, it has been difficult to produce a homogenous ligament repeatably due to the donor-variable and heterogeneous nature of MSC cultures. In this context, phenotypic characterization and long-term *in vitro* and *in vivo* studies are necessary in order to rule out the possibility of a "default" osteogenic phenotype in isolated MSCs, the existence of which would render any related engineered ligament construct physiologically inappropriate and potentially debilitating if ectopic mineralization were to occur.

Finally, there is in the tissue engineering community growing recognition that the "mathematics of morphogenesis" is "a waypoint to better implants" [172]. However, only recently have the necessary numerical methods and associated computational systems existed to enable the practical solution of modeling problems that possess a level of complexity germane to the next generation of implants: those which rely on the body's own ability to replace diseased or injured tissue and restore function. It is therefore important that biological processes be mathematically formulated and computationally implemented in a practical and integrated fashion commensurate with the interdisciplinary nature of tissue engineering and regenerative medicine. The phenomenon of stem cell differentiation resulting from its chemo-mechanical environment is no exception, and its incorporation into a multi-physics computational model would represent a non-trivial step toward the vision of '*in silico* bioreactors'

3

for individual patient design of engineered tissue.

1.2 Marrow stromal cell biology and culture

Though interpretations of the term abound, stem cells are commonly defined by the possession of two properties: *self-renewability*, the capacity to divide indefinitely such that at least one daughter cell is no more differentiated than the parent; and *multipotency*, the ability for progeny to assume more than one distinct phenotype upon terminal differentiation [216]. In the adult mammal, stem cells reside in organs and are effectively inseparable (both physically and conceptually) from their *niche*, a tissue-specific protective microenvironment that provides the soluble and insoluble signals to maintain the "stemness" of these precursor cells and regulate their release for massive differentiation in tissue repair. Here, the definition will be made that MPCs refer to those *dividing cells which have lost their self-renewal property, but still have demonstrated multipotency.* The use of the terms MSC or MPC will be made as precise as possible.

1.2.1 Isolation and characterization

The first direct *ex vivo* evidence for the role of adult bone marrow as a niche for anchorage-dependent, non-hematopoietic, MPCs is credited to Friedenstein et al. [53], who isolated the sub-population by its adherence to tissue culture plastic (TCP) while hematopoietic cells remained in suspension. The adherent MSCs were heterogeneous in morphology, and, when plated from a low-density single-cell suspension, clonogenic colonies emerged that were fibroblast-like in appearance (i.e., spindle or bipolar-shaped), and were termed colony forming unit-fibroblasts (CFU-Fs). These same CFU-F colonies were capable of multiple mesenchymal lineages as evidenced by staining positive for both bone and adipose tissue [54].

Plastic adherence and mass density

The essence of Friedenstein et al. [53]'s isolation method is utilized by almost all labs today, as the majority of unwanted cells are removed according to this plastic adherence principle. The cell content of bone marrow aspirate contains mostly erythrocytes (red blood cells), thrombocytes (platelets), and leukocytes (white blood cells) separate from the non-hematopoietic fraction. The latter population is morphologically, immunologically, and functionally heterogeneous and includes mature adipocytes and endothelial cells, as well as a multipotent subpopulation [166]. MSCs and their MPCs are rare: Bruder et al. [19] reported human MPCs at 1 in 10^5 or an order of magnitude less [68] (1 in 10^6) of the nucleated cell population (anuclear platelets and red blood cells in the hematopoietic fraction are generally not included in cell counts) from human iliac marrow aspirates. In addition to MPCs, MSCs likely contain partially-differentiated osteoblasts and fibroblasts, as well as hematopoietic cells [173]. In fact, Phinney et al. [153] speculated that MPCs, in various inbred mouse strains, may only represent $10\,\%$–$20\,\%$ of the plastic adherent cell population, with a balance of persistent hematopoietic progenitors. It should also be borne in mind that these rates vary from species to species [112, 118], between the young and old [41], as well as between donors, and even between different samples from the same patient [129].

Additional techniques exist to further purify mesenchymal cells from their hematopoietic *in vivo* neighbors prior to culture on TCP. For instance, a density gradient (e.g., Percoll, Ficoll) may be used to fractionate stromal cells from the hematopoietic lineages in fashion similar to that used for whole blood [102]. The density gradient centrifugation method may be also used in combination with a negative-selection antibody cocktail to immuno-deplete hematopoietic cells and enrich for MPCs [1]

(although this dramatically slows the growth rate of cells [8]). In slightly different way, Hung et al. [75] enriched the MPC fraction by size by passing human bone marrow through a porous membrane.

Immunology

The example of the CFU-F assay [24, 54] illustrates a fundamental challenge of stem cell biology: stem cells are defined by their behavior, not by a particular gene or protein expression profile [197]. For whole populations, it becomes difficult, on one hand, to distinguish between directed differentiation and, on the other, the preferential selection and proliferation of differentiated progeny. In this way, the stemness of a particular cell can only be verified by its progeny (i.e., a colony-based retrospective assay), precluding the use of a prospective or presumptive isolation method [197]. There has been a long and intense effort to, by analogy with the marker profile of hematopoietic stem cells [183], identify a unique membrane-surface epitope for MPCs which, when coupled to a fluorescence-activated cell sorting (FACS) or magnetic-activated sorting system, would represent a rapid, high-throughput, sophisticated isolation method with many possible applications. This has not been so straightforward. While endothelial (CD31) and hematopoietic-specific (CD3, CD11a, CD14, CD19, CD34, CD38, CD45, glycophorin A, HLA-DR) markers [77, 166] are absent in MPC cultures, they do heterogeneously express cell-surface antigens (CD73, CD90, CD105) from multiple mesenchymal lineages and germ layers [113, 166, 173]. MPCs do express major histocompatibility complex (MHC) class I proteins but are negative for human leukocyte antigen (HLA) class II molecules [25]. Without costimulatory molecules (CD40, CD80, CD86 [166]), T-cells may be activated by MHC I but are left anergic [81]. This combination strongly suggests MPC are non-immunogenic,

6

making them favorable candidates for allogenic transplantation as suggested above.

The first monoclonal antibody (mAb) candidate for a positive selection protocol, STRO-1$^+$, was reported by Simmons and Torokstorb [177]. Sorting for these cells enriched for multipotent CFU-Fs capable of transferring the hematopoietic microenvironment. Many other candidate mAbs have also been reported [45], but results tend to be species-specific [1]. Additionally, dramatic loss of cell viability following FACS of MSCs has been a significant hurdle for some groups [196].

Returning to the physical rather than immunological properties of cells, osteoprogenitor cells from fetal rat periosteum isolated for small size and low cytoplasmic granularity via optical scattering properties and FACS yielded a slowly-cycling, MPC population [217]. Later, Smith et al. [181] reported the isolation of a highly-clonogenic (90 %) fraction of human MSCs capable of osteogenesis and adipogenesis using similar sorting criteria. In this approach, the confounding and viability effects of antibody conjugation and/or residual tags in subsequent culture are absent, making it especially suitable for routine use.

Proliferative potential

Rarity notwithstanding, these cells exhibit massive proliferative potential: $> 10^6$ (≈ 20 population doublings) clonal progeny can routinely be obtained from a single adult human MSC [154]. Bruder et al. [19] found a mean terminal of nearly 40 doublings prior to senescence (irreversible cessation of mitosis), putting MSCs between fetal (50 doublings) and adult (20 doublings) fibroblasts in terms of proliferative potential [67]. Importantly, this provides practical evidence that MSCs are inherently "younger" than other fibroblast-like cells of the same animal. Furthermore, indications point to a strong coupling between differentiation and proliferation potentials,

as multipotency is diminished with serial passage and culture confluency [40].

Morphology

The morphology of 2-D primary-cultured MSCs, as observed by Friedenstein et al. [53], is heterogeneous and species-dependent but is above all fibroblast-like, especially with increased time in culture. By definition then, no gross morphological change should accompany fibrogenesis. Chondrogenic differentiation of MPCs produces cells (chondrocytes) that have a characteristic rounded, unspread appearance [22], while differentiation to osteoblasts reveals cells that are more flat and polygonal [115]. Adipocytes and myoblasts appear similar to chondrocytes [115] and fibroblasts, respectively.

Immunocytochemistry and gene expression

As with all cell culture, however, morphological characterization, besides being subjective, is satisfactory for only the most routine or preliminary of assays. Mesenchymal (multi)potency and differentiation of MSCs in clonal colonies, entire populations, or 3-D cultures are almost universally verified at least by (immuno)cytochemical staining. Since the phenotypes of interest are mesenchymal, these usually involve identification of a secreted extracellular matrix (ECM) molecule or intracellular precursor. The most common stain for adipogenesis is Oil Red O, a fat-soluble dye that dissolves in lipid droplets and reveals adipogenic cells. Such a cell population can also be immunofluorescently-tagged with a mAb for the enzyme lipoprotein lipase for the same purpose. The cationic dyes Alcian blue [206] and Safranin O [98] provide convenient markers for negatively-charged glycosaminoglycans (GAGs) characteristic of chondrogenic cultures, or, immunofluorescence staining for collagen II (Col2) will also detect presumptive cartilage ma-

trix [186]. Myogenic cultures can be identified by immuno-staining for the transcription factor MyoD or the sarcomeric intermediate filament desmin. Osteogenesis is colorimetrically-assayed by the presence of alkaline phosphatase (ALP) activity, an enzyme tied to pre-osseous and calcifying osteoblastic metabolism [175]; or by stains that directly (alizarin red) or indirectly (von Kossa) interact with deposited calcium in specimens. These same cultures will also immuno-stain positive for collagen I (Col1). More mature osteoblastic cultures can be immunophenotyped with the (glyco)proteins osteocalcin, osteonectin, and osteopontin [144], all of which play various roles in mineralization and/or calcium ion homeostasis.

Unfortunately, no stain or tag or combination thereof is known that *positively* identifies MPCs [9] *or* fibroblasts [190] from the outset; this technical limitation is central to difficulties in studying MPC biology in general and the optimization of MPCs for fibrogenesis in this project in particular. Characterization is thus a practice of negative marking and selection. Put another way, a specimen staining/tagging negatively for a panel of assays from the previous paragraph representing each lineage would at best *not reject* the existence of a putative MPC culture. In addition to the absence of all of the above markers—with the important exception of Col1—*fibroblasts* cultured for the formation and assembly of a tendon or ligament-like tissue should contain α-smooth muscle actin (α-SMA) [89, 127] cytoskeletal isoforms, produce the fibronectin adhesive matrix glycoprotein (AMG) [212], as well as secrete the structural ECM proteins Col1, collagen III (Col3), and elastin (Eln) [131, 210].

Recently, the basic helix-loop-helix (bHLH) transcription factor scleraxis (Scx) has received attention as a marker for the tendon/ligament lineage [18, 35, 169] (Fig. 1.1). Mice lacking the *Scx* gene during embryonic development fail to develop limb tendons [126] properly. Although the role of Scx in the adult is unknown, it my

be an important marker if MSC participation in tendon/ligament neogenesis *in vivo* or *in vitro* is anything like that in the embryo.
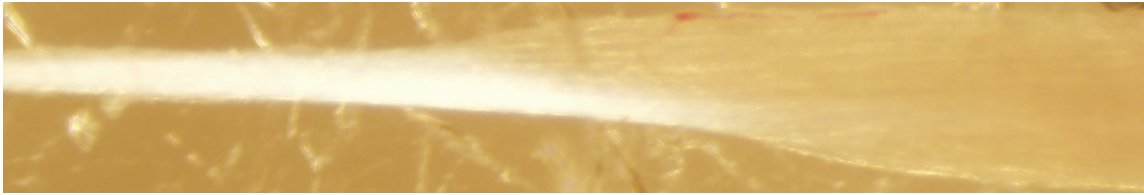
(a) Brightfield.
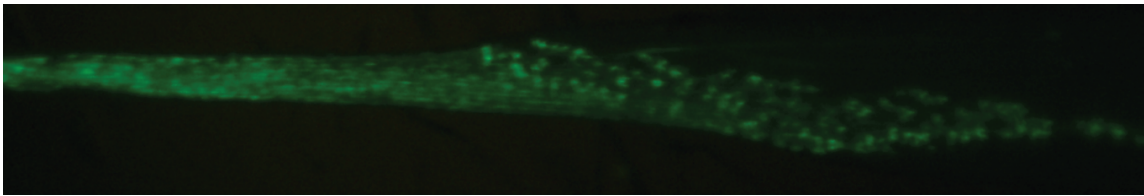
(b) GFP.

Figure 1.1: *Scleraxis* is expressed in the lumbrical tendon (left side) but not muscle (right side) as indicated by GFP reporter in the *ScxGFP* transgenic mouse [159]. Micrographs courtesy of Dr. Christopher L. Mendias.

Many, if not most investigators now use the expression of the same aforementioned marker protein genes via reverse transcription (RT)-polymerase chain reaction (PCR) to phenotype their cultures, with (immuno)cytochemistry as validation. Of course, measures of gene up/down-regulation are inherently less functional in nature, but it does enable a class of experiments of higher sensitivity, shorter term and greater economy.

1.2.2 Regulation

Regulation of stem cell differentiation and fate depends on both *intrinsic* and *extrinsic* factors. Intrinsic control, which subsumes the action of transcription factors and chromatin [64], is beyond the scope of this work. Extrinsic regulation *in vivo* is dominated by the properties of the 3-D niche; *in vitro* this corresponds to controllable factors in the culture environment that may be chemical in nature, either

soluble (freely-diffusing species) or insoluble (immobilzed species), or physical, such as geometry or stiffness.

Chemical factors

Pharmacologic agents   Analogous to the canonical chemical stains for the mesenchymal lineages (§1.2.1), a panel of hormonal and pharmaceutical cocktails containing differentiation factors are well-known to be effective on MPCs. These are introduced separately from other growth factors and cytokines whose precise role in MPC differentiation is less-established. Chief among these differentiation factors are β-glycerophosphate (β-gly) or, more commonly, the glucocorticoid dexamethasone (Dex) [117] and the the coenzyme ascorbic acid that induce osteogenesis in MPCs. Furthermore, viability and functional nodule formation can be enhanced in the presence of Dex [11], but at least one study reports Dex having an anti-osteogenic effect on murine MSCs [48]. The drug indomethacin uniquely induces adipogenesis, especially in the presence of Dex, and sometimes combined with 1,25-dihydroxyvitamin D_3 or 1-methyl-3-isobutylxanthine [182]. A chondrogenic defined medium containing both Dex and transforming growth factor-beta 3 was formulated by Mackay et al. [111]. Finally, the antimycotic amphotericin B [153] and/or 5-azacytidine [199] have shown to be variously myogenic for rat and murine MPCs. It should be noted that these soluble-factor differentiation conditions also tend to be sensitive to the particular species and serum lot [156], which can be partially offset by screening for mitogenic fetal bovine serum lots [104].

Cytokines   Distinct factors for fibroblastic differentiation do not exist, and so care must be taken to avoid the inclusion of the above potent factors if a fibroblastic culture is desired. Instead, investigators have studied the effect of various growth fac-

tors and cytokines. *In vitro*, basic fibroblast growth factor (bFGF) is known to both increase MPC proliferation and decrease ALP activity [107], which can be exploited to exert an anti-osteogenic effect on cultures. Low doses of a related growth factor, FGF-2, induced increased proliferation as well as uniform increases in the expression of ECM proteins and α-SMA in human MSCs in prolonged culture. Perhaps the most comprehensive study of growth-factors effects on MSCs in the context of fibroblastic differentiation was Moreau et al. [123]. In screening a number of soluble factors and combinations thereof, it was found that an initial treatment by a mitogen, bFGF or epidermal growth factor, followed by transforming growth factor β1 (TGF-β_1) treatment enhanced cell morphology, metabolic activity, and Col1 expression and synthesis. These results, combined with negligible expression of cartilage GAGs and Col2, were interpreted as definitive evidence of fibroblastic differentiation. However, no assay or amplification for *osteogenesis* was examined.

Adhesive matrix glycoproteins   In terms of AMGs, laminin is known to induce osteogenic differentiation in human MSCs [90], and a laminin-containing matrix can be observed surrounding MSCs in 2-D culture [154]. Laminin, however, is a matrix protein of basement membranes in epithelial connective tissue. Tendon and ligament are *non-epithelial* tissues, in which fibronectin is the predominant AMG that attaches fibroblasts to collagen [212]. Other than isolated evidence that fibronectin preserved stemness in adipose-derived MPCs [133, 184], little else is known about its role in differentiation of MPCs. Interestingly, scaffolds modified with arginine-glycine-aspartate sequences, which mimic the integrin-binding domains on AMGs, have induced osteogenesis in rat MSCs in the absence of differentiation factors [174] (§1.2.2).

Oxygen tension   A controllable MSC culture parameter that recently has received renewed attention is oxygen fraction (ϕ_{O_2}). Traditional cell and tissue culture ϕ_{O_2} is maintained near atmospheric levels ($\sim 18\,\%$), yet mean tissue level *in vivo* is $3\,\%$ with substantial variation [36]. It has long been known that some animal cells [32], including fibroblasts [50], proliferate more rapidly at $\phi_{O_2} < 20\,\%$. In addition to proliferation, $\phi_{O_2} < 5\,\%$ conferred greatest collagen production in human ACL fibroblasts [49]. What is more, embryonic tissues exist in a substantially lower oxygen environment than adult tissues. Indeed, ϕ_{O_2} level is known to affect all aspects of stem cell biology, from enhanced proliferation in murine satellite cells [37], delayed proliferative senescence in murine fibroblasts [149], blunted apoptosis in fetal central nervous system-derived stem cells [188], reversed myogenic suppression in satellite cells [76], and mobilization of hematopoietic progenitor cells from marrow [88]. Of the more limited work done with MSCs, $\phi_{O_2} = 5\,\%$ conditions brought about enhanced osteogenesis in terms of ALP activity and calcium content [105] in rat MSCs (with Dex and β-gly), while $\phi_{O_2} = 3\,\%$ strongly inhibited osteogenesis in human MSCs, even in the presence of Dex [43]. Moreover, culturing MSCs in hypoxic conditions has been shown to upregulate telomerase expression, resulting in cells replicating in excess of their Hayflick limit [67] while retaining multipotency [42]. A couple of hypotheses have been formed to explain these phenomena. Cells may be susceptible to oxygen-derived free radicals in typical cell culture conditions (thus proliferation is reduced), and bone-marrow ϕ_{O_2} *in vivo* measurements vary widely between 1–$7\,\%$ [63, 91] (hence the differentiated phenotype varies) and with a reported mean of $6.8\,\%$ [80]. Since cellular metabolism *in vitro* occurs predominantly by anaerobic glycolysis [52], more oxygen is not necessarily better, especially for those of the connective tissue lineages. By analogy with the hypoxia-induced hepatocyte growth

factor-mediated activation of satellite muscle cells, an altered oxygen tension may also alter the activity of certain cytokines. For example, TGF-β_1 is a disulfide-linked homodimer that has little biological activity in monomeric form, which suggests that the associated redox reaction in low ϕ_{O_2} should enhance its potency. Other than observed osteogenic inhibition [43], the effect of hypoxia has not been considered on the culture of MSCs for tendon/ligament tissue engineering (TE) targets.

Physical factors

In addition to cell-biological aspects, modern tissue engineering has sought to identify physical factors that can augment or replace biochemical signals. Recent important studies *in vitro* on 2-D matrices lend support to this notion, in which precise control of MSC shape [115] or substrate stiffness [46] were able to overwhelm media supplements providing the opposite signal. MSCs were also shown to prefer uniaxial extension as opposed to equibiaxial stretching for smooth muscle-differentiation [148]. It is worth noting that in none of these studies was fibroblastic potential realized in the range of conditions tested.

1.3 Parallel-fibered soft tissue mechanics

In this section, a brief overview of fibrous tissue biomechanics is given; Woo et al. [210] provides the most current comprehensive review on this topic. A modern review of continuum modeling approaches to biomechanics is also available [74].

1.3.1 Composition and morphology

Macroscopically and microscopically, the parallel-fibered ligament and tendon tissues are in many ways very similar. They are predominantly composed of Col1 (the dominant structural protein in the mammalian body [108]) by dry weight (70–

80 %) [62], embedded in a small but significant proteoglycan-rich ground substance consisting mainly of decorin and biglycan [106]. Subtle differences exist in cellularity and composition, wherein ligament fibroblasts are found to be more metabolically active [4], and ligament presents more elastin and is about 10 % Col3 by dry weight [131], along with an assortment of other collagens. Collagen fibril diameters in ligament distribute bimodally to $\approx 50\,\mathrm{nm}$ and $\approx 125\,\mathrm{nm}$ [62] means. Like tendon, ligament tissue exhibits a highly-organized hierarchy, built up from the Col1 triple-helical monomer (1.5 nm wide, $\approx 300\,\mathrm{nm}$ long), organized into fibrils ($\sim 100\,\mathrm{nm}$ diameter, $\sim 100\,\mathrm{\mu m}$ long), then fibers ($\sim 10\,\mathrm{\mu m}$), and finally fascicles ($\sim 100\,\mathrm{\mu m}$), with cross-linking at every level. A planar crimp (wavelength $\sim 10\,\mathrm{\mu m}$ [158]) is canonically-observed in tendon and ligament and is a unique feature of these native tissues that, notably, has not been re-capitulated in engineered tissue equivalents *in vitro*.

1.3.2 Elasticity

The axial stress-strain behavior of tendon and ligament in tension is easily recognizable. It begins with a low-modulus 'toe' region which gradually becomes exponentially-increasing to the 'heel', after which point the stress increases approximately linearly until yield/failure. The form of this curve is conducive to proper physiological function: Generous stretching is permitted at low loads for proper range of motion, but excessive joint movement and possible dislocation is prevented by the stiff linear region of the curve [210]. The precise microstructural underpinnings for this particular shape of curve are not known, but it is likely a combination of fibril un-crimping, fibril stretching, and, to a lesser extent, inter-fibril shear-lag sliding effects. The linear portion of the stress-strain curve is represented by young ACL tissue as stiff as $\approx 110\,\mathrm{MPa}$ and as strong as $\approx 40\,\mathrm{MPa}$, but as weak as $\approx 10\,\mathrm{MPa}$ in

older adults [132]. For rabbit, the most prevalent animal model for ligament study, ACL and MCL tangent moduli measure $\approx 500\,\mathrm{MPa}$ and $\approx 1\,\mathrm{GPa}$, respectively. Similarly, moduli for the MCL of rat (the animal model to be used in this project) $\approx 400\,\mathrm{MPa}$ [157].

A 1-D, scalar, exponential-form stress-strain function introduced by Kenedi [87] and popularized by Fung [56] historically was the most widely-employed model to capture this nonlinear elastic stress-strain behavior of ligament and tendon. The continuum approach is now the standard for tissue biomechanics due to its mathematical generality and suitability to numerical methods (such as the finite element method) necessary to computationally solve practical problems with a modicum of complexity. Though the continuum strain energy generalization of Fung's original exponential function to 3-D and anisotropy are straightforward, the model parameters are still phenomenological coefficients with no physical interpretation. This precludes their direct measurement and requires curve-fitting for their estimation.

The other historical basis of strain energy functions for soft fibrous tissues can be traced to constitutive models for rubbery or polymeric solids. These models either implicitly [163] or explicitly [6] derive their elasticity from the decrease in configurational entropy of a constituent long-chain molecule under axial load. However, the size, spacing, and cross-linking of Col1 hierarchical components (§1.3.1) may prevent the thermally-driven sampling of configurations required for an entropic basis of elasticity. Furthermore, experiments on canine MCL indicated a decrease in modulus with increased temperature [208], a hallmark of *energetic* elasticity. An (energetic-elastic) elastica-based continuum strain energy description suitable for fibrous biopolymers [60] is among well-founded alternative approaches to model nonlinear ligament elasticity.

1.3.3 Anisotropy

Anisotropy is directional dependence that endows tissue with the ability to maximize stiffness and strength for tissue-specific loading configurations with a minimum of biological resources (Fig. 1.2). For the parallel-fibered soft tissues, this anisotropy is primarily governed by the organization and orientation of its Col1 fibrils in a unidirectional fashion. As a result, similar to traditional fiber-reinforced composites, these tissues exhibit *transverse isotropy* in which there is one material preferred direction along the fibril, with a minimum stiffness arising from an interstitial ground substance along directions perpendicular to the fibril. The lone study [160] to quantify this in the human MCL yielded tangent moduli of $\approx 300\,\mathrm{MPa}$ and $\approx 10\,\mathrm{MPa}$ with tensile strengths of $\approx 40\,\mathrm{MPa}$ and $\approx 1.5\,\mathrm{MPa}$ in the longitudinal and transverse directions, respectively. Like other tissues, one of the hallmarks of ligament scarring is a poorly-organized ECM [51]. In ligament, the resulting deficiency in mechanical stiffness and strength corresponds to a loss of function. Moreover, the proper recovery of anisotropy in engineered tissue constructs aimed at augmenting endogenous healing is a crucial step in achieving mechanical equivalence to tissues *in vivo*. The attendant co-alignment of cells and the fibrils of their ECM also sets up the optimal microenvironment for cells to receive and respond to mechanical signals for longer-term remodeling [178, 200, 201].

The mathematical representation of transverse isotropy in continuum strain energy functions usually takes either an *integral-based* form [99] or is trigonometric *moment-based* [16]. In the former, a fiber-level strain energy function (a function of fiber stretch) is multiplied by a fiber direction density function (DDF) and integrated over all possible directions. In the moment-based approach, the fiber strain energy function is evaluated at the mean direction of the DDF and simply scaled

by the mean resultant length (standard deviation) of the DDF strength. The integral expression is more valid for more general strain states, but the latter is clearly more computationally-efficient. An analysis of the ranges of validity for these methods is reported in Bischoff [15], including conditions under which they can be made equivalent.

(a) Tendon [78].   (b) Arterial wall [71].   (c) Skin [176].   (d) Aortic valve [168].
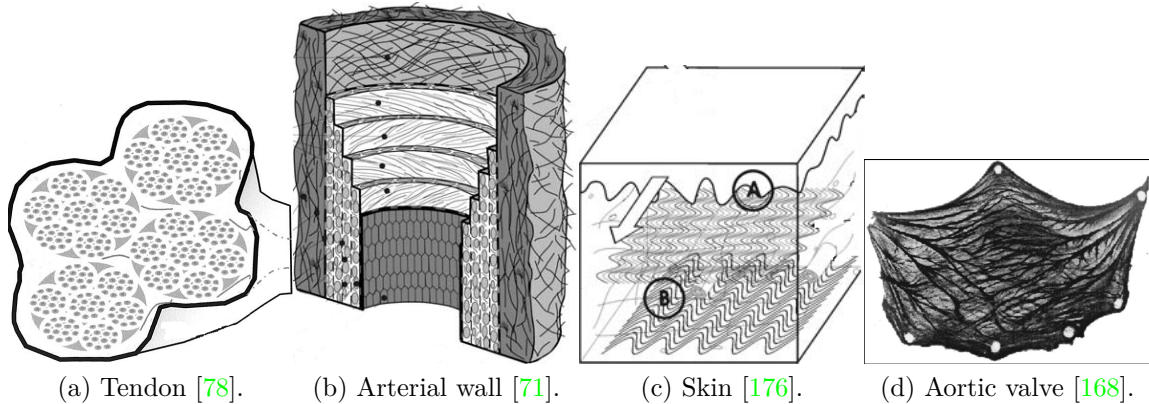
Figure 1.2: Anisotropy is directional dependence that endows tissue with the ability to maximize stiffness and strength for tissue-specific loading configurations with a minimum of biological resources.

1.3.4 Viscoelasticity

Like all biological soft tissues, tendon and ligament exhibit typical time and history-dependent viscoelastic (VE) behaviors. In particular, the quasi-linear viscoelastic (QLV) theory of Fung [56] has seen enormous success in simulating the stress relaxation behavior of parallel-fibered soft tissues. QLV assumes linear (strain-independent) VE while allowing for a nonlinear elastic response (time-strain separability), combined with a relaxation function possessing a constant-valued relaxation spectrum (based on the observed frequency-insensitivity of soft-tissue hysteresis). Importantly, Provenzano et al. [157] have shown rat MCL VE to *not* be load/displacement-independent, apparently rejecting the QLV hypothesis for ligament. Fiber recruit-

ment [192] or general nonlinear VE models [82] have since gained favor to cross-predict creep and relaxation or model relaxation at multiple strain levels.

Furthermore, the physical basis of parallel-fibered tissue VE is currently a point of contention. Unlike the case of cartilage, for which a biphasic mixture model became the standard for cartilage VE shortly after Mow et al. [125] with further enhancements to allow for flow-independent VE with the introduction of solid-phase VE [44, 114], VE models of ligament have remained largely in the domain of QLV. This is despite the physical motivation (fluid flow) and fundamental derivation (balance laws) afforded by the mixture-theory approach from which QLV generally abstains. Recently, investigators have adopted mixture theory for modeling VE experiments on tendon and ligament [214], including our group [58], yet a mixture model of parallel-fibered tissue incorporating a VE solid directly compared with tensile experiments has not yet appeared in the literature. While intrinsic solid VE is likely to play a lesser role in ligament than in cartilage due to differences in proteoglycan content (and possibly lesser still in engineered tissue), the unknown fraction of bound (immobile) interstitial water and possible VE of collagen motivates a detailed investigation of ligament VE using the elastic-solid and viscoelastic-solid versions of the mixture model combined with multiple VE testing protocols. Reports of experimental determination of human MCL hydraulic permeability [204], a critical transport parameter for inclusion in a mixture model, indicates this approach is gaining favor in the field.

1.3.5 Growth and remodeling

Even when just accounting for passive mechanical behavior, soft biological tissue represents a borderline worst-case scenario from a mechanician's standpoint: it

is hydrated, compliant, heterogeneous, anisotropic, nearly-incompressible, VE, and capable of large deformations. To subsume the physics of engineered-tissue requires consideration of living tissue's ability to grow and remodel—to *functionally adapt*—to its chemo-mechanical environment. As a material, this unique feature of biological tissue necessitates a proper experimental and theoretical treatment of multiple interacting and interconverting soluble and insoluble species/phases, the fine-scale behavior of which exerts, and is subject to, the *phenotype* of resident cells which grow and remodel the macroscopic tissue. In a modeling context, our group has carefully delineated between the developmental processes of growth and remodeling in biological and engineered tissue. The common thread tying growth and remodeling together is the feature of thermodynamic irreversibility, a notion which is consistent with the dynamic, dissipative, non-equilibrium nature of biological systems.

Growth is defined as *a change in mass* [58], and is typified by the synthesis or enzymatic degradation of matrix proteins. An early mathematical theory for adaptive growth in bone [34] introduced a solid scalar mass source/sink fed by a strain-controlled chemical reaction. Epstein and Maugin [47] introduced a vectorial mass flux. Our group incorporated the classical notions of scalar mass sources/sinks and vectorial mass fluxes (among others) in an open-mass continuum mixture model consisting of solid and fluid phases and an arbitrary number of soluble chemical species [58]. As with the previous models, the system is open with respect to mass, but in particular, growth occurs not by the transport of end-products but by the interconversion (reaction) of soluble chemical species. These precursor and byproduct species are capable of Fickean flux with respect to the fluid phase as well as convective flux along with the fluid, all of which may be occurring with respect to the solid.

On the other hand, *remodeling* is generally defined as any evolution of material

properties that does not rely on changes in or fluxes of mass, but is most commonly thought of as a change of microstructure [59], such as the reorientation or fusion of fibrous matrix proteins. The ability of contractile cells to induce *in vivo*-like patterns of alignment in collagen gels by tractional reorientation [10, 187] is now well known. This role of cell traction in aligning collagen fibrils can be demonstrated with a straightforward cell culture experiment (Fig. 1.3). When a fibroblast-seeded collagen gel is placed between crossed, polarized filters immediately following gelation, the collagen gel, a birefringent species, is observed to be isotropic since it does not rotate the polarity of light and the field is dark. Over the course of 12 h as the fibroblasts attach to the collagen matrix and exert their intrinsic contractile activity, the gel is compacted around fixed constraints. As collagen becomes more organized from the resultant tension, it allows the transmission of more light through the polarized lens, which is readily observed with the sequential increase in intensity (Fig. 1.3b). In contrast, similar experimental configurations without constraints or without cells do not yield contraction and/or alignment, pointing to both mechanical forces and cells as necessary ingredients for ECM remodeling.
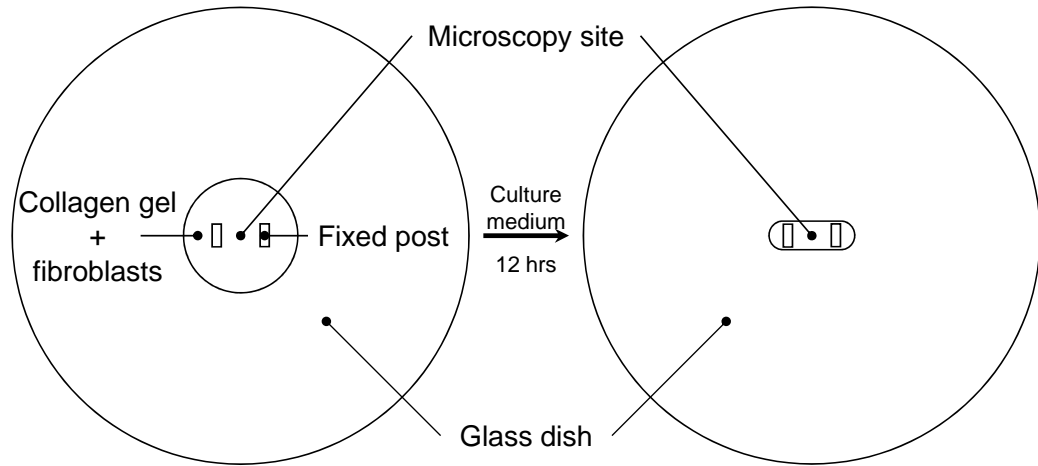
(a) Experimental setup. 1 mg/mL collagen gels (Collagen I, Rat Tail, #A1048301, Invitrogen, Grand Island, NY) were seeded with TFbs (§4.2.2) in GM (§4.2.1) at 1×10^6 cell/mL and delivered to a glass petri dish around two fixed polyethylene posts. Over the course of 12 h, the intrinsic traction exerted by the cells on the collagen induced compaction of the gel as limited by the posts into a ligament-like structure.

t	Gel+Cells+Post	Gel+Cells	Gel+Post
0 h			
4 h			
12 h			

(b) Polarized light micrographs. Dish setup was placed between crossed polarized filters and micrographs taken in time. Both cells and the geometric constraint provided by the post are required to develop anisotropy, indicated by an increase in captured intensity. Lack of posts or cells yields no alignment and no change in intensity.

Figure 1.3: Tractional collagen fibril reorientation.

Fusion is ubiquitous *in vivo* as collagen fibril segments undergo post-depositional modifications in embryonic tendon. The end-to-end association and fusion of fibrils yield increases in length with insignificant changes in diameter (Fig. 1.4a). Interestingly, a rapid increase in late-embryonic tendon mechanical properties correlates with measured lengthening of fibrils [116], again implicating an interplay between mechanics and biologically-driven remodeling.

(a) Schematic.   (b) Electron micrograph.
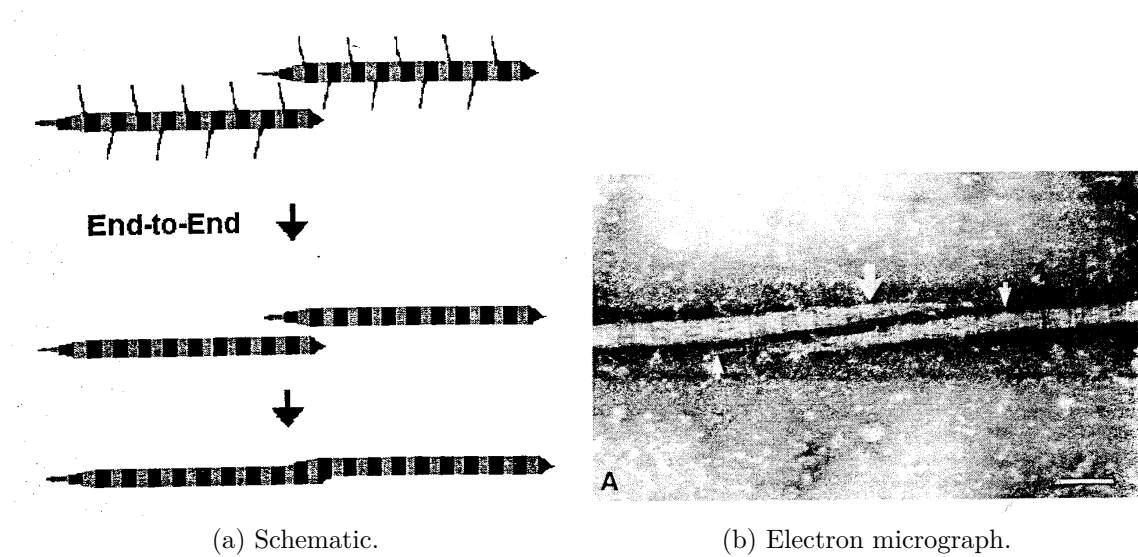
Figure 1.4: Longitudinal collagen fibril fusion [14].

Moreover, the differentiation of stem cells is also consistent with this mathematical notion of biological remodeling, that is, an irreversible evolution of an internal variable (indicating some degree or extent of differentiation) with negligible change in overall mass. All these events are usually separated from processes of growth by time scales of at least an order of magnitude; i.e., macroscopic, mechanically-relevant growth occurs over days while remodeling occurs over hours (Fig. 3.4a and Fig. 3.4b, insets).

1.4 Microscopy and image analysis for anisotropy quantification

Among the many properties that enable soft biological connective tissue to perform their mechanical function, yet complicate their experimental and theoretical study, *anisotropy* endows tissue with the ability to maximize stiffness and strength for tissue-specific loading configurations with a minimum of biological resources. For soft tissues, this anisotropy is primarily governed by the organization of collagen, the dominant structural protein in the mammalian body [108]. In particular, parallel-fibered soft tissues such as ligament and tendon possess an ECM composed of type I collagen fibrils as well as a proteoglycan-rich intervening ground substance. As a result, similar to traditional fiber-reinforced composites, these tissues exhibit *transverse isotropy* in which there is one material preferred direction along the fiber, while any direction perpendicular to the fiber relies on the response of the matrix ground substance. Like other tissues, one of the hallmarks of ligament scarring is a poorly-organized ECM [51] with a corresponding loss of mechanical properties. Moreover, the proper recovery of anisotropy in engineered tissue contructs (ETCs) aimed at augmenting endogenous healing is a crucial step in achieving mechanical equivalence to tissues *in vivo*. For example, contractile cells like fibroblasts rapidly (within hours) induce *in vivo*-like patterns of alignment in mechanically-constrained collagen gels (demonstrated notably by Stopak and Harris [187]). While this mechanism provides a basal level of anisotropy for the short-term, the attendant co-alignment of cells and the fibrils of their ECM also sets up the optimal microenvironment for cells to receive and respond to mechanical signals for longer-term remodeling [178, 200, 201].

Given the mechanical importance of ECM anisotropy development, whether in wound repair or in tissue engineering, appropriate methods are necessary for its sys-

tematic study and constitutive modeling. In the years since seminal work by Bell et al. [10], Stopak and Harris [187] and others, the fibroblast-populated collagen lattice has seen continued use as such a model system for studying cell-matrix interactions [155]. Since isotropy remodeling occurs in these gels, at least in part, via cell-mediated fibril reorientation, detailed information is required about the time course of fibril orientation in 3D *in situ* (i.e., under mechanical load). Small angle light scattering has been used extensively to characterize in detail the collagen organization in planar tissues ($<500\,\mu m$) [13, 165], but with a spatial resolution of $\geq 100\,\mu m$. By exploiting the birefringent property of the collagen molecule, quantitative polarized light microscopy can provide indirect information on collagen alignment in real time ($\Delta t \approx 5\,s$) [193], although it can only resolve orientations orthogonal to the optical axis and the data is thickness-averaged. It is therefore still suitable mainly for relatively thin, planar specimens, although incorporation of a universal stage attachment has allowed additionally the measurement of elevation angles up to 15° in the arterial wall [180]. Additional methods for analyzing orientation in thin samples or on surfaces of samples with varying temporal resolution include synchrotron x-ray scattering [120], laser Raman microscopy [202], optical coherence tomography [66], and elastic scattering spectroscopy [94]. confocal laser scanning microscopy (CLSM), on the other hand, can be used to produce 3-D volumetric (tomographic) image data as a result of its *optical sectioning* property and shallow depth of field. Its lateral resolution and, moreover, contrast are also enhanced as compared to widefield optics [145]. This is important since the fibril diameters in reconstituted collagen gels are typically $\sim 100\,nm$ (as measured by electron microscopy [70]), while the (uncorrected) Rayleigh criteria of resolution for high numerical aperture (NA) objectives in common use are 200–300 nm [86]. Making use of the reflectance properties of

25

collagen, *reflection* or *backscattered-light–mode* CLSM has been successfully applied during the mechanical testing of collagen gels ($\Delta t \approx 15 \, \text{min}$) [164]. This capability is particularly attractive for biological applications since it requires no fixation or staining of the specimen.

Since the (micro)structural anisotropy of the specimen is obtained with CLSM by direct visualization and not otherwise inferred from the specimen's optical properties, the quantitative analysis of microscopy data is essentially reduced to one of image processing. A classical stereological approach for 3-D data is to examine the variation between image slices in terms of intersection counts of a linear probe with features in the planar image [167, 194], but is not sensitive enough for slight anisotropies [205]. One can also identify and analyze the orientation of individual particles in the specimen, as is common in the study of suspensions of anisometric colloids [122]. Another such discrete approach was introduced by Wu et al. [211, 211] for quantifying diameter, length, and 3-D orientation of fibrils in a suitably-imaged (i.e., CLSM) collagen gel. For data in which the identification of individual constituents is difficult, computationally-intensive, and/or unnecessary for a particular application, a reasonable alternative is to instead analyze the orientations of image texture patterns (i.e., fiber-like lines/edges). This approach lends itself to a continuous treatment of the image intensity field, and is well-studied in paper[213], textile [26], and other polymer [39] and materials [83, 161] processing. One of the first applications of such image processing to collagen microstructure was to extract the components of a Fourier-transformed electron micrographs falling within a band of angles [27]. A critical issue that emerged was the loss of angular sensitivity in digital images with lower frequency components. In this case, the transformed intensities cluster to the center of the image where the rectangular pixel grid is inherently coarser in the

angular coordinate. Other frequency-domain analyses involving radial-coordinate integration of power spectrum intensity as a function of angle were applied to obtaining mean directions in paper sheet laser optical diffraction [213], collagen fiber disarray via small angle light scattering [95], and phalloidin-FITC–conjugated stress fiber orientation in corneal wound contraction under CLSM [152]. Yuhara et al. [215] instead suggested that only the frequency band corresponding to fiber width is of interest. However, none of these studies included any significant calibration to test images in terms of *deviation* or *dispersion* of texture orientations quantifying the extent of alignment. This aspect was visited later by Palmer and Bizios [147], when it was found that a similar frequency-domain analysis technique did not match manual measurements of orientation deviations for fluid-sheared endothelial cell populations. In contrast, Chaudhuri et al. [26] outlined the basic procedure for most *spatial-domain* methods to follow, namely, *edge detection*, *directional histogram construction*, and some kind of *parameter identification* or *peak detection*. Along with [84], these methods were reasonably validated with test images, but are fraught with a multiplicity of parameters and seemingly ad-hoc statistical treatments at each step of the procedure. Combined with a lack of justification of parameter values, adaptation of their methods to even a slightly different problem would yield uncertain results. Nevertheless, the gradient-based method of [84] was recently applied to individual confocal reflectance microscopy images of fixed sections of remodeled collagen gels [33, 191], as well as sheared endothelial cells *in vitro* [85].

1.5 Parallel-fibered tissue engineering

The literature on the engineering of fibrous connective tissue is already vast. The reviews Petrigliano et al. [151], Vunjak-Novakovic et al. [198] are noted for a more

thorough treatment, especially with respect to the scaffolding aspect of ligament engineering, a discussion of which is neglected here due to the scaffold-less approach utilized by the STEL.

1.5.1 Culture system parameters
Cell source

Only one salient study appears to have been conducted evaluating the differential performance of these cell types in an engineered construct framework [195]. It was found that, versus skin and ACL fibroblasts, MSCs engrafted resorbable suture material with greater proliferation and collagen synthesis. These results bode well for MSC-based engineering, but mechanical characterization is additionally necessary to verify the enhanced stiffness and strength that the collagen content readouts imply.

Chemical factors

As on 2-D CP [123], the sequential application of a mitogen (bFGF) to a 3-D MSC-seeded silk-fiber matrices followed with a differentiation factor (TGF-β_1) was found to be the most conducive to collagen synthesis versus use of epidermal growth factor or mitogen-free controls [124]. This is consistent with *in vivo* data: Acute-phase ligament injury TGF-β_1 levels are known to be high in the acute phase of ligament injury (subsiding in 2–4 wk) [210]. Not surprisingly, beginning TGF-β_1 treatment at the peak of cell activity yielded greater activity at day 14 compared to removing all growth factors at peak activity. Given the diversity and complexity of functions by the TGF-β_1 superfamily [7], and the time-dependent expression of TGF-β_1 receptors, an additional investigation of TGF-β_1's role in fibroblastic differentiation is outside the scope of this work. These studies [123, 124] provide the best precedent for MSC fibrogenesis and ligament engineering with respect to cytokine

administration. The usage of TGF-β_1 has also been shown to be critical to construct self-assembly using tendon fibroblasts our laboratory [20].

In contrast to 2-D cell culture, the existence of a 3-D solid matrix surrounding cells in engineered tissue culture brings with it a more restrictive diffusion environment for soluble factors; this limitation is exacerbated by the fact that almost all tissue engineering applications do not include vascular support [203]. So, while subatmospheric oxygen tension may be more normoxic for mesenchymal cells on tissue culture plastic, this hypothesis must be re-evaluated for a 3-D engineered tissue construct. Oxygen concentration is $\sim 0.07\,\mathrm{mM}$ and diffusion is quite slow ($\sim 2.0\times 10^{-5\,\mathrm{cm^2}}/\mathrm{s}$[128]) in normal tissues, but the diffusion distance *in vivo* is at most only $200\,\mu\mathrm{m}$ from capillary to cell membrane [30, 31] (chondrocytes may survive at $> 1\,\mathrm{mm}$ cartilage thickness). Using a conservative oxygen consumption rate of $4 \times 10^{-17\,\mathrm{mol}}/\mathrm{cel\cdot s}$ for MSCs [96] and zeroth-order kinetics, a simple calculation shows that the radius for a scaffold-less, cylindrical engineered ligament could be at most $\sim 0.25\,\mathrm{mm}$ in $5\,\%\ \phi_{\mathrm{O_2}}$ versus $0.5\,\mathrm{mm}$ for $20\,\%\ \phi_{\mathrm{O_2}}$ to avoid oxygen depletion at the very center [128]. Fortunately, the glycolytic capacity of mesenchymal cells *in vitro* [52] may obviate some of these restrictions, but to what extent is unknown without quantitative data on their basal aerobic respiration rate in culture.

Physical factors

The studies cited in §1.2.2 [46, 115] did not utilize 3-D matrices, a cell's (insoluble) adhesion with which is known to differ fundamentally than that on 2-D surfaces [38]. This is critical since this so-called "3-D–matrix adhesion" is the substrate for the initial mechanotransduction event upstream of the signaling cascade that ultimately influences lineage. Therefore, the influence of ECM stiffness or cell shape in 3-D

context is as yet undetermined.

Widespread evidence points to the general optimization of native [209] and engineered tissue phenotype in response to cyclic mechanical stimulation in terms of cell proliferation [12], ECM protein alignment [170] and breakdown [171], and synthesis [79] for a variety of tissue targets, all of which can potentially enhance mechanical properties. The effect of mechanical stimulation is less understood with respect to directed differentiation of MPCs. Chondrogenesis is enhanced under cyclic compression with respect to both static culture [5] and chondrogenic medium [72]. Altman et al. [3] reported a sophisticated bioreactor for paralled-fibered tissue equivalents capable of simultaneous stretching and twisting deformations mimicking *in vivo* ligament loading patterns. Most compelling in the context of fibrogenesis and ligamentization is their report that cyclic stretch-twist of MSC-seeded collagen gels using this same device upregulated Col1, Col3, and fibronectin transcription and increased their deposition [3]. These appear to be isolated observations with respect to phenotype and need to be further substantiated. A later study also indicated that the collagen production of MSC-seeded silk matrices was sensitive to the timepoint in culture at which mechanical stimulation was first applied [28].

The mechanisms behind cyclic stress/strain-stimulated tissue growth, remodeling, and differentiation are likely some combination of direct cell mechanotransduction and convective mass transport. But the relative roles of these biological and physical phenomena are compelling unknowns in the mechanobiology of 3-D engineered tissue since the two occur concomitantly and are not easily independently-controlled in practice. While the experimental investigation of this question in the context of a scaffold-less, self-assembling ligament construct is outside the scope of this project, it may, however, be approached theoretically using tools such as the continuum,

multiphysics, computational model to be enhanced and utilized herein.

1.5.2 Characterization and evaluation

Composition and morphology

Due to the diversity of precursor scaffolds and architectures, it is difficult to compare engineered-ligament and tendon outcomes based on composition or morphology. In general, the scaffold-less approaches tend to be more cellular and collagen fibrils thinner ($\approx 60\,\text{nm}$) [21] than native tissue. With silk-based scaffolding, synthesized collagen is often deposited directly onto the existing fibers, which may degrade quickly, instead of forming its own matrix *de novo* [29].

Mechanical properties

As indicated from the outset, a continuing challenge for all connective tissue engineering is obtaining constructs that are nominally-equivalent in mechanical response. Scaffold-less engineered tendon in this group has registered as stiff as $17\,\text{MPa}$ with an ultimate strength of at least $2\,\text{MPa}$ [21]. Later MSC-based ligament constructs based on similar technology achieved tangent moduli of $\approx 15\,\text{MPa}$ with similar ultimate strengths as before [21]. Tangent moduli $\approx 100\,\text{MPa}$ were obtained using a fibroblast-populated collagen-scaffold–collagen-gel approach, with ultimate strengths as high as $\sim 10\,\text{MPa}$ [61]. A highly–cross-linked collagen-based engineered ligament neared native tissue at $> 40\,\text{MPa}$ [23], while synthetic scaffold strengths have reached super-physiological levels in the 100s of MPa. Mechanical properties of the silk-based scaffold approach are difficult to compare since the authors did not properly normalize the structural properties of their constructs to obtain stress and strain [2, 28].

Few data exist in the literature on the VE properties of engineered ligament and tendon. In stress relaxation ($\approx 0.01\,\text{s}^{-1}$ strain rate), Gentleman et al. [61] reported

equilibrium-to-peak stress ratios of $\approx 25\,\%$ and half-relaxation time constants of just a few seconds, indicating a rapidly-equilibrating response.

1.6 Overview and summary of contributions

This dissertation is organized as follows:

Following the introductory Chap. 1, Chap. 2 covers a detailed analysis of the thermodynamics of a class of mathematical models of fiber remodeling, i.e., both re-orientation and fusion. The thermodynamic admissibility of such laws in the context of the dissipation equality are examined as well as issues of maximum dissipation, strain energy convexity, and numerical solutions of the fully 3-D nonlinear elasticity problem.

Chap. 3 describes the formulation, validation, and application of an edge-based image processing method to extract and quantify fiber direction and alignment information from planar and volumetric image data.

Chap. 4 reports on a cell and molecular biology study of the fibrogenic potential of MSCs and TFbs under differential ϕ_{O_2} culture during the monolayer phase of the engineered-tendon/ligament system prior to self-assembly. Chap. 5 contains concluding remarks.

Table 1.1 list conference platform and poster presentations and refereed publications resulting from doctoral research. Note that work related to the development and analysis of a model of focal adhesion dynamics is not described in the dissertation.

Table 1.1: Abstracts and publications resulting from doctoral research.

Type	Reference	Chapter	Notes
Platform	Thermodynamic considerations for remodeling in biological tissue; Olberding, Garikipati, Kuhl, Grosh, and Arruda [135]	2	
Publication	Biological remodelling: Stationary energy, configuration change, internal variables and dissipation; Garikipati, Olberding, Narayanan, Arruda, Grosh, and Calve [59]	2	
Platform	Fibroblast-Mediated Collagen Fibril Reorientation in Three Dimensions Using Confocal Reflection Microscopy; Olberding, Garikipati, Arruda, and Garikipati [136]	2,3	
Platform	Quantification of Collagen Fibril Reorientation in Volumetric Image Data by Confocal Microscopy; Olberding, Grosh, Arruda, and Garikipati [137]	3	
Platform	Focal adhesion dynamics: Reaction domination; Olberding, Thouless, Arruda, and Garikipati [138]	—	
Poster	Role of oxygen content on the fibrogenesis of bone marrow stromal cells; Olberding, Garikipati, Grosh, Larkin, and Arruda [139]	4	
Proc. paper	A Theoretical Study of the Thermodynamics and Kinetics of Focal Adhesion Dynamics; Olberding, Thouless, Arruda, and Garikipati [143]	—	Published
Publication	The non-equilibrium thermodynamics and kinetics of focal adhesion dynamics; Olberding, Thouless, Arruda, and Garikipati [142]	—	Submitted
Publication	Effect of oxygen on the fibrogenesis and parallel-fibered engineered tissue potential of bone marrow stem cells and fibroblasts; Olberding, Garikipati, Grosh, Larkin, and Arruda [140]	4	In preparation
Publication	Fiber reorientation and fusion and maximum thermodynamic dissipation; Olberding, Grosh, Arruda, and Garikipati [141]	2	In preparation
Publication	An intensity gradient-based method for quantifying fiber orientation distribution in planar and volumetric data; Olberding, Garikipati, Grosh, Larkin, and Arruda [140]	3	In preparation

BIBLIOGRAPHY

[1] A. Alhadlaq and J. J. Mao. Mesenchymal stem cells: Isolation and therapeutics. *Stem Cells and Development*, 13(4):436–448, 2004. 5, 7

[2] G. H. Altman, R. L. Horan, H. H. Lu, J. Moreau, I. Martin, J. C. Richmond, and D. L. Kaplan. Silk matrix for tissue engineered anterior cruciate ligaments. *Biomaterials*, 23(20):4131–4141, Oct 2002. 31

[3] G. H. Altman, H. H. Lu, R. L. Horan, T. Calabro, D. Ryder, D. L. Kaplan, P. Stark, I. Martin, J. C. Richmond, and G. Vunjak-Novakovic. Advanced bioreactor with controlled application of multi-dimensional strain for tissue engineering. *Journal of Biomechanical Engineering-Transactions of the ASME*, 124(6):742–749, 2002. 30

[4] D. Amiel, C. Frank, F. Harwood, J. Fronek, and W. Akeson. Tendons and ligaments: A morphological and biochemical comparison. *Journal of Orthopaedic Research*, 1(257), 1984. 15

[5] P. Angele, D. Schumann, M. Angele, B. Kinner, C. Englert, R. Hente, B. Fuchtmeier, M. Nerlich, C. Neumann, and R. Kujat. Cyclic, mechanical compression enhances chondrogenesis of mesenchymal progenitor cells in tissue engineering scaffolds. *Biorheology*, 41(3-4):335–346, 2004. 30

[6] E. M. Arruda and M. C. Boyce. A 3-dimensional constitutive model for the large stretch behavior of rubber elastic-materials. *Journal of the Mechanics and Physics of Solids*, 41(2):389–412, Feb 1993. 16

[7] L. Attisano and J. L. Wrana. Signal transduction by the TGF-beta superfamily. *Science*, 296(5573):1646–1647, 2002. 28

[8] M. Baddoo, K. Hill, R. Wilkinson, D. Gaupp, C. Hughes, G. C. Kopen, and D. G. Phinney. Characterization of mesenchymal stem cells isolated from murine bone marrow by negative selection. *Journal of Cellular Biochemistry*, 89(6):1235–1249, Aug 2003. 6

[9] B. Barrilleaux, D. G. Phinney, D. J. Prockop, and K. C. O'Connor. Review: Ex vivo engineering of living tissues with adult stem cells. *Tissue Engineering*, 12(11):3007–3019, 2006. 3, 9

[10] E. Bell, B. Ivarsson, and C. Merrill. Production of a tissue-like structure by contraction of collagen lattices by human-fibroblasts of different proliferative potential invitro. *Proceedings of the National Academy of Sciences of the United States of America*, 76(3):1274–1278, 1979. 21, 25

[11] C. G. Bellows, J. N. M. Heersche, and J. E. Aubin. Determination of the capacity for proliferation and differentiation of osteoprogenitor cells in the presence and absence of dexamethasone. *Developmental Biology*, 140(1):132–138, Jul 1990. 11

[12] C. C. Berry, J. C. Shelton, D. L. Bader, and D. A. Lee. Influence of external uniaxial cyclic strain on oriented fibroblast-seeded collagen gels. *Tissue Engineering*, 9(4):613–624, Aug 2003. 30

[13] K. L. Billiar and M. S. Sacks. A method to quantify the fiber kinematics of planar tissues under biaxial stretch. *Journal of Biomechanics*, 30(7):753–756, 1997. 25

[14] D. E. Birk, M. V. Nurminskaya, and E. I. Zycband. Collagen fibrillogenesis insitu - fibril segments undergo postdepositional modifications resulting in linear and lateral growth during matrix development. *Developmental Dynamics*, 202 (3):229–243, 1995. 23

[15] J. E. Bischoff. Continuous versus discrete (invariant) representations of fibrous structure for modeling non-linear anisotropic soft tissue behavior. *International Journal of Non-Linear Mechanics*, 41(2):167–179, 2006. 18

[16] J. E. Bischoff, E. A. Arruda, and K. Grosh. A microstructurally based orthotropic hyperelastic constitutive law. *Journal of Applied Mechanics-Transactions of the ASME*, 69(5):570–579, 2002. 17

[17] T. R. Brazelton, F. M. V. Rossi, G. I. Keshet, and H. M. Blau. From marrow to brain: Expression of neuronal phenotypes in adult mice. *Science*, 290(5497): 1775–1779, Dec 2000. 3

[18] D. Brown, D. Wagner, X. Q. Li, J. A. Richardson, and E. N. Olson. Dual role of the basic helix-loop-helix transcription factor scleraxis in mesoderm formation and chondrogenesis during mouse embryogenesis. *Development*, 126 (19):4317–4329, Oct 1999. 9

[19] S. P. Bruder, N. Jaiswal, and S. E. Haynesworth. Growth kinetics, self-renewal, and the osteogenic potential of purified human mesenchymal stem cells during extensive subcultivation and following cryopreservation. *Journal of Cellular Biochemistry*, 64(2):278–294, Feb 1997. 5, 7

[20] S. Calve. *Morphological and Mechanical Characterization of Self-Assembling Tendon Constructs and Myotendinous Junctions.* Ph.D. dissertation, University of Michigan, Ann Arbor, 2006. 29

[21] S. Calve, R. G. Dennis, P. E. Kosnik, K. Baar, K. Grosh, and E. M. Arruda. Engineering of functional tendon. *Tissue Engineering*, 10(5-6):755–761, 2004. 2, 31

[22] A. I. Caplan. Mesenchymal stem-cells. *Journal of Orthopaedic Research*, 9(5): 641–650, Sep 1991. 2, 8

[23] A. B. Caruso and M. G. Dunn. Functional evaluation of collagen fiber scaffolds for ACL reconstruction: Cyclic loading in proteolytic enzyme solutions. *Journal of Biomedical Materials Research Part a*, 69A(1):164–171, Apr 2004. 31

[24] H. Castro-Malaspina, R. E. Gay, G. Resnick, N. Kapoor, P. Meyers, D. Chiarieri, S. Mckenzie, H. E. Broxmeyer, and M. A. S. Moore. Characterization of human-bone marrow fibroblast colony-forming cells (CFU-F) and their progeny. *Blood*, 56(2):289–301, 1980. 6

[25] G. Chamberlain, J. Fox, B. Ashton, and J. Middleton. Concise review: Mesenchymal stem cells: Their phenotype, differentiation capacity, immunological features, and potential for homing. *Stem Cells*, 25(11):2739–2749, Nov 2007. doi: {10.1634/stemcells.2007-0197}. 6

[26] B. B. Chaudhuri, P. Kundu, and N. Sarkar. Detection and gradation of oriented texture. *Pattern Recognition Letters*, 14(2):147–153, 1993. 26, 27

[27] S. Chaudhuri, H. Nguyen, R. M. Rangayyan, S. Walsh, and C. B. Frank. A fourier domain directional filtering method for analysis of collagen alignment in ligaments. *Ieee Transactions on Biomedical Engineering*, 34(7):509–518, 1987. 26

[28] J. S. Chen, R. L. Horan, D. Bramono, J. E. Moreau, Y. Z. Wang, L. R. Geuss, A. L. Collette, V. Volloch, and G. H. Altman. Monitoring mesenchymal stromal cell developmental stage to apply on-time mechanical stimulation for ligament tissue engineering. *Tissue Engineering*, 12(11):3085–3095, 2006. 30, 31

[29] S. H. Chen and H. J. Gao. Non-slipping adhesive contact of an elastic cylinder on stretched substrates. *Proceedings of the Royal Society A-Mathematical Physical and Engineering Sciences*, 462(2065):211–228, 2006. 31

[30] D. C. Chow, L. A. Wenning, W. M. Miller, and E. T. Papoutsakis. Modeling pO(2) distributions in the bone marrow hematopoietic compartment. I. Krogh's model. *Biophysical Journal*, 81(2):675–684, Aug 2001. 29

[31] D. C. Chow, L. A. Wenning, W. M. Miller, and E. T. Papoutsakis. Modeling pO(2) distributions in the bone marrow hematopoietic compartment. II. modified Kroghian models. *Biophysical Journal*, 81(2):685–696, Aug 2001. 29

[32] P. D. Cooper, A. M. Burt, and J. N. Wilson. Critical effect of oxygen tension on rate of growth of animal cells in continuous suspended culture. *Nature*, 182 (4648):1508–1509, 1958. 13

[33] K. D. Costa, E. J. Lee, and J. W. Holmes. Creating alignment and anisotropy in engineered heart tissue: Role of boundary conditions in a model three-dimensional culture system. *Tissue Engineering*, 9(4):567–577, 2003. 27

[34] S. C. Cowin and D. H. Hegedus. Bone remodeling I: Theory of adaptive elasticity. *Journal of Elasticity*, 6(3):313–326, 1976. 20

[35] P. Cserjesi, D. Brown, K. L. Ligon, G. E. Lyons, N. G. Copeland, D. J. Gilbert, N. A. Jenkins, and E. N. Olson. Scleraxis: a basic helix-loop-helix protein that prefigures skeletal formation during mouse embryogenesis. *Development*, 121 (4):1099–1110, Apr 1995. 9

[36] M. Csete. Oxygen in the cultivation of stem cells. In J. Ourednik, V. Ourednik, Sakaguchi D. S., and NilsenHamilton M., editors, *Stem Cell Biology: Development and Plasticity*, volume 1049 of *Annals of the New York Academy of Sciences*, pages 1–8. New York Acad Sciences, New York, 2005. doi: {10.1196/annals.1334.001}. 13

[37] M. Csete, J. Walikonis, N. Slawny, Y. W. Wei, S. Korsnes, J. C. Doyle, and B. Wold. Oxygen-mediated regulation of skeletal muscle satellite cell proliferation and adipogenesis in culture. *Journal of Cellular Physiology*, 189(2): 189–196, Nov 2001. 13

[38] E. Cukierman, R. Pankov, D. R. Stevens, and K. M. Yamada. Taking cell-matrix adhesions to the third dimension. *Science*, 294(5547):1708–1712, 2001. 29

[39] N. C. Davidson, A. R. Clarke, and G. Archenhold. Large-area, high-resolution image analysis of composite materials. *Journal of Microscopy-Oxford*, 185: 233–242, 1997. 26

[40] C. M. DiGirolamo, D. Stokes, D. Colter, D. G. Phinney, R. Class, and D. J. Prockop. Propagation and senescence of human marrow stromal cells in culture: A simple colony-forming assay identifies samples with the greatest potential to propagate and differentiate. *British Journal of Haematology*, 107(2): 275–281, 1999. 8

[41] G. D'Ippolito, P. C. Schiller, C. Ricordi, B. A. Roos, and G. A. Howard. Age-related osteogenic potential of mesenchymal stromal stem cells from human vertebral bone marrow. *Journal of Bone and Mineral Research*, 14(7):1115–1122, Jul 1999. 5

[42] G. D'Ippolito, S. Diabira, G. A. Howard, P. Menei, B. A. Roos, and P. C. Schiller. Marrow-isolated adult multilineage inducible (MIAMI) cells, a unique population of postnatal young and old human cells with extensive expansion and differentiation potential. *Journal of Cell Science*, 117(14):2971–2981, 2004. 13

[43] G. D'Ippolito, G. A. Howard, B. A. Roos, and P. C. Schiller. Isolation and characterization of marrow-isolated adult multilineage inducible (MIAMI) cells. *Experimental Hematology*, 34(11):1608–1610, Nov 2006. 13, 14

[44] M. R. DiSilvestro, Q. L. Zhu, M. Wong, J. S. Jurvelin, and J. K. F. Suh. Biphasic poroviscoelastic simulation of the unconfined compression of articular cartilage: I - Simultaneous prediction of reaction force and lateral displacement. *Journal of Biomechanical Engineering-Transactions of the ASME*, 123(2):191–197, Apr 2001. 19

[45] R. G. Edwards. Stem cells today: B1. Bone marrow stem cells. *Reproductive Biomedicine Online*, 9(5):541–583, 2004. 7

[46] A. J. Engler, S. Sen, H. L. Sweeney, and D. E. Discher. Matrix elasticity directs stem cell lineage specification. *Cell*, 126(4):677–689, 2006. 14, 29

[47] M. Epstein and G. A. Maugin. Thermomechanics of volumetric growth in uniform bodies. *International Journal of Plasticity*, 16(7-8):951–978, 2000. 20

[48] N. Falla, P. Vanvlasselaer, J. Bierkens, B. Borremans, G. Schoeters, and U. Vangorp. Characterization of a 5-fluorouracil enriched osteoprogenitor population of the murine bone-marrow. *Blood*, 82(12):3580–3591, 1993. 11

[49] B. Fermor, J. Urban, D. Murray, A. Pocock, E. Lim, M. Francis, and J. Gage. Proliferation and collagen synthesis of human anterior cruciate ligament cells in vitro: Effects of ascorbate-2-phosphate, dexamethasone and oxygen tension. *Cell Biology International*, 22(9-10):635–640, 1998. 13

[50] A. R. Fisher. Some effects of different tensions of oxygen on the respiration and growth of l-strain fibroblasts. *Nature*, 186(4721):315–316, 1960. 13

[51] C. Frank, D. Amiel, S. L. Y. Woo, and W. Akeson. Normal ligament properties and ligament healing. *Clinical Orthopaedics and Related Research*, 196:15–25, 1985. 17, 24

[52] R. I. Freshney. *Culture of Animal Cells: A Manual of Basic Technique*. Wiley-Liss, New York, 4th edition, 2000. 13, 29

[53] A. J. Friedenstein, R. K. Chailakh, and K. S. Lalykina. Development of fibroblast colonies in monolayer cultures of guinea-pig bone marrow and spleen cells. *Cell and Tissue Kinetics*, 3(4):393–, 1970. 4, 5, 8

[54] A. J. Friedenstein, A. A. Ivanovsmolenski, R. K. Chailakhyan, U. F. Gorskaja, A. I. Kuralesova, N. W. Latzinik, and U. W. Gerasimow. Origin of bone-marrow stromal mechanocytes in radiochimeras and heterotopic transplants. *Experimental Hematology*, 6(5):440–444, 1978. 4, 6

[55] A. J. Friedenstein, R. K. Chailakh, and U. W. Gerasimov. Bone-marrow osteogenic stem-cells - Invitro cultivation and transplantation in diffusion-chambers. *Cell and Tissue Kinetics*, 20(3):263–272, May 1987. 2

[56] Y. C. Fung. *Biomechanics: Mechanical Properties of Living Tissues*. Springer-Verlag, New York, 1993. 16, 18

[57] J. Z. Gao, J. E. Dennis, L. A. Solchaga, A. S. Awadallah, V. M. Goldberg, and A. I. Caplan. Tissue-engineered fabrication of an osteochondral composite graft using rat bone marrow-derived mesenchymal stem cells. *Tissue Engineering*, 7 (4):363–371, 2001. 2

[58] K. Garikipati, E. M. Arruda, K. Grosh, H. Narayanan, and S. Calve. A continuum treatment of growth in biological tissue: The coupling of mass transport and mechanics. *Journal of the Mechanics and Physics of Solids*, 52(7):1595–1625, 2004. 19, 20

[59] K. Garikipati, J. E. Olberding, H. Narayanan, E. M. Arruda, K. Grosh, and S. Calve. Biological remodelling: Stationary energy, configuration change, internal variables and dissipation. *Journal of the Mechanics and Physics of Solids*, 54(7):1493–1515, Jul 2006. 21, 33

[60] K. Garikipati, S. Göktepe, and C. Miehe. Elastica-based strain energy functions for soft biological tissue. *Journal of the Mechanics and Physics of Solids*, 56(4):1693–1713, Apr 2008. doi: {10.1016/j.jmps.2007.07.005}. 16

[61] E. Gentleman, G. A. Livesay, K. C. Dee, and E. A. Nauman. Development of ligament-like structural organization and properties in cell-seeded collagen scaffolds in vitro. *Annals of Biomedical Engineering*, 34(5):726–736, 2006. 31

[62] J. C. H. Goh, H. W. Ouyang, S. H. Teoh, C. K. C. Chan, and E. H. Lee. Tissue-engineering approach to the repair and regeneration of tendons and ligaments. *Tissue Engineering*, 9:S31–S44, 2003. 2, 15

[63] J. L. Grant and B. Smith. Bone marrow gas tensions, bone marrow blood flow, and erythropoiesis in man. *Annals of Internal Medicine*, 58(5):801–, 1963. 13

[64] D. L. Gumucio. CDB 683 – Organogenesis of complex tissues: Stem cell biology. Lecture notes, Fall 2006. 10

[65] M. Hairfield-Stein, C. England, H. J. Paek, K. B. Gilbraith, , R. Dennis, E. Boland, and P. Kosnik. Development of self-assembled, tissue-engineered ligament from bone marrow stromal cells. *Tissue Engineering*, 13(4):703–710, 2007. 2

[66] K. A. Hansen, J. A. Weiss, and J. K. Barton. Recruitment of tendon crimp with applied tensile strain. *Journal of Biomechanical Engineering-Transactions of the ASME*, 124(1):72–77, 2002. 25

[67] L. Hayflick. Limited in vitro lifetime of human diploid cell strains. *Experimental Cell Research*, 37(3):614–, 1965. 7, 13

[68] S. E. Haynesworth, J. Goshima, V. M. Goldberg, and A. I. Caplan. Characterization of cells with osteogenic potential from human marrow. *Bone*, 13(1): 81–88, 1992. 5

[69] F. L. Hefti, A. Kress, J. Fasel, and E. W. Morscher. Healing of the transected anterior cruciate ligament in the rabbit. *Journal of Bone and Joint Surgery-American Volume*, 73A(3):373–383, Mar 1991. 1

[70] D. F. Holmes, M. J. Capaldi, and J. A. Chapman. Reconstitution of collagen fibrils invitro - the assembly process depends on the initiating procedure. *International Journal of Biological Macromolecules*, 8(3):161–166, 1986. 25

[71] G. A. Holzapfel, T. C. Gasser, and R. W. Ogden. A new constitutive framework for arterial wall mechanics and a comparative study of material models. *Journal of Elasticity*, 61(1-3):1–48, 2000. 18

[72] C. Y. C. Huang, K. L. Hagar, L. E. Frost, Y. B. Sun, and H. S. Cheung. Effects of cyclic compressive loading on chondrogenesis of rabbit bone-marrow derived mesenchymal stem cells. *Stem Cells*, 22(3):313–323, 2004. 30

[73] Y. C. Huang, R. G. Dennis, L. Larkin, and K. Baar. Rapid formation of functional muscle in vitro using fibrin gels. *Journal of Applied Physiology*, 98 (2):706–713, 2005. 2

[74] J. D. Humphrey. Continuum biomechanics of soft biological tissues. *Proceedings of the Royal Society of London Series A-Mathematical Physical and Engineering Sciences*, 459(2029):3–46, 2003. 14

[75] S. C. Hung, N. J. Chen, S. L. Hsieh, H. Li, H. L. Ma, and W. H. Lo. Isolation and characterization of size-sieved stem cells from human bone marrow. *Stem Cells*, 20(3):249–258, 2002. 6

[76] J. G. Hunter, M. F. van Delft, R. A. Rachubinski, and J. P. Capone. Peroxisome proliferator-activated receptor gamma ligands differentially modulate muscle cell differentiation and MyoD gene expression via peroxisome proliferator-activated receptor gamma -dependent and -independent pathways. *Journal of Biological Chemistry*, 276(41), Oct 2001. 13

[77] R. Huss. Perspectives on the morphology and biology of CD34-negative stem cells. *Journal of Hematotherapy & Stem Cell Research*, 9(6):783–793, Dec 2000. 6

[78] J. M. Ingraham, R. M. Hauck, and H. P. Ehrlich. Is the tendon embryogenesis process resurrected during tendon healing? *Plastic and Reconstructive Surgery*, 112(3):844–854, Sep 2003. doi: {10.1097/01.PRS.0000070180.62037.FC}. 18

[79] B. C. Isenberg and R. T. Tranquillo. Long-term cyclic distention enhances the mechanical properties of collagen-based media-equivalents. *Annals of Biomedical Engineering*, 31(8):937–949, 2003. 30

[80] Y. Ishikawa and T. Ito. Kinetics of hematopoietic stem-cells in a hypoxic culture. *European Journal of Haematology*, 40(2):126–129, FEB 1988. 13

[81] E. H. Javazon, K. J. Beggs, and A. W. Flake. Mesenchymal stem cells: Paradoxes of passaging. *Experimental Hematology*, 32(5):414–425, MAY 2004. doi: {10.1016/j.exphem.2004.02.004}. 2, 6

[82] G. A. Johnson, G. A. Livesay, S. L. Y. Woo, and K. R. Rajagopal. A single integral finite strain viscoelastic model of ligaments and tendons. *Journal of Biomechanical Engineering-Transactions of the ASME*, 118(2):221–226, May 1996. 19

[83] B. Josso, D. R. Burton, and M. J. Lalor. Texture orientation and anisotropy calculation by fourier transform and principal component analysis. *Mechanical Systems and Signal Processing*, 19(5):1152–1161, 2005. 26

[84] W. J. Karlon, J. W. Covell, A. D. McCulloch, J. J. Hunter, and J. H. Omens. Automated measurement of myofiber disarray in transgenic mice with ventricular expression of ras. *Anatomical Record*, 252(4):612–625, 1998. 27

[85] W. J. Karlon, P. P. Hsu, S. Li, S. Chien, A. D. McCulloch, and J. H. Omens. Measurement of orientation and distribution of cellular alignment and cytoskeletal organization. *Annals of Biomedical Engineering*, 27(6):712–720, 1999. 27

[86] H. Ernst Keller, James B. Pawley, and Anonymous. *Objective Lenses For Confocal Microscopy*, volume Revised, pages 77–86. Plenum, New York, 1990. ISBN 0-306-43538-1. 25

[87] R. M. Kenedi. Bio-engineering - Concepts trend + potential. *Nature*, 202(493): 334–, 1964. 16

[88] A. Kessinger and J. G. Sharp. The whys and hows of hematopoietic progenitor and stem cell mobilization. *Bone Marrow Transplantion*, 31(5), Mar 2003. 13

[89] B. Kinner, J. M. Zaleskas, and M. Spector. Regulation of smooth muscle actin expression and contraction in adult human mesenchymal stem cells. *Experimental Cell Research*, 278(1):72–83, Aug 2002. 9

[90] R. F. Klees, R. M. Salasznyk, K. Kingsley, W. A. Williams, A. Boskey, and G. E. Plopper. Laminin-5 induces osteogenic gene expression in human mesenchymal stem cells through an erk-dependent pathway. *Molecular Biology of the Cell*, 16(2):881–890, Feb 2005. 12

[91] H. Kofoed, E. Sjøntoft, S. O. Siemssen, and H. P. Olesen. Bone-marrow circulation after osteotomy - Blood-flow, pO_2, pCO_2, and pressure studied in dogs. *Acta Orthopaedica Scandinavica*, 56(5):400–403, 1985. 13

[92] P. E. Kosnik, J. A. Faulkner, and R. G. Dennis. Functional development of engineered skeletal muscle from adult and neonatal rats. *Tissue Engineering*, 7(5):573–584, 2001. 2

[93] L. Kostogiannis, E. Ageberg, P. Neuman, L. Dahlberg, T. Friden, and Harald Roos. Activity level and subjective knee function 15 years after anterior cruciate ligament injury - A prospective, longitudinal study of non reconstructed patients. *American Journal of Sports Medicine*, 35(7):1135–1143, JUL 2007. doi: {10.1177/0363546507299238}. 2

[94] O. Kostyuk and R. A. Brown. Novel spectroscopic technique for in situ monitoring of collagen fibril alignment in gels. *Biophysical Journal*, 87(1):648–655, 2004. 25

[95] P. L. Kronick and M. S. Sacks. Quantification of vertical-fiber defect in cattle hide by small-angle light-scattering. *Connective Tissue Research*, 27(1):1–13, 1991. 27

[96] L. Kunz-Schughart, J. Doetsch, W. Mueller-Klieser, and K. Groebe. Proliferative activity and tumorigenic conversion: Impact on cellular metabolism in 3-D culture. *American Journal of Physiology-Cell Physiology*, 278(4):C765–C780, Apr 2000. 29

[97] M. T. Lam, S. Sim, X. Y. Zhu, and S. Takayama. The effect of continuous wavy micropatterns on silicone substrates on the alignment of skeletal muscle myoblasts and myotubes. *Biomaterials*, 27(24):4340–4347, 2006. 2

[98] M. Lammi and M. Tammi. Densitometric assay of nanogram quantities of proteoglycans precipitated on nitrocellulose membrane with Safranin-O. *Analytical Biochemistry*, 168(2):352–357, Feb 1988. 8

[99] Y. Lanir. Constitutive-equations for fibrous connective tissues. *Journal of Biomechanics*, 16(1):1–12, 1983. 17

[100] L. M. Larkin, S. Calve, T. Y. Kostrominova, and E. M. Arruda. Structure and functional evaluation of tendon-skeletal muscle constructs engineered in vitro. *Tissue Engineering*, 12(11):3149–3158, 2006. 2

[101] K. Le Blanc, I. Rasmusson, B. Sundberg, C. Gotherstrom, M. Hassan, M. Uzunel, and O. Ringden. Treatment of severe acute graft-versus-host disease with third party haploidentical mesenchymal stem cells. *Lancet*, 363 (9419):1439–1441, May 2004. 2

[102] D. P. Lennon and A. I. Caplan. Isolation of human marrow-derived mesenchymal stem cells. *Experimental Hematology*, 34(11):1604–1605, 2006. 5

[103] D. P. Lennon, S. E. Haynesworth, R. G. Young, J. E. Dennis, and A. I. Caplan. A chemically-defined medium supports in-vitro proliferation and maintains the osteochondral potential of rat marrow-derived mesenchymal stem-cells. *Experimental Cell Research*, 219(1):211–222, Jul 1995. 3

[104] D. P. Lennon, S. E. Haynesworth, S. P. Bruder, N. Jaiswal, and A. I. Caplan. Human and animal mesenchymal progenitor cells from bone marrow: Identification of serum for optimal selection and proliferation. *In Vitro Cellular & Developmental Biology-Animal*, 32(10):602–611, 1996. 11

[105] D. P. Lennon, J. M. Edmison, and A. I. Caplan. Cultivation of rat marrow-derived mesenchymal stem cells in reduced oxygen tension: Effects on in vitro and in vivo osteochondrogenesis. *Journal of Cellular Physiology*, 187(3):345–355, 2001. 13

[106] I. K. Y. Lo, L. Marchuk, D. A. Hart, and C. B. Frank. Messenger ribonucleic acid levels in disrupted human anterior cruciate ligaments. *Clinical Orthopaedics and Related Research*, (407):249–258, Feb 2003. 15

[107] R. M. Locklin, R. O. C. Oreffo, and J. T. Triffitt. Effects of TGF beta and bFGF on the differentiation of human bone marrow stromal fibroblasts. *Cell Biology International*, 23(3):185–194, 1999. 12

[108] H. Lodish, A. Berk, P. Matsudaira, C. A. Kaiser, M. Krieger, M. P. Scott, S. L. Zipursky, and J. Darnell. *Molecular Cell Biology*. W. H. Freeman, 5th edition, 2004. 14, 24

[109] L. Stefan Lohmander, P. Martin Englund, Ludvig L. Dahl, and Ewa M. Roos. The long-term consequence of anterior cruciate ligament and meniscus injuries: Osteoarthritis. *American Journal of Sports Medicine*, 35(10), Oct 2007. 1

[110] J. Ma, K. Goble, M. Smietana, T. Kostrominova, L. Larkin, and E. M. Arruda. Morphological and functional characteristics of three-dimensional engineered bone-ligament-bone constructs following implantation. *Journal of Biomechanical Engineering-Transactions of the ASME*, 131(10), OCT 2009. doi: {10.1115/1.4000151}. 2, 3

[111] A. M. Mackay, S. C. Beck, J. M. Murphy, F. P. Barry, C. O. Chichester, and M. F. Pittenger. Chondrogenic differentiation of cultured human mesenchymal stem cells from marrow. *Tissue Engineering*, 4(4):415–428, Win 1998. 11

[112] A. K. Majors, C. A. Boehm, H. Nitto, R. J. Midura, and G. F. Muschler. Characterization of human bone marrow stromal cells with respect to osteoblastic differentiation. *Journal of Orthopaedic Research*, 15(4):546–557, Jul 1997. 5

[113] M. K. Majumdar, V. Banks, D. P. Peluso, and E. A. Morris. Isolation, characterization, and chondrogenic potential of human bone marrow-derived multipotential stromal cells. *Journal of Cellular Physiology*, 185(1):98–106, Oct 2000. 6

[114] A. F. Mak. The apparent viscoelastic behavior of articular-cartilage - The contributions from the intrinsic matrix viscoelasticity and interstitial fluid-flows. *Journal of Biomechanical Engineering-Transactions of the ASME*, 108 (2):123–130, May 1986. 19

[115] R. McBeath, D. M. Pirone, C. M. Nelson, K. Bhadriraju, and C. S. Chen. Cell shape, cytoskeletal tension, and RhoA regulate stem cell lineage commitment. *Developmental Cell*, 6(4):483–495, 2004. 8, 14, 29

[116] D. J. Mcbride, R. L. Trelstad, and F. H. Silver. Structural and mechanical assessment of developing chick tendon. *International Journal of Biological Macromolecules*, 10(4):194–200, 1988. 23

[117] C. A. G. McCulloch and H. C. Tenenbaum. Dexamethasone induces proliferation and terminal differentiation of osteogenic cells in tissue-culture. *Anatomical Record*, 215(4):397–402, Aug 1986. 11

[118] L. D. Meirelles and N. B. Nardi. Murine marrow-derived mesenchymal stem cell: Isolation, in vitro expansion, and characterization. *British Journal of Haematology*, 123(4):702–711, Nov 2003. 5

[119] E. Mezey, K. J. Chandross, G. Harta, R. A. Maki, and S. R. McKercher. Turning blood into brain: Cells bearing neuronal antigens generated in vivo from bone marrow. *Science*, 290(5497):1779–1782, Dec 2000. 3

[120] K. Misof, G. Rapp, and P. Fratzl. A new molecular model for collagen elasticity based on synchrotron X-ray scattering evidence. *Biophysical Journal*, 72(3): 1376–1381, 1997. 25

[121] K. C. Miyasaka, D. Daniel, and P. Hirschman. The incidence of knee ligament injuries in the general population. *American Journal of Knee Surgery*, 4:3–8, 1991. 1

[122] A. Mohraz and M. J. Solomon. Direct visualization of colloidal rod assembly by confocal microscopy. *Langmuir*, 21(12):5298–5306, 2005. 26

[123] J. E. Moreau, J. S. Chen, D. S. Bramono, V. Volloch, H. Chernoff, G. Vunjak-Novakovic, J. C. Richmond, D. L. Kaplan, and G. H. Altman. Growth factor induced fibroblast differentiation from human bone marrow stromal cells in vitro. *Journal of Orthopaedic Research*, 23(1):164–174, 2005. 12, 28

[124] J. E. Moreau, J. S. Chen, R. L. Horan, D. L. Kaplan, and G. H. Altman. Sequential growth factor application in bone marrow stromal cell ligament engineering. *Tissue Engineering*, 11(11-12):1887–1897, 2005. 28

[125] V. C. Mow, S. C. Kuei, W. M. Lai, and C. G. Armstrong. Biphasic creep and stress-relaxation of articular-cartilage in compression - Theory and experiments. *Journal of Biomechanical Engineering-Transactions of the ASME*, 102 (1):73–84, 1980. 19

[126] N. D. Murchison, B. A. Price, D. A. Conner, D. R. Keene, E. N. Olson, C. J. Tabin, and R. Schweitzer. Regulation of tendon differentiation by scleraxis distinguishes force-transmitting tendons from muscle-anchoring tendons. *Development*, 134(14):2697–2708, Jul 2007. 9

[127] M. M. Murray and M. Spector. Fibroblast distribution in the anteromedial bundle of the human anterior cruciate ligament: The presence of alpha-smooth muscle actin-positive cells. *Journal of Orthopaedic Research*, 17(1):18–27, Jan 1999. 9

[128] G. E. Muschler, C. Nakamoto, and L. G. Griffith. Engineering principles of clinical cell-based tissue engineering. *Journal of Bone and Joint Surgery-American Volume*, 86A(7):1541–1558, Jul 2004. 29

[129] G. F. Muschler, C. Boehm, and K. Easley. Aspiration to obtain osteoblast progenitor cells from human bone marrow: The influence of aspiration volume. *Journal of Bone and Joint Surgery-American Volume*, 79A(11):1699–1709, Nov 1997. 5

[130] P. Neuman, M. Englund, I. Kostogiannis, T. Friden, H. Roos, and L. E. Dahlberg. Prevalence of tibiofemoral osteoarthritis 15 years after nonoperative treatment of anterior cruciate ligament injury: A prospective cohort study. *American Journal of Sports Medicine*, 36(9), Sep 2008. 1

[131] M. E. Nimni and R. D. Harkness. *Collagen: Biochemistry*, volume 1, chapter Molecular structures and functions of collagen. CRC Press, Cleveland, 1988. 9, 15

[132] F. R. Noyes and E. S. Grood. Strength of anterior cruciate ligament in humans and rhesus-monkeys. *Journal of Bone and Joint Surgery-American Volume*, 58 (8):1074–1082, 1976. 16

[133] K. C. O'Connor, H. Song, N. Rosenzweig, and D. A. Jansen. Extracellular matrix substrata alter adipocyte yield and lipogenesis in primary cultures of stromal-vascular cells from human adipose. *Biotechnology Letters*, 25(23): 1967–1972, Dec 2003. 12

[134] B. E. Øiestad, L. Engebretsen, K. Storheim, and M. A. Risberg. Knee osteoarthritis after anterior cruciate ligament injury: A systematic review. *American Journal of Sports Medicine*, 37(7), Jul 2009. 1

[135] J. E. Olberding, K. Garikipati, E. Kuhl, K. Grosh, and E. M. Arruda. Thermodynamic considerations for remodeling in biological tissue. In *Proceedings of the Eighth U.S. National Congress on Computational Mechanics*, Austin, TX, July 2005. 33

[136] J. E. Olberding, K. Garikipati, E. M. Arruda, and K. Garikipati. Fibroblast-mediated collagen fibril reorientation in three dimensions using confocal reflection microscopy. In *Proceedings of the 15th U.S. National Congress on Theoretical and Applied Mechanics*, Boulder, CO, June 2006. 33

[137] J. E. Olberding, K. Grosh, E. M. Arruda, and K. Garikipati. Quantification of collagen fibril reorientation in volumetric image data by confocal microscopy. In *Proceedings of the Biomedical Engineering Society 2006 Annual Fall Meeting*, Chicago, IL, October 2006. 33

[138] J. E. Olberding, M. D. Thouless, E. M. Arruda, and K. Garikipati. Focal adhesion dynamics: Reaction domination. In *Proceedings of the Biomedical Engineering Society 2007 Annual Fall Meeting*, Los Angeles, CA, September 2007. 33

[139] J. E. Olberding, K. Garikipati, K. Grosh, L. M. Larkin, and E. M. Arruda. Role of oxygen content on the fibrogenesis of bone marrow stromal cells. In *Proceedings of the Biomedical Engineering Society 2009 Annual Fall Scientific Meeting*, Pittsburgh, PA, October 2009. 33

[140] J. E. Olberding, K. Garikipati, K. Grosh, L. M. Larkin, and E. M. Arruda. Effect of oxygen on the fibrogenesis and parallel-fibered engineered tissue potential of bone marrow stem cells and fibroblasts. In preparation, 2010. 33

[141] J. E. Olberding, K. Grosh, E. M. Arruda, and K. Garikipati. Fiber reorientation and fusion and maximum thermodynamic dissipation. In preparation, 2010. 33

[142] J. E. Olberding, M. D. Thouless, E. M. Arruda, and K. Garikipati. The non-equilibrium thermodynamics and kinetics of focal adhesion dynamics. Submitted, 2010. 33

[143] J. E. Olberding, M. D. Thouless, E. M. Arruda, and K. Garikipati. A theoretical study of the thermodynamics and kinetics of focal adhesion dynamics. In Garikipati, K and Arruda, EM, editor, *IUTAM Symposium on Cellular, Molecular and Tissue Mechanics, Proceedings*, volume 16 of *IUTAM Bookseries*, pages 181–192. Springer, New York, 2010. doi: {10.1007/978-90-481-3348-2\ _15}. 33

[144] A. Oldberg, A. Franzen, and D. Heinegard. Cloning and sequence-analysis of rat bone sialoprotein (osteopontin) cDNA reveals an Arg-Gly-Asp cell-binding sequence. *Proceedings of the National Academy of Sciences of the United States of America*, 83(23):8819–8823, Dec 1986. 9

[145] R. Oldenbourg, H. Terada, R. Tiberio, and S. Inoue. Image sharpness and contrast transfer in coherent confocal microscopy. *Journal of Microscopy-Oxford*, 172:31–39, 1993. 25

[146] M. F. Owings and Kozak L. J. Ambulatory and inpatient procedures in the United States, 1996. *Vital Health Statistics 13*, 139:1–119, 1998. 1

[147] B. M. Palmer and R. Bizios. Quantitative characterization of vascular endothelial cell morphology and orientation using fourier transform analysis. *Journal of Biomechanical Engineering-Transactions of the ASME*, 119(2):159–165, 1997. 27

[148] J. S. Park, J. S. F. Chu, C. Cheng, F. Q. Chen, D. Chen, and S. Li. Differential effects of equiaxial and uniaxial strain on mesenchymal stem cells. *Biotechnology and Bioengineering*, 88(3):359–368, Nov 2004. 14

[149] S. Parrinello, E. Samper, A. Krtolica, J. Goldstein, S. Melov, and J. Campisi. Oxygen sensitivity severely limits the replicative lifespan of murine fibroblasts. *Nature Cell Biology*, 5(8), Aug 2003. 13

[150] E. Pennisi. Tending tender tendons. *Science*, 295(5557):1011–1011, Feb 2002. 1

[151] F. A. Petrigliano, D. R. McAllister, and B. M. Wu. Tissue engineering for anterior cruciate ligament reconstruction: A review of current strategies. *Arthroscopy-the Journal of Arthroscopic and Related Surgery*, 22(4):441–451, 2006. 27

[152] W. M. Petroll, H. D. Cavanagh, P. Barry, P. Andrews, and J. V. Jester. Quantitative-analysis of stress fiber orientation during corneal wound contraction. *Journal of Cell Science*, 104:353–363, 1993. 27

[153] D. G. Phinney, G. Kopen, R. L. Isaacson, and D. J. Prockop. Plastic adherent stromal cells from the bone marrow of commonly used strains of inbred mice: Variations in yield, growth, and differentiation. *Journal of Cellular Biochemistry*, 72(4):570–585, 1999. 5, 11

[154] M. F. Pittenger, A. M. Mackay, S. C. Beck, R. K. Jaiswal, R. Douglas, J. D. Mosca, M. A. Moorman, D. W. Simonetti, S. Craig, and D. R. Marshak. Multilineage potential of adult human mesenchymal stem cells. *Science*, 284(5411): 143–147, 1999. 7, 12

[155] A. M. Pizzo, K. Kokini, L. C. Vaughn, B. Z. Waisner, and S. L. Voytik-Harbin. Extracellular matrix (ECM) microstructural composition regulates local cell-ECM biomechanics and fundamental fibroblast behavior: a multidimensional perspective. *Journal of Applied Physiology*, 98(5):1909–1921, 2005. 25

[156] D. J. Prockop. Marrow stromal cells as stem cells for nonhematopoietic tissues. *Science*, 276(5309):71–74, 1997. 2, 11

[157] P. Provenzano, R. Lakes, T. Keenan, and R. Vanderby. Nonlinear ligament viscoelasticity. *Annals of Biomedical Engineering*, 29(10):908–914, Oct 2001. 16, 18

[158] P. P. Provenzano and R. Vanderby. Collagen fibril morphology and organization: Implications for force transmission in ligament and tendon. *Matrix Biology*, 25(2):71–84, 2006. 15

[159] B. A. Pryce, A. E. Brent, N. D. Murchison, C. J. Tabin, and R. Schweitzer. Generation of transgenic tendon reporters, scxgfp and scxap, using regulatory elements of the scleraxis gene. *Developmental Dynamics*, 236(6):1677–1682, Jun 2007. 10

[160] K. M. Quapp and J. A. Weiss. Material characterization of human medial collateral ligament. *Journal of Biomechanical Engineering-Transactions of the ASME*, 120(6):757–763, 1998. 17

[161] C. Redon, L. Chermant, J. L. Chermant, and M. Coster. Assessment of fibre orientation in reinforced concrete using fourier image transform. *Journal of Microscopy-Oxford*, 191:258–265, 1998. 26

[162] B. Reider, M. R. Sathy, J. Talkington, N. Blyznak, and S. Kollias. Treatment of isolated medial collateral ligament injuries in athletes with early functional rehabilitation - A 5-year follow-up-study. *American Journal of Sports Medicine*, 22(4):470–477, Jul-Aug 1994. 1

[163] R. S. Rivlin. Large elastic deformations of isotropic materials. I. Fundamental concepts. *Philosophical Transactions of the Royal Society of London Series A-Mathematical and Physical Sciences*, 240(822):459–508, Large Elastic Deformations of Isotropic Materials. I. Fundamental Concepts 1948. 16

[164] B. A. Roeder, K. Kokini, J. P. Robinson, and S. L. Voytik-Harbin. Local, three-dimensional strain measurements within largely deformed extracellular matrix constructs. *Journal of Biomechanical Engineering-Transactions of the ASME*, 126(6):699–708, 2004. 26

[165] M. S. Sacks, D. B. Smith, and E. D. Hiester. A small angle light scattering device for planar connective tissue microstructural analysis. *Annals of Biomedical Engineering*, 25(4):678–689, 1997. 25

[166] H. K. Salem and C. Thiemermann. Mesenchymal stromal cells: Current understanding and clinical status. *Stem Cells*, 28(3):585–596, Mar 2010. doi: {10.1002/stem.269}. 5, 6

[167] W. M. Saltzman, S. H. Pasternak, and R. Langer. Quantitative image-analysis for developing microstructural descriptions of heterogeneous materials. *Chemical Engineering Science*, 42(8):1989–2004, 1987. 26

[168] A. A. H. J. Sauren, W. Kuijpers, A. A. Vansteenhoven, and F. E. Veldpaus. Aortic-Valve Histology And Its Relation With Mechanics - Preliminary-Report. *Journal of Biomechanics*, 13(2):97–104, 1980. 18

[169] R. Schweitzer, J. H. Chyung, L. C. Murtaugh, A. E. Brent, V. Rosen, E. N. Olson, A. Lassar, and C. J. Tabin. Analysis of the tendon cell fate using scleraxis, a specific marker for tendons and ligaments. *Development*, 128(19): 3855–3866, Oct 2001. 9

[170] D. Seliktar, R. A. Black, R. P. Vito, and R. M. Nerem. Dynamic mechanical conditioning of collagen-gel blood vessel constructs induces remodeling in vitro. *Annals of Biomedical Engineering*, 28(4):351–362, 2000. 30

[171] D. Seliktar, R. M. Nerem, and Z. S. Galis. Mechanical strain-stimulated remodeling of tissue-engineered blood vessel constructs. *Tissue Engineering*, 9 (4):657–666, 2003. 30

[172] J. L. Semple, N. Woolridge, and C. J. Lumsden. In vitro, in vivo, in silico: Computational systems in tissue engineering and regenerative medicine. *Tissue Engineering*, 11(3-4):341–356, 2005. 3

[173] B. Seshi, S. Kumar, and D. Sellers. Human bone marrow stromal cell: Coexpression of markers specific for multiple mesenchymal cell lineages. *Blood Cells Molecules and Diseases*, 26(3):234–246, Jun 2000. 5, 6

[174] H. Shin, J. S. Temenoff, G. C. Bowden, K. Zygourakis, M. C. Farach-Carson, M. J. Yaszemski, and A. G. Mikos. Osteogenic differentiation of rat bone marrow stromal cells cultured on arg-gly-asp modified hydrogels without dexamethasone and beta-glycerol phosphate. *Biomaterials*, 26(17):3645–3654, Jun 2005. 12

[175] R. S. Siffert. The role of alkaline phosphatase in osteogenesis. *Journal of Experimental Medicine*, 93(5):415–, 1951. 9

[176] F. H. Silver, L. M. Siperko, and G. P. Seehra. Mechanobiology of force transduction in dermal tissue. *Skin Research and Technology*, 9(1):3–23, 2003. 18

[177] P. J. Simmons and B. Torokstorb. Identification of stromal cell precursors in human bone-marrow by a novel monoclonal-antibody, STRO-1. *Blood*, 78(1): 55–62, 1991. 7

[178] D. G. Simpson, M. Majeski, T. K. Borg, and L. Terracio. Regulation of cardiac myocyte protein turnover and myofibrillar structure in vitro by specific directions of stretch. *Circulation Research*, 85(10):E59–E69, 1999. 17, 24

[179] M. J. Smietana, F. N. Syed-Picard, J. Ma, T. Kostrominova, E. M. Arruda, and L. M. Larkin. The effect of implantation on scaffoldless three-dimensional engineered bone constructs. *In Vitro Cellular & Developmental Biology-Animal*, 45(9):512–522, SEP 2009. doi: {10.1007/s11626-009-9216-3}. 2, 3

[180] J. F. H. Smith, P. B. Canham, and J. Starkey. Orientation of collagen in the tunica adventitia of the human cerebral-artery measured with polarized-light and the universal stage. *Journal of Ultrastructure Research*, 77(2):133–145, 1981. 25

[181] J. R. Smith, R. Pochampally, A. Perry, S. C. Hsu, and D. J. Prockop. Isolation of a highly clonogenic and multipotential subfraction of adult stem cells from bone marrow stroma. *Stem Cells*, 22(5):823–831, 2004. 7

[182] H. Song, K. C. O'Connor, K. D. Papadopoulos, and D. A. Jansen. Differentiation kinetics of in vitro 3T3-l1 preadipocyte cultures. *Tissue Engineering*, 8 (6):1071–1081, Dec 2002. 11

[183] G. J. Spangrude, S. Heimfeld, and I. L. Weissman. Purification and characterization of mouse hematopoietic stem-cells. *Science*, 241(4861):58–62, Jul 1988. 6

[184] B. M. Spiegelman and C. A. Ginty. Fibronectin modulation of cell-shape and lipogenic gene-expression in 3t3-adipocytes. *Cell*, 35(3):657–666, 1983. 12

[185] K. P. Spindler, J. M. Dawson, G. C. Stahlman, J. M. Davidson, and L. B. Nanney. Collagen expression and biomechanical response to human recombinant transforming growth factor beta (rhTGF-beta 2) in the healing rabbit mcl. *Journal of Orthopaedic Research*, 20(2):318–324, Mar 2002. 1

[186] G. R. Srinivas, C. O. Chichester, H. J. Barrach, V. Pillai, and A. L. Matoney. Production of Type-II collagen specific monoclonal-antibodies. *Immunological Investigations*, 23(2):85–98, 1994. 9

[187] D. Stopak and A. K. Harris. Connective-tissue morphogenesis by fibroblast traction: I. Tissue-culture observations. *Developmental Biology*, 90(2):383–398, 1982. 21, 24, 25

[188] L. Studer, M. Csete, S. H. Lee, N. Kabbani, J. Walikonis, B. Wold, and R. McKay. Enhanced proliferation, survival, and dopaminergic differentiation of CNS precursors in lowered oxygen. *Journal of Neuroscience*, 20(19): 7377–7383, Oct 2000. 13

[189] F. N. Syed-Picard, L. M. Larkin, C. M. Shaw, and E. M. Arruda. Three-dimensional engineered bone from bone marrow stromal cells and their autogenous extracellular matrix. *Tissue Engineering Part A*, 15(1):187–195, Jan 2009. doi: {10.1089/ten.tea.2007.0140}. 3

[190] A. Takashima. Establishment of fibroblast cultures. In J. S. Bonifacino, M. Dasso, J. B. Harford, J. Lippincott-Schwartz, and K. M. Yamada, editors, *Current Protocols in Cell Biology*, Current Protocols, chapter 2.1. Wiley, 1998. 9

[191] S. Thomopoulos, G. M. Fomovsky, and J. W. Holmes. The development of structural and mechanical anisotropy in fibroblast populated collagen gels. *Journal of Biomechanical Engineering-Transactions of the ASME*, 127(5):742–750, 2005. 27

[192] G. M. Thornton, C. B. Frank, and N. G. Shrive. Ligament creep behavior can be predicted from stress relaxation by incorporating fiber recruitment. *Journal of Rheology*, 45(2):493–507, Mar-Apr 2001. 19

[193] T. T. Tower, M. R. Neidert, and R. T. Tranquillo. Fiber alignment imaging during mechanical testing of soft tissues. *Annals of Biomedical Engineering*, 30(10):1221–1233, 2002. 25

[194] E. E. Underwood. *Stereology*. Addison-Wesley, Reading, MA, 1970. 26

[195] F. Van Eijk, D. B. F. Saris, J. Riesle, W. J. Willems, C. A. Van Blitter-swijk, A. J. Verbout, and W. J. A. Dhert. Tissue engineering of ligaments: A comparison of bone marrow stromal cells, anterior cruciate ligament, and skin fibroblasts as cell source. *Tissue Engineering*, 10(5-6):893–903, 2004. 28

[196] P. Vanvlasselaer, N. Falla, H. Snoeck, and E. Mathieu. Characterization and purification of osteogenic cells from murine bone-marrow by 2-color cell sorting using anti-SCA-1 monoclonal-antibody and wheat-germ-agglutinin. *Blood*, 84 (3):753–763, 1994. 7

[197] G. Vogel. Stem cells - 'Stemness' genes still elusive. *Science*, 302(5644):371–371, Oct 2003. 6

[198] G. Vunjak-Novakovic, G. Altman, R. Horan, and D. L. Kaplan. Tissue engineering of ligaments. *Annual Review of Biomedical Engineering*, 6:131–156, 2004. 27

[199] S. Wakitani, T. Saito, and A. I. Caplan. Myogenic cells derived from rat bone-marrow mesenchymal stem-cells exposed to 5-azacytidine. *Muscle & Nerve*, 18 (12):1417–1426, Dec 1995. 11

[200] J. H. C. Wang, F. Y. Jia, T. W. Gilbert, and S. L. Y. Woo. Cell orientation determines the alignment of cell-produced collagenous matrix. *Journal of Biomechanics*, 36(1):97–102, 2003. 17, 24

[201] J. H. C. Wang, G. G. Yang, and Z. Z. Li. Controlling cell responses to cyclic mechanical stretching. *Annals of Biomedical Engineering*, 33(3):337–342, 2005. 17, 24

[202] Y. N. Wang, C. Galiotis, and D. L. Bader. Determination of molecular changes in soft tissues under strain using laser raman microscopy. *Journal of Biomechanics*, 33(4):483–486, 2000. 25

[203] J. Wei and M. B. Russ. Convection and diffusion in tissues and tissue-cultures. *Journal of Theoretical Biology*, 66(4):775–787, 1977. 29

[204] J. A. Weiss and B. J. Maakestad. Permeability of human medial collateral ligament in compression transverse to the collagen fiber direction. *Journal of Biomechanics*, 39(2):276–283, 2006. 19

[205] W. J. Whitehouse. Quantitative morphology of anisotropic trabecular bone. *Journal of Microscopy-Oxford*, 101(Jul):153–168, 1974. 26

[206] P. Whiteman. Quantitative measurement of alcian blue glycosaminoglycans complexes. *Biochemical Journal*, 131(2):343–350, 1973. 8

[207] S. L. Woo, T. M. Vogrin, and S. D. Abramowitch. Healing and repair of ligament injuries in the knee. *Journal of the American Academy of Orthopaedic Surgeons*, 8(6), Nov-Dec 2000. 1

[208] S. L. Y. Woo, T. Q. Lee, M. A. Gomez, S. Sato, and F. P. Field. Temperature-dependent behavior of the canine medial collateral ligament. *Journal of Biomechanical Engineering-Transactions of the ASME*, 109(1):68–71, Feb 1987. 16

[209] S. L. Y. Woo, R. E. Debski, J. D. Withrow, and M. A. Janaushek. Biomechanics of knee ligaments. *American Journal of Sports Medicine*, 27(4):533–543, Jul-Aug 1999. 30

[210] S. L. Y. Woo, S. D. Abramowitch, R. Kilger, and R. Liang. Biomechanics of knee ligaments: injury, healing, and repair. *Journal of Biomechanics*, 39(1): 1–20, 2006. 1, 9, 14, 15, 28

[211] J. Wu, B. Rajwa, D. L. Filmer, C. M. Hoffmann, B. Yuan, C. S. Chiang, J. Sturgis, and J. P. Robinson. Analysis of orientations of collagen fibers by novel fiber-tracking software. *Microscopy and Microanalysis*, 9(6):574–580, 2003. 26

[212] K. M. Yamada and K. Olden. Fibronectins—adhesive glycoproteins of cell-surface and blood. *Nature*, 275(5677):179–184, 1978. 9, 12

[213] C. F. Yang, C. M. Crosby, A. R. K. Eusufzai, and R. E. Mark. Determination of paper sheet fiber orientation distributions by a laser optical diffraction method. *Journal of Applied Polymer Science*, 34(3):1145–1157, 1987. 26, 27

[214] L. H. Yin and D. M. Elliott. A biphasic and transversely isotropic mechanical model for tendon: application to mouse tall fascicles in uniaxial tension. *Journal of Biomechanics*, 37(6):907–916, 2004. 19

[215] T. Yuhara, M. Hasuike, and K. Murakami. Fiber orientation measurement with the 2-dimensional power spectrum of a high-resolution soft-x-ray image. *Journal of Pulp and Paper Science*, 17(4):J110–J114, 1991. 27

[216] P. W. Zandstra and A. Nagy. Stem cell bioengineering. *Annual Review of Biomedical Engineering*, 3:275–305, 2001. 4

[217] R. Zohar, J. Sodek, and C. A. G. McCulloch. Characterization of stromal progenitor cells enriched by flow cytometry. *Blood*, 90(9):3471–3481, 1997. 7

CHAPTER 2

Mathematical modeling of fiber reorientation and fusion

2.1 Introduction

The case of fiber reorientation is the most ubiquitous in theoretical remodeling studies. These models have the basic structure of a transversely-isotropic constitutive model combined with a strain-based rate equation governing the evolution of a local fiber orientation vector. A simple first-order, principal stretch-driven evolution equation allows for a number of non-trival boundary-value problem simulations [224, 226]. However, current treatments of remodeling phenomena in biological tissue [219, 221] generally do not consider the thermodynamic (first and second law) implications of prescribed evolution equations for internal variables. In the following a thermodynamic investigation of this class of models of fiber remodeling by reorientation and fusion is presented.

2.2 Kinematics of transverse isotropy

Proper anisotropy is a critical feature of many healthy connective tissues. For the parallel-fibered soft tissues, in which only one family of fibers affects directional mechanical behavior at each point in the material, the special unidirectional case of transverse isotropy is appropriate. Here then, the local fiber direction is parametrized by the unit vector field $\mathbf{m}$ (Fig. 2.1):

$$\mathbf{m}(\mathbf{X}, t) = \mathbf{K}(\mathbf{X}, t)\mathbf{m}_0(\mathbf{X}), \quad \mathbf{m}_0, \mathbf{m} \in \Omega_0, \mathbf{K} \in SO(3), \quad \|\mathbf{m}_0\| = \|\mathbf{m}\| = 1. \quad (2.1)$$

By virtue of its time-dependent referential configuration, $\mathbf{m}$ is thus an *internal variable* that determines the instantaneous pointwise principal *material* symmetry axis. The alternative definition of the internal variable as the reorientation tensor $\mathbf{K}$, while not critical to this model of reorientation, denotes in its position dependence that (in general) each infinitesimal neighborhood undergoes an independent rotation (unlike a rigid-body rotation, $\mathbf{Q}(t)$). This microstructural complexity, in turn, illustrates that while the consideration of $\mathbf{m}$-dependent configurational changes is mathematically possible [denoted as Case I remodeling in 222], for the case of fiber reorientation, a compatible constitutive prescription is not straightforward [222, see Remark 4].

Similarly, the remodeling effect of *longitudinal* fiber fusion leading to an increase in the value of an associated material parameter l representing fiber length is defined as

$$l(\mathbf{X}, t) = \lambda(\mathbf{X}, t)l_0(\mathbf{X}) \tag{2.2}$$

Both of these remodeling effects are conveniently combined into a structural tensor $\mathbf{M}$ whereby

$$\mathbf{M}(\mathbf{X}, t) \equiv \bar{\mathbf{m}}(\mathbf{X}, t) \otimes \bar{\mathbf{m}}(\mathbf{X}, t) \qquad \text{and} \qquad \bar{\mathbf{m}} \equiv \lambda(\mathbf{X}, t)\mathbf{m}(\mathbf{X}, t). \tag{2.3}$$

The corresponding strain energy representation typically defines such a hyperelastic, transversely-isotropic material by satisfying

$$W(\mathbf{C}, \mathbf{M}) = W(\mathbf{Q}\mathbf{C}\mathbf{Q}^{\mathrm{T}}, \mathbf{Q}\mathbf{M}\mathbf{Q}^{\mathrm{T}}), \qquad \forall \mathbf{Q} \in SO(3), \mathbf{C} \in \mathrm{Sym}^{+}(3) \qquad (2.4)$$

where W is the strain energy density function per unit reference volume, $\mathbf{C}$ is the usual right Cauchy-Green stretch tensor, and $\mathbf{Q}$ is an arbitrary rigid-body rotation superposed on the reference configuration. As usual, the strain energy Eq. 2.4 is alternatively formulated in terms of scalar invariants with respect to which it is an isotropic function:

$$W(\mathbf{C}, \mathbf{M}) = W(\mathrm{tr}\,\mathbf{C}, J^2, \hat{\lambda}^2) \qquad (2.5)$$

where

$$J^2 = \det \mathbf{C} \qquad\qquad \hat{\lambda}^2 = \mathbf{C} : \mathbf{M}. \qquad (2.6)$$

2.3 Balance laws

In the following, the thermodynamic balance laws are given in the material description and local form. Taking the view that changes in mass are negligible for processes of remodeling , the balance of mass remains the same as for a single phase solid, likewise for the momenta balances. Proceeding directly then to the *balance of energy* sees

$$\dot{e} = \underbrace{\mathbf{P} : \dot{\mathbf{F}}}_{\text{stress power}} - \underbrace{\nabla \cdot \mathbf{q}}_{\text{heat conduction}} \qquad\qquad \nabla \cdot (\bullet) \equiv \mathrm{tr}\,\frac{\partial(\bullet)}{\partial \mathbf{X}} \qquad (2.7)$$

with e the internal energy density and $\mathbf{q}$ the heat flux.

The *entropy inequality* is expressed in balance form as

$$\dot{\eta} = \underbrace{-\nabla \cdot \left(\frac{\mathbf{q}}{\Theta}\right)}_{\text{entropy conduction}} - \underbrace{\gamma}_{\text{entropy production}}, \qquad\qquad \gamma \geq 0, \qquad (2.8)$$

where η is the entropy density and Θ is the temperature. Free energy ψ is introduced with the Legendre transformation

$$\dot{e} = \dot{\psi} + \Theta\dot{\gamma} \qquad\qquad \psi = W + \psi^{\text{chm}} \qquad\qquad (2.9)$$

in which the isothermal ($\dot{\Theta} = 0$) assumption has been used. Note that the local rate of chemical free energy $\dot{\psi}^{\text{chm}}$ is written explicitly for future use. Combining Eq. 2.7, Eq. 2.8, Eq. 2.9, and employing the following additional assumptions

$$\mathbf{q} = \underbrace{-\kappa\nabla\Theta}_{\text{Fourier conduction}} , \qquad \mathbf{P} = \underbrace{\frac{\partial W}{\partial \mathbf{F}}}_{\text{hyperelasticity}} , \qquad W = \underbrace{W(\mathbf{C}, \mathbf{M})}_{\text{transverse isotropy}} ,$$

(with $\nabla(\bullet) \equiv \partial(\bullet)/\partial\mathbf{X}$) yields the *dissipation inequality*:

$$D \equiv \Theta\gamma = \frac{\kappa\|\nabla\Theta\|^2}{\Theta} - (\dot{W}^{\text{rmd}} + \dot{\psi}^{\text{chm}}) \geq 0. \qquad\qquad (2.10)$$

The *remodeling power* $\dot{W}^{\text{rmd}}$ is that portion of the strain energy rate not resulting from the stress power:

$$\dot{W}^{\text{rmd}} \equiv \dot{W} - \mathbf{P} : \dot{\mathbf{F}}$$
$$= \frac{\partial W}{\partial \mathbf{M}} : \dot{\mathbf{M}}, \qquad\qquad (2.11)$$

and results from the non-constant material fiber length and direction. The remodeling power and chemical energy rate, however, are not independent. Knowing that remodeling processes occur by cell traction, a simple relation can be assigned:

$$\dot{W}^{\text{rmd}} = -\beta\dot{\psi}^{\text{chm}}, \qquad\qquad 0 \leq \beta = \text{const} \leq 1, \qquad\qquad (2.12)$$

where β is a constant of proportionality representing the efficiency of energy transfer from cellular ATP storage to the material. Neglecting heat conduction, this leads to

$$D^{\text{rmd}} = \frac{1-\beta}{\beta}\dot{W}^{\text{rmd}} \qquad\qquad (2.13)$$

56

Observe that, for this simple model, remodeling dissipation is proportional to remodeling power, and that the inequality is satisfied identically for *stiffening* ($\dot{W}^{\mathrm{rmd}} > 0$) remodeling laws. Moreover, it is immediately apparent that *a purely mechanical formulation is thermodynamically inadmissible* since the lack of a chemical energy term would violate Eq. 2.10 (without the positive heating term) for the same $\dot{W}^{\mathrm{rmd}}$.

2.4   Evolution equations

To examine the dissipative character of the system further, constitutive relations for fiber remodeling must be specified. For the purposes of this preliminary analysis, a simple first-order reorientation rate equation [224, 226] was convenient (Fig. 2.2):

$$\dot{\mathbf{m}} = \boldsymbol{\omega} \times \mathbf{m} = -\frac{1}{\tau^{\mathrm{rot}}} \left[(\cos \nu) \, \mathbf{m} - \mathbf{n} \right], \tag{2.14}$$

where

$$\dot{\mathbf{m}} \equiv \frac{\partial \mathbf{m}}{\partial t}, \qquad \boldsymbol{\omega} = \frac{\mathbf{m} \times \mathbf{n}}{\tau^{\mathrm{rot}}}, \qquad \|\mathbf{n}\| = 1, \qquad \cos \nu \equiv \mathbf{m} \cdot \mathbf{n}.$$

In words, the pointwise fiber direction rotates according to the axial vector $\boldsymbol{\omega}$ toward a *target direction* $\mathbf{n}$ (to be specified) with an angular velocity proportional to the angle between the fiber and target directions and inversely proportional to a reorientation time constant τ^{rot}. For future use, the reorientation vector $\dot{\mathbf{m}}$ can be decomposed into a direction $\bar{\boldsymbol{\omega}}$ and magnitude $1/\bar{\tau}^{\mathrm{rot}}$:

$$\dot{\mathbf{m}} = \frac{\bar{\boldsymbol{\omega}}(\mathbf{n})}{\bar{\tau}^{\mathrm{rot}}(\nu)}, \qquad \bar{\boldsymbol{\omega}}(\mathbf{n}) \equiv \frac{\dot{\mathbf{m}}(\mathbf{n})}{\|\dot{\mathbf{m}}(\mathbf{n})\|}, \qquad \bar{\tau}^{\mathrm{rot}}(\nu) = \frac{\sin \nu}{\tau^{\mathrm{rot}}}. \tag{2.15}$$

Similarly, an evolution equation for *longitudinal* fiber fusion can be written

$$\dot{\lambda} = \frac{1}{\tau^{\mathrm{fus}}} \begin{cases} \hat{\lambda} - \lambda, & \hat{\lambda} > 1 \\ \\ 0, & \text{otherwise} \end{cases}, \tag{2.16}$$

which simply states that the rate of elongation by fusion is proportional to the (tensile) fiber strain $(\hat{l} - l)$, scaled by a fusion time constant τ^{fus}.
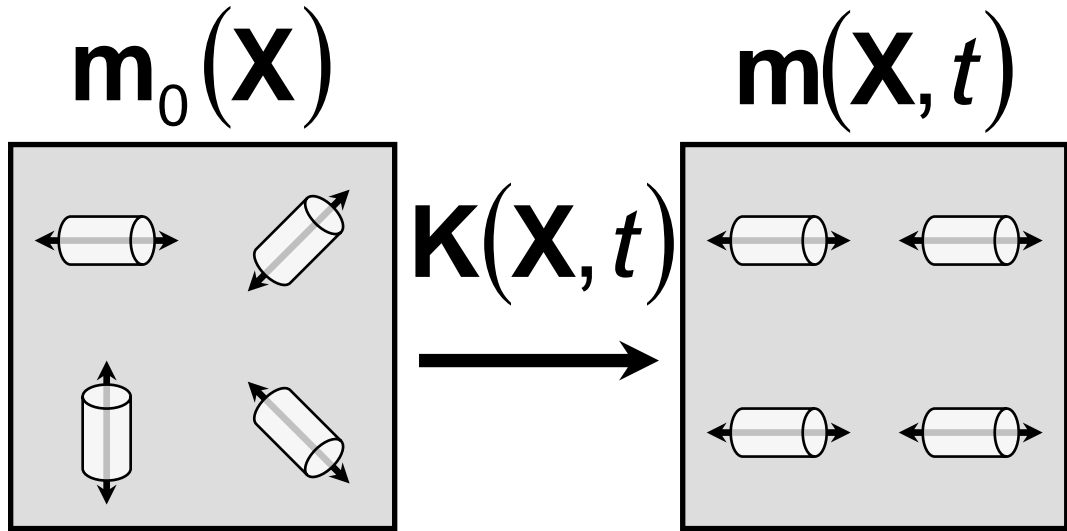
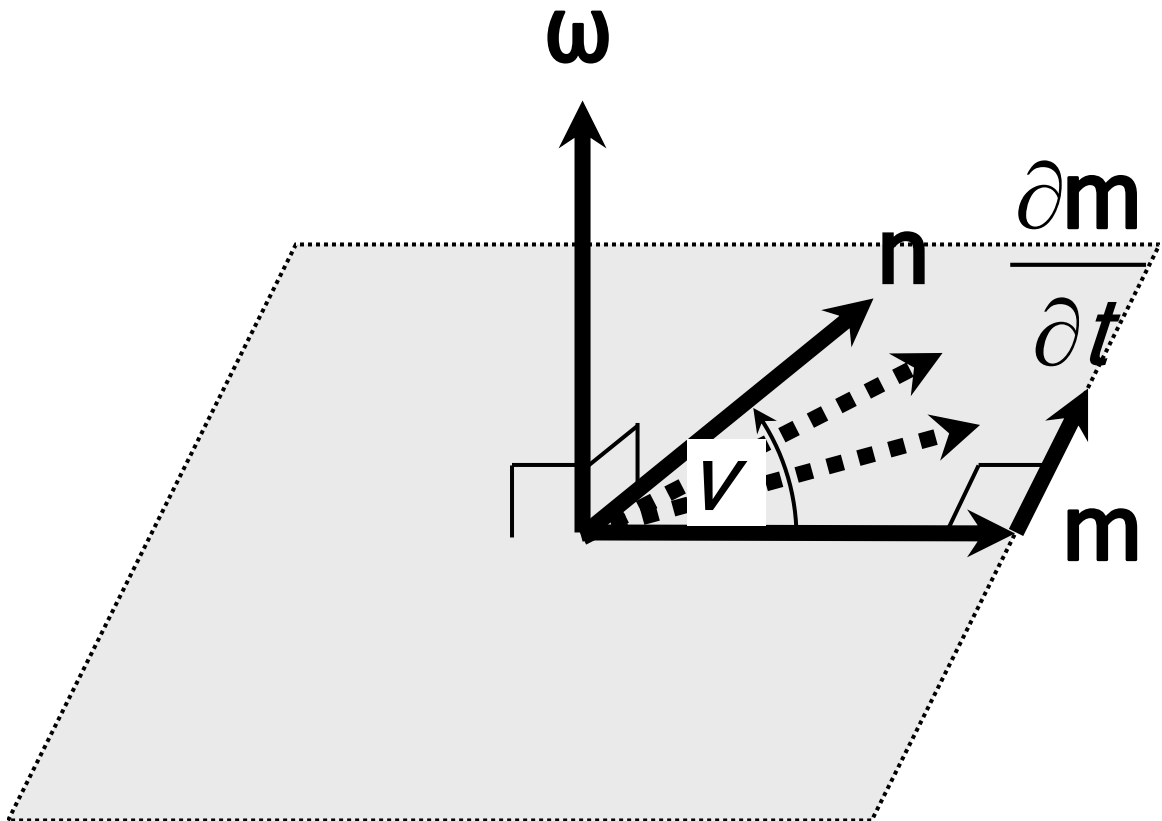Figure 2.1: Kinematics of fiber reorientation.

Figure 2.2: Evolution equation for fiber reorientation.

2.5   Maximum reorientation power

It was noted in §2.3 that a stiffening remodeling power is required to satisfy the dissipation inequality Eq. 2.13. Within the structure of Eq. 2.14 and ignoring fiber fusion, it is worthwhile to investigate not only what choices of target direction $\mathbf{n}$ satisfy the inequality but how they might enhance dissipation by maximizing the reorientation power. Importantly, the following development is independent of the particular choice of transversely-isotropic strain energy function.

Using the chain rule to open up the *reorientation* power (c.f., Eq. 2.11) yields

$$\dot{W}^{\mathrm{rot}} = \frac{1}{\hat{\lambda}} \frac{\partial W}{\partial \hat{\lambda}} \mathbf{C}\mathbf{m} \cdot \dot{\mathbf{m}}. \tag{2.17}$$

Observe that all that is required for non-negative $\dot{W}^{\mathrm{rot}}$ is a W monotonically-increasing in $\hat{\lambda}$ and an $\dot{\mathbf{m}}$ with the same sense as $\mathbf{m}$ (since $\mathbf{C} \in \mathrm{Sym}^+(3)$). Furthermore, it can be seen from the decomposition Eq. 2.15$_3$ that the angular velocity of reorientation $1/\bar{\tau}^{\mathrm{rot}}$ is rotationally-symmetric for a cone of $\mathbf{n}$ (Fig. 2.3, left) having half-angle ν (Fig. 2.2) from $\mathbf{m}$. Now working in the principal stretch space $\{\mathbf{e}_1, \mathbf{e}_2, \mathbf{e}_3\}$ of $\mathbf{C}$ with $\lambda_1^2 \geq \lambda_2^2 \geq \lambda_3^2$, this half-angle controlling angular velocity rate is chosen such that $\cos \nu = \mathbf{m} \cdot \mathbf{n} \equiv \mathbf{m} \cdot \mathbf{e}_1 \geq 0$ (i.e., according to the maximum principal stretch direction). With only this assumption on the magnitude $1/\bar{\tau}^{\mathrm{rot}}(\nu)$, the task is now to find the target vector $\mathbf{n}$ on this cone that maximizes the reorientation power through the direction $\bar{\boldsymbol{\omega}}(\mathbf{n})$. A modified reorientation power $\bar{P}^{\mathrm{rot}}$ can be defined as

$$\bar{P}^{\mathrm{rot}} \equiv \frac{\bar{\tau}^{\mathrm{rot}} \hat{\lambda}}{\partial W / \partial \hat{\lambda}} \dot{W}^{\mathrm{rot}} = \mathbf{C}\mathbf{m} \cdot \bar{\boldsymbol{\omega}}. \tag{2.18}$$

which removes the reorientation rate and strain energy contributions from $\dot{W}^{\mathrm{rot}}$. Knowing that the (instantaneous) reorientation direction must be orthogonal to the fiber direction ($\mathbf{m} \cdot \dot{\mathbf{m}} = 0$, Fig. 2.2), a local orthonormal triad $\{\bar{\mathbf{e}}_1, \bar{\mathbf{e}}_2, \bar{\mathbf{e}}_3\}$ is con-

structed with respect to the fiber direction and the stretch state (Fig. 2.3):

$$\bar{\mathbf{e}}_1 \equiv \frac{\mathbf{e}_1 - m_1\mathbf{m}}{\sqrt{1-m_1^2}}, \qquad \bar{\mathbf{e}}_2 \equiv \frac{m_3\mathbf{e}_2 - m_2\mathbf{e}_3}{\sqrt{1-m_1^2}}, \qquad \bar{\mathbf{e}}_3 \equiv \mathbf{m}, \qquad (2.19)$$

with $\mathbf{e}_1 \cdot \bar{\mathbf{e}}_1 \geq 0$. This enables the succinct expression of $\bar{\boldsymbol{\omega}}$:

$$\bar{\boldsymbol{\omega}} = (\cos\bar{\mu})\bar{\mathbf{e}}_1 + (\sin\bar{\mu})\bar{\mathbf{e}}_2 \qquad (2.20)$$

where the interpretation of $\bar{\mu}$ is given in Fig. 2.3. Plugging Eq. 2.20 into Eq. 2.18 and using the spectral decomposition $\mathbf{Cm} = \sum_i^3 \lambda_i^2 m_i \mathbf{e}_i$ yields

$$\bar{P}^{\mathrm{rot}} = \frac{\left[(\lambda_1^2 - \lambda_2^2)\, m_2^2 + (\lambda_1^2 - \lambda_3^2)\, m_3^2\right] m_1 \cos\bar{\mu} + (\lambda_2^2 - \lambda_3^2)\, m_2 m_3 \sin\bar{\mu}}{\sqrt{1-m_1^2}}. \qquad (2.21)$$

With just the single parameter $\bar{\mu}$ to vary, Eq. 2.21 is straightforwardly extremized by:

$$\bar{\mu}^{\mathrm{max}} = \arg\left(\frac{\partial \bar{P}^{\mathrm{rot}}}{\partial \bar{\mu}} = 0\right) = \arctan\left[\frac{(\lambda_2^2 - \lambda_3^2)\, m_2 m_3}{\left[(\lambda_1^2 - \lambda_2^2)\, m_2^2 + (\lambda_1^2 - \lambda_3^2)\, m_3^2\right] m_1}\right], \qquad (2.22)$$

in which *maximization* is guaranteed by consistent use of the principal stretch space basis definitions. While the specification of $\bar{\tau}^{\mathrm{rot}} \equiv \sqrt{1-m_1^2}/\tau^{\mathrm{rot}}$ for the reorientation rate confers an eventual 'relaxation' of $\mathbf{m}$ to $\mathbf{e}_1$, clearly only for the simple case of uniaxial extension ($\lambda_1 \geq \lambda_2 = \lambda_3$) does $\bar{\mu}^{\mathrm{max}} = 0$, in which $\mathbf{m}$ rotates directly toward $\mathbf{e}_1$. More generally, the dissipation-maximizing trajectory of $\mathbf{m}$ will not remain planar even for a constant stretch state. This somewhat complex result for an apparently simple model deserves further attention, as maximally-dissipative evolution equations are attractive features of mathematical formulations of inelasticity [228].

2.6 Fiber reorientation simulations

In contrast to above developments, generality is eschewed here in favor of the numerical solution of fully 3-D fiber reorientation (neglecting fusion) initial-boundary–value problems (IBVPs) representative of the attendant fibril alignment in the early-culture compaction of a collagenous engineered-tissue construct. These solutions

allowed the computation of the total reorientation power throughout an entire body under different initial fiber and boundary conditions.

A continuum-scale strain energy function incorporating the worm-like chain (WLC) model of entropic elasticity [223] was employed to simulate the mechanical response of a collagenous tissue construct:

$$W(\operatorname{tr}\mathbf{C}, J^2, \hat{\lambda}^2) = \underbrace{\frac{Nk_B\Theta L}{4A}\left[2\bar{r}^2 - \bar{r} + \frac{1}{1-\bar{r}}\right]}_{\text{entropy}}$$
$$\underbrace{- \frac{Nk_B\Theta L}{4A}\left[4\bar{r}_0^2 - \bar{r}_0 + \frac{\bar{r}_0}{(1-\bar{r}_0)^2}\right]\log\hat{\lambda}}_{\text{repulsion}}$$
$$+ \underbrace{\gamma\left[(\operatorname{tr}\mathbf{C} - 3) + \frac{1}{\beta}\left(J^{-2\beta} - 1\right)\right]}_{\text{bulk compressibility}} \tag{2.23}$$

with the WLC end-to-end and contour lengths r and L parameters (Fig. 2.4a) normalized by

$$\bar{r} = \bar{r}_0\hat{\lambda}, \qquad\qquad \bar{r} \equiv \frac{r}{L}, \qquad\qquad \bar{r}_0 \equiv \frac{r_0}{L}, \tag{2.24}$$

and other invariants defined in Eq. 2.6. This transversely-isotropic case of the eight-chain model [218] can be recovered from the orthotropic unit cell introduced in Bischoff et al. [220] by setting the dimensions $a = c$ and switching labels a and b (Fig. 2.4b). Since network effects are not likely in immature tissue, b was neglected to simplify the analysis. In-depth details and analysis of the model parameters themselves can be found in Kuhl et al. [224]. For fiber reorientation, the evolution equation Eq. 2.14 was further specialized to $\mathbf{n} \equiv \mathbf{e}_1$ so that the target vector was fully equated with the maximum principal stretch direction. The numerical implementation of the constitutive model consisting of both the linearization of the hyperelastic strain energy function and explicit integration of the fiber evolution equation was

incorporated into a custom user element subroutine for FEAP[229], a general-purpose nonlinear finite element analysis software package, for subsequent numerical solution of the nonlinear elasticity problem.

Fig. 2.5 shows a schematic of the applied conditions and kinematics of the model problem. The cylindrical geometry was lengthened uniaxially and held either under constant displacement or constant load, starting with either all transversely-oriented fibers ("uniform") or all randomly-oriented fibers ("inhomogeneous"). The axial stress responses for these cases (Fig. 2.6a) immediately show the dramatic stiffening effect of fiber reorientation. The global reorientation power

$$\mathcal{P}^{\mathrm{rmd}}(t) \equiv \int_{\Omega_0} \frac{\partial W}{\partial \mathbf{M}} : \dot{\mathbf{M}} \, dV \tag{2.25}$$

for each of these cases is plotted versus dimensionless time in Fig. 2.6b. As expected, the reorientation power production is nearly always positive, with the exception of the transversely-oriented cases, in which there is an initial interval of dissipation. This, however, is an artifact of the repulsion term of the strain energy function Eq. 2.23: Transversely-oriented fibers are initially *compressed* from the coupling of stretch and contraction in lateral directions and so pick up strain energy from the repulsion term; as they rotate axially, they lose 'repulsive' strain energy more quickly than they gain 'entropic' strain energy for a brief time, hence producing negative power. In the randomly-oriented case, most fibers are outside of this regime at any one time and the effect is not seen. Also as expected, the power production nearly vanishes after a duration of several time constants, indicating that fibers are completely aligned with the (constant) maximum principal stretch direction ($\mathbf{e}_Z$) and that reorientation has largely ceased.
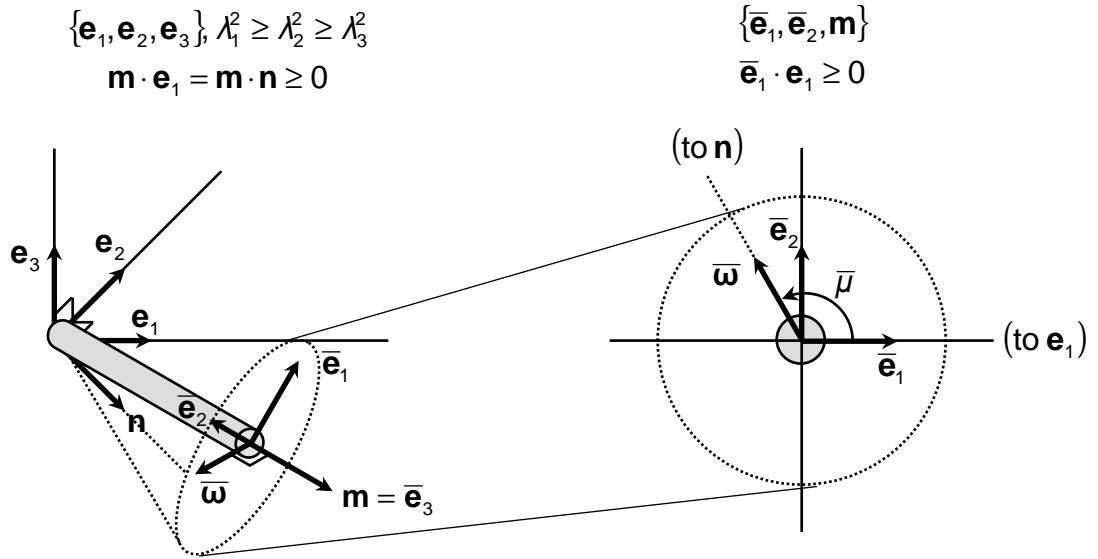
Figure 2.3: Orientation of fiber direction **m** and cone of target vectors **n** in principal stretch space and construction of rotated basis to parametrize $\bar{\boldsymbol{\omega}}$ with respect to **m**.

(a) Worm-like chain.

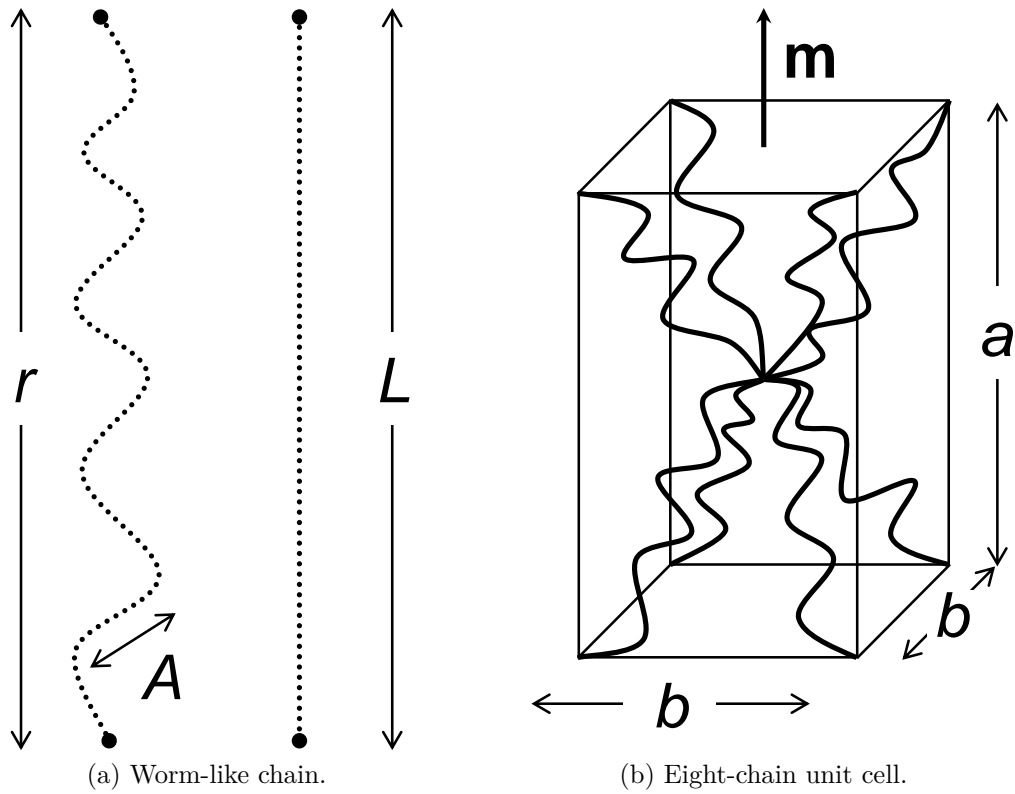(b) Eight-chain unit cell.

Figure 2.4: Transversely-isotropic worm-like chain model schematic.

2.7   Strain energy convexity

Normally, aspects of strain energy convexity are studied with respect to perturbations about the *deformation* state. Such an analysis for the transversely-isotropic strain energy function Eq. 2.23 has been carried out in Kuhl et al. [225]. Here, a preliminary investigation of the convexity of the strain energy as a function of the *fiber vector* $\bar{\mathbf{m}}$ is described.

For fiber evolution (reorientation *and* fusion), the statement of strain energy convexity can be written:

$$\Delta\bar{\mathbf{m}} \cdot \frac{\partial^2 W}{\partial\bar{\mathbf{m}}\partial\bar{\mathbf{m}}} \Delta\bar{\mathbf{m}} \geq 0 \qquad\qquad \forall\Delta\bar{\mathbf{m}} \in \Omega_0 \qquad\qquad (2.26)$$

This is not a trivial task, even for a chosen strain energy function. The approach taken here is direct: Find surfaces of constant strain energy in the space of the components of $\bar{\mathbf{m}}$, and examine for convexity. The following isochoric cases were considered:

$$\mathbf{F}^{1\text{ext}} \equiv \frac{\mathbf{I}}{\sqrt{\tilde{\lambda}}} + \left(\tilde{\lambda} - \frac{1}{\sqrt{\tilde{\lambda}}}\right)\mathbf{e}_3 \otimes \mathbf{e}_3 \qquad \text{\color{blue}uniaxial extension} \qquad (2.27\text{a})$$

$$\mathbf{F}^{2\text{ext}} \equiv \tilde{\lambda}\mathbf{I} + \left(\frac{1}{\tilde{\lambda}^2} - \tilde{\lambda}\right)\mathbf{e}_3 \otimes \mathbf{e}_3 \qquad \text{\color{blue}biaxial extension} \qquad (2.27\text{b})$$

$$\mathbf{F}^{\text{pshr}} \equiv \tilde{\lambda}\mathbf{e}_1 \otimes \mathbf{e}_1 + \frac{\mathbf{e}_2 \otimes \mathbf{e}_2}{\tilde{\lambda}} + \mathbf{e}_3 \otimes \mathbf{e}_3 \qquad \text{\color{blue}pure shear} \qquad (2.27\text{c})$$

$$\mathbf{F}^{\text{sshr}} \equiv \mathbf{I} + \tilde{\lambda}\mathbf{e}_1 \otimes \mathbf{e}_2 \qquad \text{\color{blue}simple shear} \qquad (2.27\text{d})$$

where $\mathbf{F}$ is the deformation gradient, $\mathbf{I}$ is the identity tensor, $\tilde{\lambda}$ is the applied stretch parameter, and $\{\mathbf{e}_1, \mathbf{e}_2, \mathbf{e}_3\}$ is a Cartesian basis. Associated 'iso-energy' surfaces for the strain energy function Eq. 2.23 are plotted in Fig. 2.7. Additionally, the surfaces are shaded according to the fiber stretch $\hat{\lambda}$ defined in Eq. 2.24 (the applied stretch projected onto the fiber). In all cases except for biaxial extension do the surfaces appear to be convex. Note that the failure of convexity occurs where the fiber stretch

is highly compressive ($\hat{\lambda} \ll 1$). This non-convexity corresponds to the phenomenon seen with the negative reorientation power in Fig. 2.6b and is thus likely an artifact of the repulsive term in Eq. 2.23. This feature further motivates a more careful treatment of such offset terms in anisotropic continuum strain energy functions built from micromechanical models.

2.8 Conclusion

Some of the thermodynamic aspects of generic, transversely-isotropic internal variable models of biological remodeling have been investigated. These findings, described in terms of dissipation and convexity, provide a basis for refinement and enhancement of these constitutive models. The key result that, without a source of energy, a *stiffening* remodeling law necessarily violates the dissipation inequality directly motivates the explicit incorporation of active cell processes into the remodeling evolution equations. A potential remedy to this quandary is in fact given by the example of the anisotropic biphasic theory of Barocas and Tranquillo [219]. Having been developed specifically to model the various mechanical phenomena associated with the compaction of a fibroblast-populated biopolymer gel, they incorporated equations governing cell density, alignment, migration, mitosis, and traction into a simplified continuum mechanical, biphasic mixture model. Ongoing work in our group takes a similar approach but accounts for the detailed anisotropic mechanics of the cytoskeleton with eventual incorporation into our tissue-level mixture model [227].
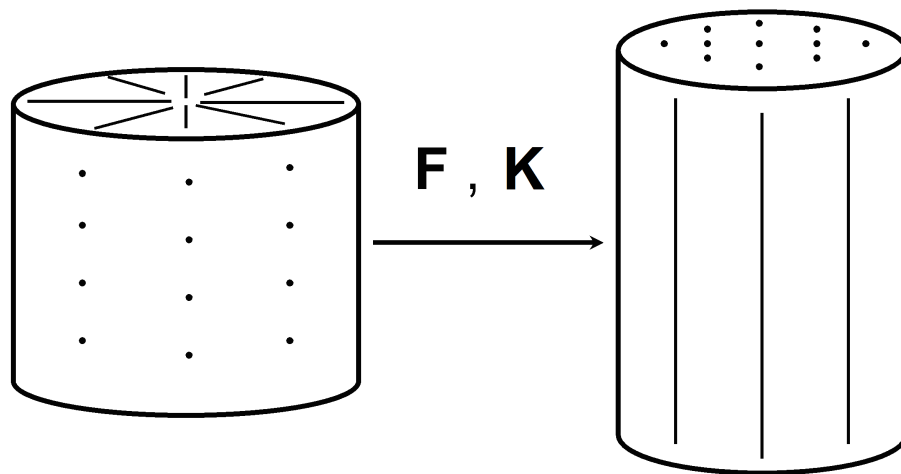
Figure 2.5: Schematic of uniaxial fiber reorientation under (ex)tension.
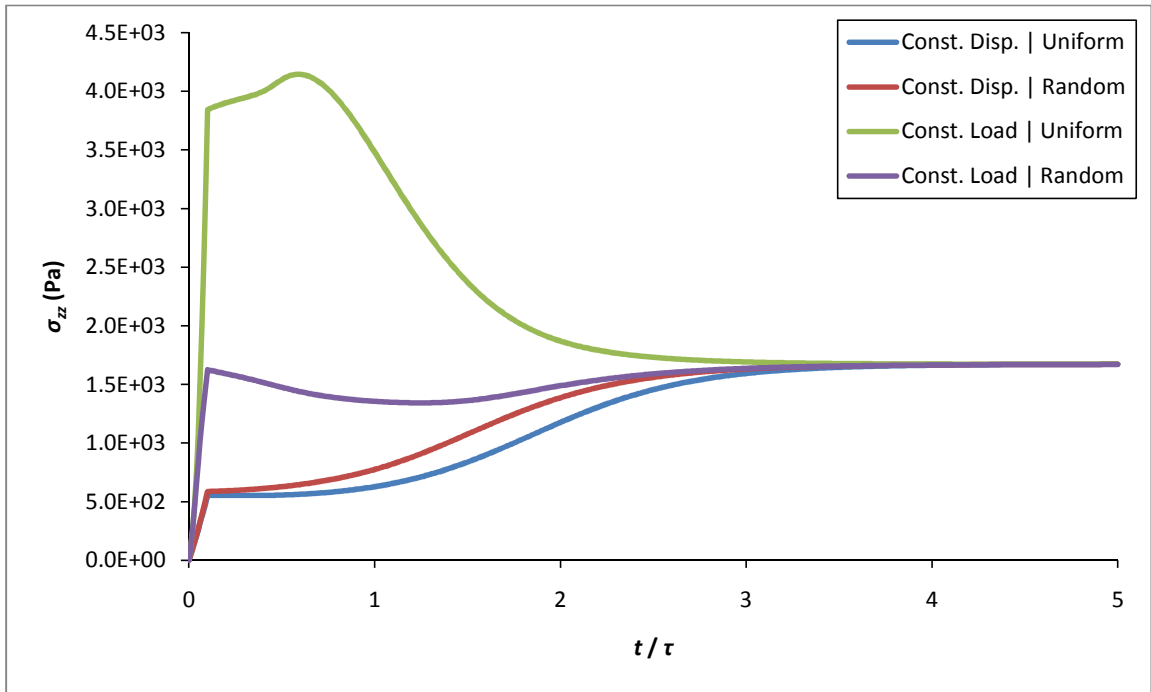
(a) Axial Cauchy stress.
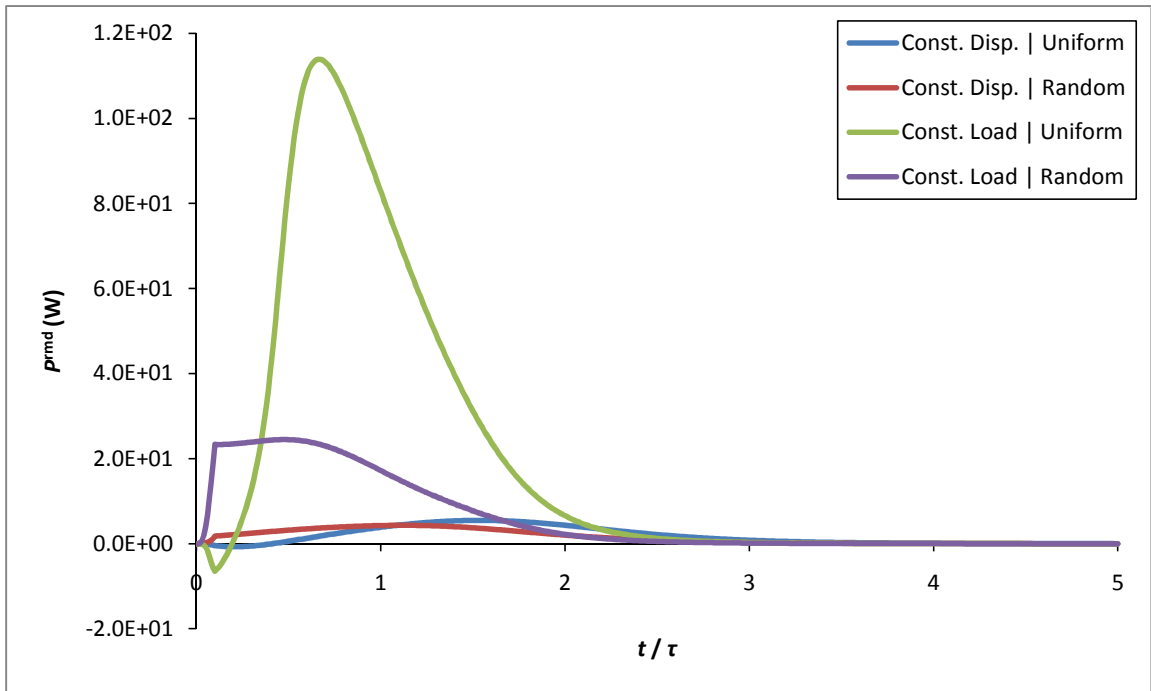
(b) Global reorientation power.

Figure 2.6: Time-dependent responses under reorientation for each IBVP.

(a) Uniaxial extension.

(b) Biaxial extension.

(c) Pure shear.

(d) Simple shear.
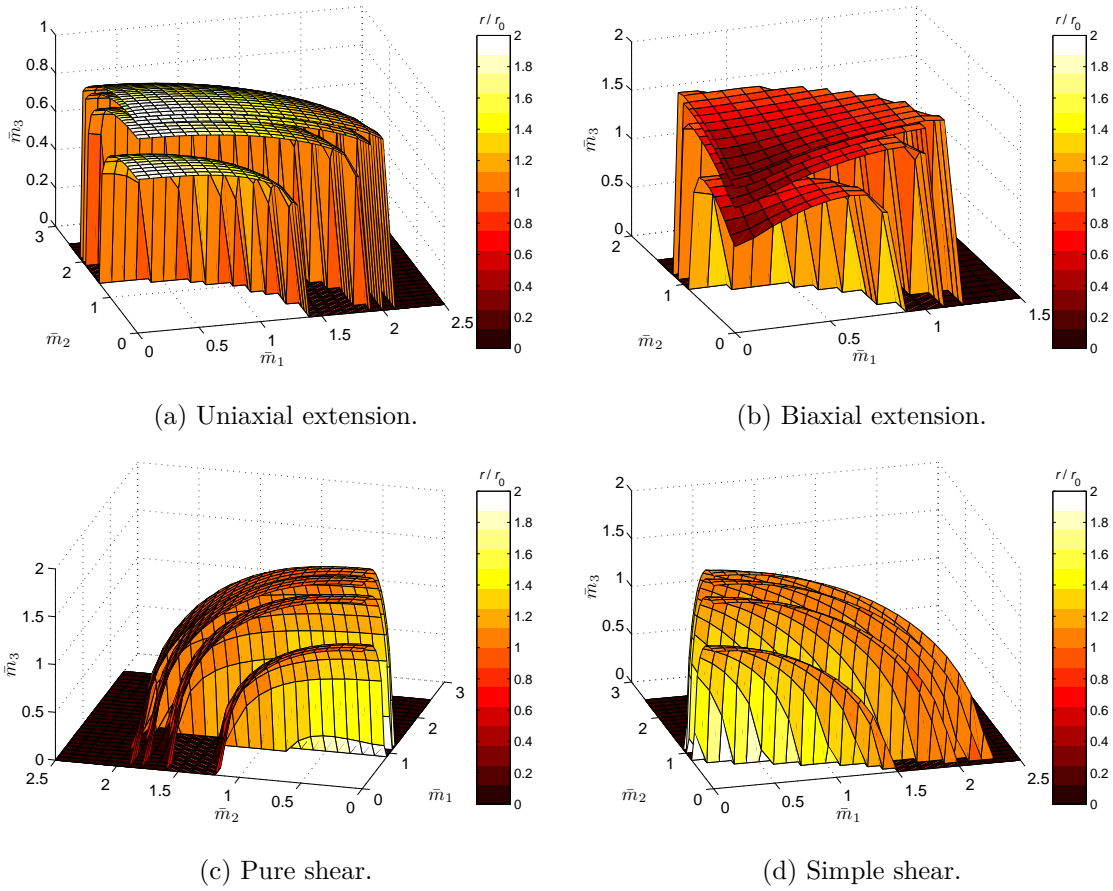
Figure 2.7: Iso-energy surfaces in the space of the fiber vector $\bar{\mathbf{m}}$ for canonical strain states.

BIBLIOGRAPHY

[218] E. M. Arruda and M. C. Boyce. A 3-dimensional constitutive model for the large stretch behavior of rubber elastic-materials. *Journal of the Mechanics and Physics of Solids*, 41(2):389–412, Feb 1993. 61

[219] V. H. Barocas and R. T. Tranquillo. An anisotropic biphasic theory of tissue-equivalent mechanics: The interplay among cell traction, fibrillar network deformation, fibril alignment, and cell contact guidance. *Journal of Biomechanical Engineering-Transactions of the ASME*, 119(2):137–145, 1997. 53, 65

[220] J. E. Bischoff, E. A. Arruda, and K. Grosh. A microstructurally based orthotropic hyperelastic constitutive law. *Journal of Applied Mechanics-Transactions of the ASME*, 69(5):570–579, 2002. 61

[221] N. J. B. Driessen, G. W. M. Peters, J. M. Huyghe, C. V. C. Bouten, and F. P. T. Baaijens. Remodelling of continuously distributed collagen fibres in soft connective tissues. *Journal of Biomechanics*, 36(8):1151–1158, 2003. 53

[222] K. Garikipati, J. E. Olberding, H. Narayanan, E. M. Arruda, K. Grosh, and S. Calve. Biological remodelling: Stationary energy, configuration change, internal variables and dissipation. *Journal of the Mechanics and Physics of Solids*, 54(7):1493–1515, Jul 2006. 54

[223] O. Kratky and G. Porod. Rontgenuntersuchung geloster fadenmolekule. *Recueil Des Travaux Chimiques Des Pays-Bas-Journal of the Royal Netherlands Chemical Society*, 68(12):1106–1122, 1949. 61

[224] E. Kuhl, K. Garikipati, E. M. Arruda, and K. Grosh. Remodeling of biological tissue: Mechanically induced reorientation of a transversely isotropic chain network. *Journal of the Mechanics and Physics of Solids*, 53(7):1552–1573, 2005. 53, 57, 61

[225] E. Kuhl, A. Menzel, and K. Garikipati. On the convexity of transversely isotropic chain network models. *Philosophical Magazine*, 86(21-22):3241–3258, Jul-Aug 2006. 64

[226] A. Menzel. Modelling of anisotropic growth in biological tissues - a new approach and computational aspects. *Biomechanics and Modeling in Mechanobiology*, 3(3):147–171, Mar 2005. 53, 57

[227] H. Narayanan, E. M. Arruda, K. Grosh, and K. Garikipati. The micromechanics of fluid-solid interactions during growth in porous soft biological tissue. *Biomechanics and Modeling in Mechanobiology*, 8(3):167–181, Jun 2009. doi: {10.1007/s10237-008-0126-1}. 65

[228] J. C. Simo and T. J. R. Hughes. *Computational Inelasticity*. Springer, New York, 1998. 60

[229] R.L. Taylor. *FEAP—a Finite Element Analysis Program*. University of California, Berkeley, Berkeley, CA, 7.5 edition, March 2005. 62

CHAPTER 3

Image analysis methods for fiber direction quantification in planar and volumetric data

3.1 Introduction

Development of tissue-specific mechanical anisotropy is crucial to effective and efficient function of connective soft tissue. This is especially important in the contexts of tissue engineering and wound repair in which it has been a major challenge to induce and/or guide the development of proper anisotropy. Any experimental and theoretical investigation of soft tissue mechanics thus benefits from quantification of the microstructual anisotropy from which the macroscopic function emerges. This requires both an appropriate microscopy or spectroscopy method and, frequently, image analysis techniques to process and apply the data. Here, the three-dimensional adaptation and extension of existing approaches for assessing global texture orientation and anisotropy via gradients of image intensity in a statistical and (possibly) spatially-dependent fashion for incorporation into transversely-isotropic strain energy functions is described. While it is hoped that the development is sufficiently general for a range of similar tissue morphologies and imaging modalities, the thrust is toward quantifying the evolution of fibril [1] -based anisotropy in fibroblast-populated collagen gels using confocal laser scanning microscopy. To this end, a two-dimensional valida-

---
[1]Though each have distinct definitions in tissue histology, the term *fibril* should be taken to mean the actual microstructural constituent, while *fiber* may be used to generically refer to any such linear structural element, including the idealized representation of a *fibril*.

tion of the proposed method's performance is demonstrated using realistic synthetic test images of known fiber distributions, and a preliminary application to three-dimensional image volumes of an isotropic and an aligned collagen gel is presented.

3.2 Formulation and algorithm

A grayscale intensity image I is represented by the scalar field $i(\mathbf{x}) \in [0, 1]$, $\mathbf{x} \in \mathbb{R}^n$, where n is the number of space dimensions. Simply stated, the problem is to obtain a weighted-average edge orientation in each local "sub-image" $S \subset I$. The gradient $\nabla i \equiv \partial i / \partial \mathbf{x}$ produces a vector field containing pointwise edge *normal* directions. Since an image is, in general, a discrete, discontinuous field, it must be smoothed (blurred) with a low-pass filter prior to numerical differentiation. In the spatial domain, image filtering is accomplished via the convolution of a filter kernel $k(\mathbf{x})$ with the intensity image $i(\mathbf{x})$ and denoted by $k * i$. Making use of the differentiation property of convolution, the approximate gradient field $\mathbf{g}(\mathbf{x})$ can thus be calculated:

$$\nabla i(\mathbf{x}) \approx \mathbf{g}(\mathbf{x}) \equiv \nabla\left(k(\mathbf{x}) * i(\mathbf{x})\right) = \nabla k(\mathbf{x}) * i(\mathbf{x}). \qquad \frac{d}{dx}(f(x) * g(x)) = \frac{df}{dx} * g(x) \qquad (3.1)$$

In this way, the gradient operation is embedded inside of the (continuous) kernel function in closed form and applied to the (discontinuous) intensity field $i(\mathbf{x})$, thus avoiding explicit numerical differentiation. Due to its monotonic frequency response, a normalized Gaussian filter is employed to smooth the image:

$$k(\mathbf{x}; \sigma) = \frac{1}{(2\pi)^{n/2}\sigma^n} \exp\left[-\frac{\|\mathbf{x}\|^2}{2\sigma^2}\right], \qquad (3.2)$$

which, when applied to Eq. 3.1, $\nabla k(\mathbf{x})$ is known as the *gradient-of-Gaussian* filter. This procedure is illustrated in Fig. 3.1, in which vertical and horizontal edge images $g_x(\mathbf{x})$ and $g_y(\mathbf{x})$ are extracted from $i(\mathbf{x})$.

Next, the directional information held in $\mathbf{g}(\mathbf{x})$ is accumulated in a *weighted histogram* of edge directions. This requires a *window* function to "bin" the gradient magnitudes according to the corresponding gradient direction. For this task, directional probability density functions (PDFs) $p : \mathbb{S}^{n-1} \mapsto \mathbb{R}^+$ are convenient[233]:

$$n = 2, \qquad p_{VM}(\boldsymbol{\xi}; \boldsymbol{\mu}, \kappa) = \frac{\exp\left[2\kappa\left(\boldsymbol{\mu} \cdot \boldsymbol{\xi}\right)^2\right]}{c(\kappa)\exp\kappa}; \qquad (3.3)$$

$$n = 3, \qquad p_W(\boldsymbol{\xi}; \boldsymbol{\mu}, \kappa) = \frac{\exp\left[\kappa(\boldsymbol{\mu} \cdot \boldsymbol{\xi})^2\right]}{c(\kappa)}; \qquad (3.4)$$

representing the (doubly-wrapped) *von Mises* and *Watson* [235] distributions on the unit circle ($\mathbb{S}^1$) and sphere ($\mathbb{S}^2$), respectively (Fig. 3.2). Here, $\boldsymbol{\mu} \in \mathbb{S}^{n-1}$ and κ are the *mean direction* and *concentration parameters*; $c(\kappa)$ is a normalization constant so that $p(\boldsymbol{\xi})$ integrates to unity, as required. Note that these PDFs are *antipodally-symmetric* since fiber direction, in a mechanical context, is only unique up to a half-space. The expression for the weighted histogram $\bar{h}^S(\boldsymbol{\xi})$ for the sub-image S incorporating the appropriate window function $w(\boldsymbol{\xi}) \leftarrow p(\boldsymbol{\xi})$ is then given as:

$$\bar{h}^S(\xi) = \frac{1}{c^S}\int_S \|\mathbf{g}(\mathbf{x})\|\, w\left(\frac{\mathbf{g}(\mathbf{x})}{\|\mathbf{g}(\mathbf{x})\|}; \boldsymbol{\xi}, -\kappa\right)\, dV, \qquad \int_{\mathbb{S}^{n-1}} \bar{h}^S(\xi)\, dA = 1. \qquad (3.5)$$

In contrast to Eq. 3.3 and Eq. 3.4, it is critical to note the sign on the concentration κ. The gradient vector field $\mathbf{g}(\mathbf{x})$ describes edge *normals*. Fiber directions correspond to edge *tangents*. In the 2-D case, the normal direction corresponds to a unique tangent line (direction, up to a half-space). For $n = 3$, however, the normal direction identifies a tangent *plane*. By windowing with the inverse ($p^{-1}(\boldsymbol{\xi})$, "girdle"-regime of the bimodal symmetric PDF, the tangent directions are accumulated instead of the normal directions. This particular strategy underlies the principal transverse isotropy assumption. Note that $VM(\xi, -\kappa) = VM(\xi + \pi/2, \kappa)$. With such a distribution model, the window function possesses the attractive property that sign reversal on

the concentration parameter is tantamount to rotating the mean direction by $\pi/2\,\mathrm{rad}$ from normal to tangent, and provides a general *inversion* framework for window functions in 2D and 3D.

So, in words, Eq. 3.5$_1$ (approximately) amounts to interrogating each pixel for its gradient direction, then incrementing the *tangential* angle bins in $\bar{h}^S(\xi)$ by the corresponding gradient magnitude. The inclusion of the non-uniform distribution in the window functions can be interpreted as accounting for the uncertainty κ associated with a single orientation measurement. To standardize the procedure, the concentration κ of the window function is chosen here such that the function decays to *half* its maximum value at the edges of the discrete histogram bins; i.e., the radius of $w(\xi)$ at half maximum is $\Delta\xi/2$:

$$\kappa = \arg\left[\frac{w_W(\xi + \Delta\xi/2; \mu, \kappa)}{w_W(\xi; \mu, \kappa)} = \frac{1}{2}\right] = \frac{\log 2}{1 - \cos\Delta\xi} \tag{3.6}$$

A similar criterion is applied for the spherical window functions, but an additional complication arises in 3-D with respect to solid angle bin mesh generation: A uniform point density is not straightforwardly obtained on the sphere by closed-form expressions on the polar and azimuthal spherical coordinates. Instead, the robust mesh generator DistMesh©[234] is employed with triangular elements to produce an approximately uniform tessellation of the sphere.

The entire formulation was implemented in MATLAB®(Version 7.2.0.283, The MathWorks, Inc., Natick, MA) with the Image Processing Toolbox.

3.3 Validation

To evaluate and validate the performance of the method, synthetic test images featuring "fibers" of known orientation distributions were generated and analyzed. Due to the quantity of artificial images required to test the range of possible fiber

$$\mathbf{g}(\mathbf{x}) \quad = \quad \frac{\partial}{\partial \mathbf{x}} \boxed{k} \quad * \quad \boxed{I} \quad = \quad \boxed{Gx}\,\mathbf{e}_x \quad + \quad \boxed{Gy}\,\mathbf{e}_y$$

Figure 3.1: Visual representation of spatial gradient-of-Gaussian filter applied to fiber image I.
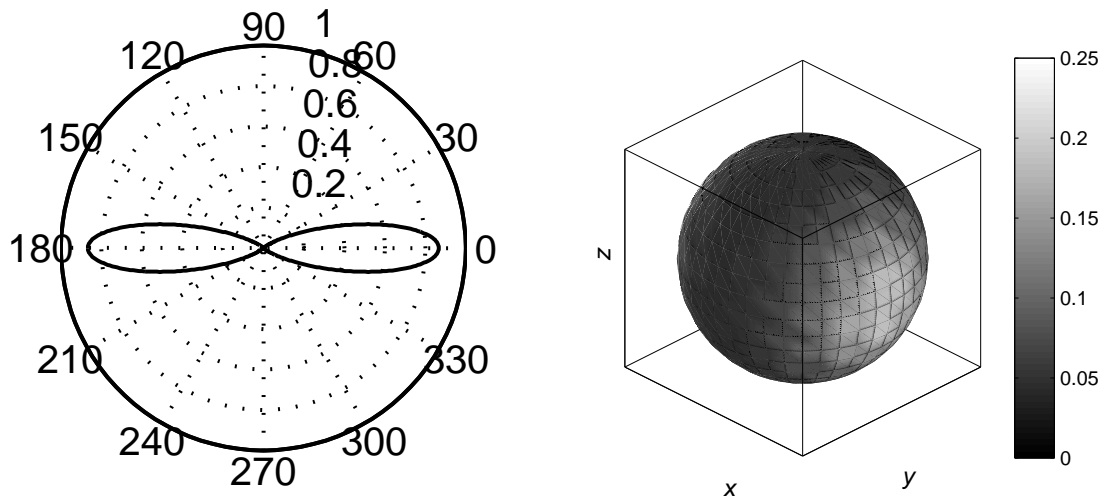
(a) Circular von Mises PDF.

(b) Spherical Watson PDF.

Figure 3.2: Directional PDFs for weighted histogram window functions.

properties, two dimensionality was maintained for method validation. The density (overlap), length, diameter, and alignment properties were varied. Fig. 3.3 shows a representative group of synthetic images and the corresponding analysis. Fibers with pixel dimensions of $D = 2\,\mathrm{px}$ diameters and $L = 100\,\mathrm{px}$ lengths are shown here, typical of collagen fibrils viewed under a confocal microscope. Each image was analyzed individually without subdivision. A Gaussian filter radius of $1\,\mathrm{px}$ was used. This value was chosen as to optimize performance and minimize error over a range of fiber alignment directions and strengths for the given fiber geometry. The excellent agreement in Fig. 3.3 provides $\sigma \approx D$ as a general analysis guideline.

3.4   Application to collagen gels

As indicated, the fibrillar alignment resulting from a fibroblast-compacted, mechanically-constrained collagen gel imaged using reflection-mode confocal microscopy was chosen as a convenient "anisotropic" specimen for the image analysis procedure. An acellular but otherwise identical gel served as an "isotropic" control specimen. Briefly, solubilized collagen (Collagen Type I; Rat Tail, #354236, BD Biosciences, Bedford, MA) was reconstituted according to the manufacturer's neutral-start procedure to a final collagen concentration of $2\,\mathrm{mg}/\mathrm{mL}$. For cellular gels, a TFB solution (prepared as per §4.2.3) was added prior to polymerization to $1\mathrm{e}6\,\mathrm{cell}/\mathrm{mL}$. The mixtures were gelled under $37\,°\mathrm{C}$ incubation in glass micro-well dishes (#P35G-1.5-14-C, MatTek Corp., Ashland, MA) fitted with a $5 \times 2 \times 8\,\mathrm{mm}$ rectangular bar mold with hydrophilized porous polyethylene (PE) ends to allow lateral contraction but constrain motion in the axial direction. Following $12\,\mathrm{h}$ in culture, image stacks were acquired from the gel mid-substances with an inverted confocal laser scanning microscope in reflection mode ($488\,\mathrm{nm}$ laser light, $480\,\mathrm{nm}$–$500\,\mathrm{nm}$ detection filter; $100\times$, $1.4\,\mathrm{NA}$ oil immersion

(a) $VM(0,0)$ (b) $VM(0,1.7)$ (c) $VM(0,3)$
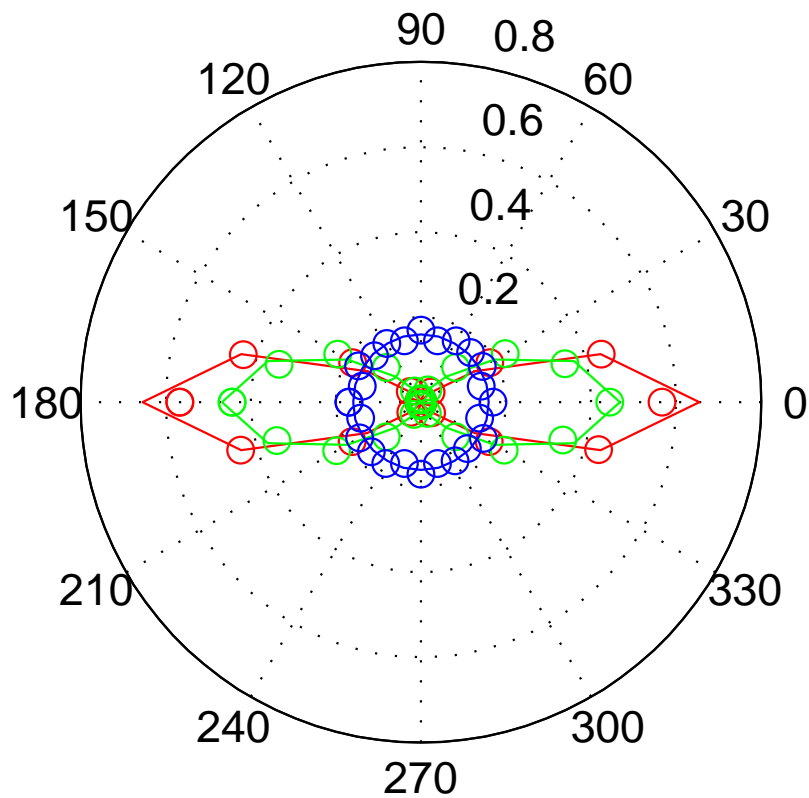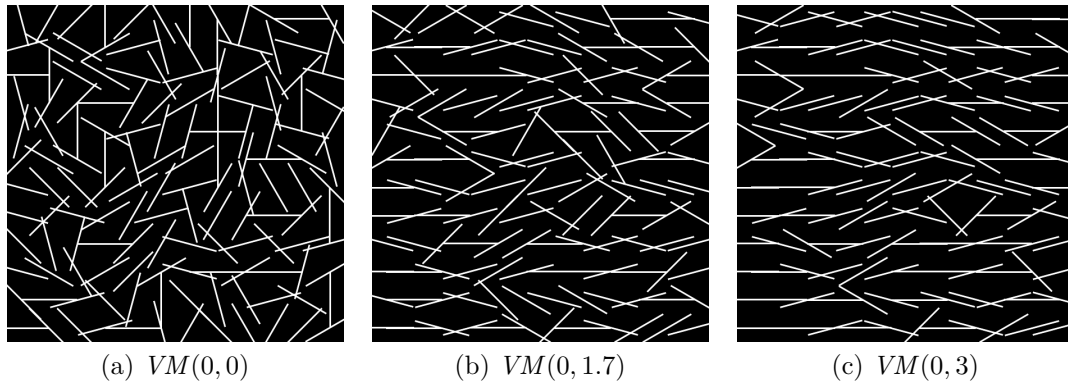
(d) Curve fits.

Figure 3.3: 2-D validation of spatial gradient-based filter-window technique. Test images were generated with "fibers" having $2\,\mathrm{px}$ diameters, $100\,\mathrm{px}$ lengths, and orientation distributions as labeled at discrete orientations each $\Delta\xi = \pi/12$. Here, image analysis parameters were fixed at $\sigma = 1\,\mathrm{px}$ (fiber radius) with window concentration $\kappa \approx 20$, determined by Eq. 3.6. Solid curves are the distributions used to generate images; open circles represent weighted histograms recovered by the analysis.

objective; Leica TCS SP2, Leica Microsystems, Wetzlar, Germany). Representative images at $z = 5\,\mu\mathrm{m}$ with a $150\,\mu\mathrm{m} \times 150\,\mu\mathrm{m}$ field of view are shown in Fig. 3.4a and Fig. 3.4b. Consistent with the macroscopic appearance of the gels (figure insets) the cell-populated gel shows a denser, more-aligned microstructure from compaction and remodeling. The fully 3-D image analysis on the $z = 1\,\mu\mathrm{m}$–$20\,\mu\mathrm{m}$ confirms these observations quantitatively, shown here via edge histogram contour plots (Fig. 3.4c, Fig. 3.4d), and thus demonstrates a practical application of the formulation.

3.5 Strain-energy representation

To tie mechanics back in, two strategies for strain-energy representation of analysis results are summarized. Upon a typical anisotropic additive split of the strain energy function $W = W^{\mathrm{iso}} + W^{\mathrm{ani}}$, the anisotropic term may, in general, be modeled in an *integral-based* form[232]:

$$W^{\mathrm{ani}} = \int_{\mathbb{S}^{n-1}} W^{\mathrm{fib}}\left(\bar{\lambda}^2\right) \bar{h}(\boldsymbol{\xi})\ dA, \qquad \bar{\lambda}^2 = \boldsymbol{\xi} \cdot \mathbf{C}\boldsymbol{\xi}; \qquad (3.7)$$

or in a *moment-based* fashion[231]:

$$W^{\mathrm{ani}} = l W^{\mathrm{fib}}\left(\bar{\lambda}^2\right), \qquad \bar{\lambda}^2 = \bar{\mathbf{m}} \cdot \mathbf{C}\bar{\mathbf{m}}, \quad l\mathbf{m} \equiv \mathrm{E}[\boldsymbol{\xi}] = \int_{\mathbb{S}^{n-1}} \boldsymbol{\xi}\bar{h}(\boldsymbol{\xi})\ dA; \qquad (3.8)$$

where W^{fib} is the fiber strain energy function and $\mathrm{E}[\boldsymbol{\xi}]$ is the *expected value* of the distribution described by density $\bar{h}$. Not surprisingly, the former expression is more valid for more general strain states, while the latter is clearly more computationally-efficient. An analysis of the ranges of validity for these methods to incorporate orientation distribution data into strain energy functions is reported in Bischoff [230], including conditions under which Eq. 3.7 and Eq. 3.8 can be made equivalent.
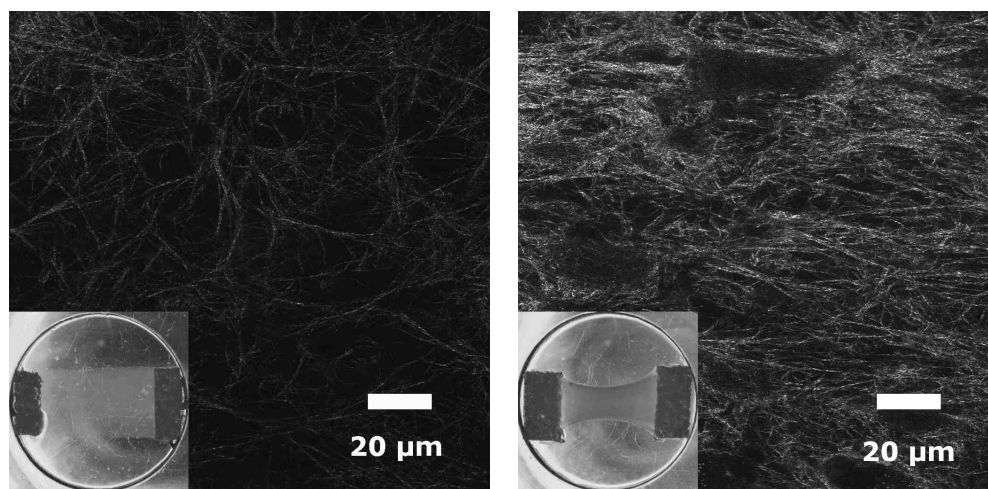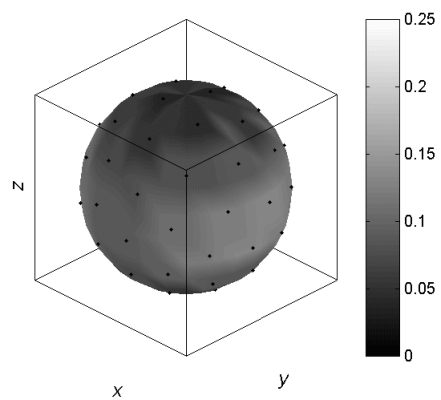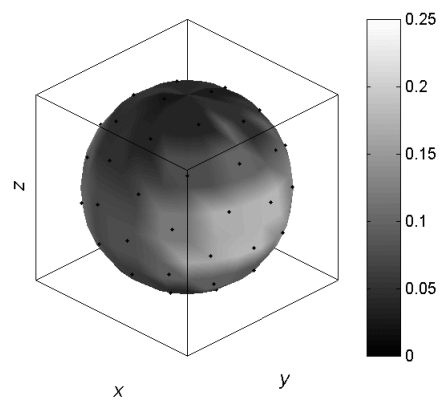
Figure 3.4: **3.4a** Acellular ("isotropic") and **3.4b** compacted ("anisotropic") collagen gels viewed via reflection-mode confocal microscopy with **3.4c**–**3.4d** corresponding directional volumetric image analysis.

3.6 Conclusion

Fully-automated, high-throughput image processing techniques and software were developed for the detailed quantification of anisotropy in 2-D and 3-D data. The presented method does not identify discrete features in the data, so it cannot directly identify cross-links or network properties in specimen microstructure. It is, however, scaleable to the requirements of a particular problem by tuning the spatial parameter σ and the size of the sub-image S. The former is the full width at half maximum of the Gaussian low-pass filter, so, as indicated above, it should be selected on the order of the fiber diameter to appropriately smooth noise in the data, yet not too large as to "blend" adjacent fibers' intensities together. Since each sub-image S generates its own angular histogram, its size should be chosen according to the spatial resolution or "locality' required by the analysis. Thus, there is a trade-off: larger subimages ensure a smoother histogram and better statistics due to more pixel (voxel) data points, but the localization of any alignment apparent in the histogram can be determined only up to the subimage location. Conversely, smaller subimages will give direction and strength of alignment at more points in the image, but each have more uncertainty. For example, if one were interested in fiber orientation patterns around a cell ($\sim 25\,\mu$m), S should be of the same size scale. At the "tissue" level, in line with the preceding example and the objectives of this project, microscopy images with a field of view $\sim 100\,\mu$m retain a very local picture when compared with a specimen size ($\sim 10\,$mm) such that image sub-division no longer makes sense. However, precise rules for the appropriate usage of these parameters for continuously fibrillar image content do not exist and remains an open issue.

BIBLIOGRAPHY

[230] J. E. Bischoff. Continuous versus discrete (invariant) representations of fibrous structure for modeling non-linear anisotropic soft tissue behavior. *International Journal of Non-Linear Mechanics*, 41(2):167–179, 2006. 78

[231] J. E. Bischoff, E. A. Arruda, and K. Grosh. A microstructurally based orthotropic hyperelastic constitutive law. *Journal of Applied Mechanics-Transactions of the ASME*, 69(5):570–579, 2002. 78

[232] Y. Lanir. Constitutive-equations for fibrous connective tissues. *Journal of Biomechanics*, 16(1):1–12, 1983. 78

[233] Kanti V. Mardia, Peter E. Jupp, and Anonymous. *Directional Statistics*, volume 2nd. Wiley, Chichester, 2000. ISBN 0-471-95333-4. 73

[234] P. O. Persson and G. Strang. A simple mesh generator in MATLAB. *SIAM Review*, 46(2):329–345, June 2004. 74

[235] G. S. Watson. Equatorial distributions on a sphere. *Biometrika*, 52:193–201, 1965. 73

Effect of oxygen tension on the two-dimensional monolayer culture fibrogenesis of bone marrow stromal cells

4.1 Introduction

Various *in vitro*, scaffold-less, 3-D, engineered tissue contructs (ETCs) fabricated in our laboratory from self-assembling 2-D cultures of rat bone marrow stromal cells (MSCs) [256, 265, 266] (MSCs), but the system is not yet optimized specifically for *in vitro* fibrogenesis, that is, the development of parallel-fibered, collagenous soft tissue like tendon and ligament.

The efficacy of a cell-based therapy for regenerative medicine, like tissue engineering (TE), relies at least in part on the ability of cells to populate a graft as quickly as possible [252] prior to differentiation and function. While massive proliferative potential is a unique feature of normal stem cells (§1.2.1), this does not always correspond to those with the greatest *growth rate*. Knowledge of growth rates is also critical in order to standardize cell culture practices such as passage frequency and dilution ratios. In our scaffold-less engineered construct system, the growth rate is relevant at a variety of plating densities, depending on whether it is the expansion phase or ETC-formation stage.

In order to produce a MSC-based soft ETC, it behooves the tissue engineer to identify those conditions which enrich for the fibroblastic phenotype for a tendinous or ligamentous tissue. collagen I (Col1) is the dominant structural protein in the

tendon and ligament extracellular matrix (ECM) (and the body) and is the most important determinant of the tissue's stiffness and strength. With Col1, elastin (Eln) is the elastic structural protein of the body and is also abundant in the parallel-fibered tissues. While no accepted unique marker for fibroblasts exists, the transcription factor scleraxis (Scx) is strongly associated with limb tendons and ligaments [263], and is required for proper embryonic limb tendon development [258]. Its role in the adult is unknown, however, its upregulation in the context of a stem-like cell such as MSCs may indicate an early *in vitro* preference toward tendon and ligament §1.2.1.

A cell culture parameter that has raised particular interest in the stem cell and tissue engineering communities recently is that of incubator oxygen tension. Most cell and tissue culture oxygen fractions (ϕ_{O_2}) are maintained near atmospheric levels ($\sim 18\%$), yet mean *in vivo* concentrations are likely 3% or lower [245, 251]. This is especially plausible in the avascular tendon and ligament tissues of the body. Moreover, the ϕ_{O_2} level is known to have exquisite effects on stem cell proliferation [242], senescence [259], apoptosis [241], differentiation [247], and migration [250] in other cell types [240], but has not been fully characterized in the multipotent MSC fraction.

The objectives of the present studies were to assess the pure fibrogenesis (fibroblastic growth and differentiation) in monolayer culture of MSCs in *differential* ϕ_{O_2} *culture*: 18% *normoxic* gaseous ϕ_{O_2} content versus 5% *hypoxia*[1], with cohort tendon fibroblasts (TFbs) as comparison given the lack of a true positive control. These levels were chosen to lie between 1%–7%, the normal values reported to be found in the bone marrow compartment [245, 251] and provide a standard cell culture control (5% CO_2-18% O_2). Given that our ETC spend at most a week in 2-D proliferation in high-serum growth medium and that immunocytochemistry does not provide the

---

[1]The conventions *normoxia* and *hypoxia* are to be understood here with respect to cell culture standards rather than physiological approximations.

quantitative sensitivity required for the heterogeneous MSC population, these aims were addressed via the cellular and molecular biological metrics of cell growth and fibroblastic gene expression and Col1 protein content for up to 8 d in culture. It was hypothesized that hypoxic conditions would support greater MSC fibrogenesis relative to normoxia due to the more physiological, *in vivo*-like environs it confers.

4.2 Materials and Methods

4.2.1 Culture media and solutions

Sterile, endotoxin and pyrogen-free media, salt solutions, and plasticware were used in all tissue acquisition and cell culture.

Transfer medium

During animal dissection and for transport prior to tissue digestion and cell isolation, tissue samples were temporarily stored in 4 °C transfer medium (TM) consisting of Dulbecco's phosphate-buffered saline (DPBS) (calcium and magnesium-free; GIBCO®, #14190, Invitrogen, Grand Island, NY) and 2× antibiotic-antimycotic (AbAm) (GIBCO™, #15240, Invitrogen).

Tissue digestion solution

To disassociate the collagenous extracellular matrix of Achilles tendons to release fibroblasts for primary culture, a digestion solution of high-glucose Dulbecco's modified Eagle medium (DMEM) (GIBCO®, #10569, Invitrogen), $500\,^{\mathrm{U}}/_{\mathrm{mL}}$ type II collagenase (GIBCO™, #17101, Invitrogen), and 2× AbAm was used, all sterilized by 0.22 µm filter (Steriflip®, #SCGP00525, Millipore, Billerica, MA).

Growth media

For routine cell expansion and subculture, TFbs will be provided a growth medium (GM) of DMEM, 20 % qualified fetal bovine serum (FBS) (GIBCO™, #10437, Invitrogen), and 1× AbAm. MSCs were raised on $\mathrm{GM_{msc}}$ composed of GM supplemented with 6 ng/mL mammal-derived recombinant human basic fibroblast growth factor (bFGF; #100-18B, PeproTech, Rocky Hill, NJ) as a mitogen.

4.2.2 Tissue digestion and cell isolation

All tissue samples for primary cell culture were obtained from two-month-old, female, non-pregnant Fischer (F344) rats.

Bone marrow stromal cells

The following procedure largely follows that of Lennon and Caplan [253] with some modifications. Legs were separated from rats post-mortem and placed in TM at 4 °C until ready for use. Samples were then rinsed in DPBS, removed of feet, split at the knee, and cleaned of remaining muscle and connective tissue. The ends of each femur and tibia were removed; then, with an 18-gauge hypodermic needle (#305196, Becton Dickinson, Franklin Lakes, NJ) and 10 mL syringe (#309604, Becton Dickinson), marrow was flushed from the bones into a 50 mL conical centrifuge tube (BD Falcon™, #352070, Becton Dickinson Labware, Franklin Lakes, NJ) containing 25 mL of GM. Marrow plugs in the medium were disrupted with 16, 18, and 22 1/2-gauge needles. The marrow suspension was centrifuged at 450 g for 5 min (Beckman AccuSpin FR™, Beckman, Schaumberg, IL), and the whole-marrow pellet reconstituted in GM and plated on 100 mm tissue culture dishes (BD Falcon®, #353003, Becton Dickinson, San Jose, CA) as passage 0 (P_0) cultures at approximately 2 legs per dish, 10 mL per dish. The non-adherent, hematopoietic sub-population of the whole marrow was removed with subsequent rinses and medium replacements, the first of which was performed 3 d after the initial plating.

Tendon fibroblasts

For details refer to Calve et al. [239]. During the extraction of soleus muscle from the hindlimbs of anesthetized rats, Achilles tendons were removed from the hindlimbs of anesthetized rats and placed in TM. When ready for disassociation, tendon tissue

samples were rinsed briefly in DPBS, the tendon separated from the residual muscle, minced with a razorblade, and placed into the soft tissue digestion solution ($\sim 2\,\text{mL}$ per tendon). These tissue samples were allowed to disassociate for $4\,\text{h}$–$6\,\text{h}$ at $37\,^\circ\text{C}$ with occasional agitation. The resulting digested mixtures were centrifuged at $750\,\text{g}$ for $15\,\text{min}$, the supernatants removed by aspiration, cell/tissue pellets reconstituted in $10\,\text{mL}$ GM, and plated as P_0 on $100\,\text{mm}$ tissue culture dishes.

4.2.3 Cell culture and treatments

Physiological environmental conditions for all cell culture were provided by a humidified $5\,\%$ CO_2 incubator (Series II CO_2 Water Jacketed Incubator, #3130, Thermo Forma, Marietta, OH) set at $37\,^\circ\text{C}$. This standard configuration results in a O_2 gas fraction of $\sim 18\,\%$. Instrument-controlled subatmospheric $5\,\%$ O_2 levels for experiments were obtained by employing an OEM O_2 sensor fuel cell (Thermo Forma) and N_2 gas source (Cryogenic Gases, Southland, MI) to purge the remaining air as necessary.

Expansion

During cell culture maintenance and expansion, $100\,\text{mm}$ dishes were rinsed with $5\,\text{mL}$ DPBS and fed with $10\,\text{mL}$ GM every 2–$3\,\text{d}$. P_n cultures were passaged subconfluently as necessary: After rinsing in DPBS, $1\,\text{mL}$ $4\,^\circ\text{C}$-$0.25\,\%$ trypsin-EDTA solution (GIBCO™, #25200-072, Invitrogen) were be added to each $100\,\text{mm}$ dish and placed in $37\,^\circ\text{C}$ incubation for $10\,\text{min}$–$15\,\text{min}$. Dishes were removed, tapped to aid detachment, and so verified visually under an inverted microscope (Nikon TMS-F, #200391). Trypsin-EDTA was inactivated in excess GM and washed by centrifuging at $450\,\text{g}$ for $5\,\text{min}$ followed by supernatant removal. Cell pellets were reconstituted in GM or GM_{msc} as necessary and diluted to the required number of subcultured P_{n+1}

dishes. P_1–P_3 MSCs and P_2–P_4 TFbs were used for all experiments.

Growth

For cell growth experiments, MSCs and TFbs were raised in GM and GM_{msc}, respectively. Cells were trypsinized, washed, counted by hemacytometer (Reichert Bright-Line, #1490, Hausser Scientific, Horsham, PA) using 2 aliquots of no less than 5 fields each, and diluted to yield plating densities of $\rho_0 = 2.5 \times 10^3, 5.0 \times 10^3, 10 \times 10^3, 20 \times 10^3$ cell/cm² in GM or GM_{msc} as appropriate. For each cell type, oxygen level, time point, and ρ_0, the resulting suspensions were delivered in $100\,\mu L$ to 6 wells of 96-well tissue-culture plates (Black Plate, Clear Bottom, #3603, Costar, Corning). Half of each plate was left empty for known cell standards during enumeration. Plates were cultured under $18\,\%$ O_2 *normoxic* and $5\,\%$ O_2 *hypoxic* gaseous conditions for at least $4\,d$. Medium was replaced daily after each enumeration assay.

Short-term expression

MSCs and TFbs were both expanded in GM. Prior to experiments, low-density ($\sim 25\,\%$ confluent) cultures in $60\,mm$ tissue culture dishes (BD Falcon®, #353002, Becton Dickinson) were serum-starved in $3\,mL$ DMEM with $1\times$ AbAm and $1\times$ insulin-transferrin-selenium-X supplement (GIBCO®, #51500-056, Invitrogen) for $24\,h$. Dishes were then switched back to GM and cultured an additional $24\,h$ under normoxic or hypoxic conditions, after which dishes were taken for RNA analysis.

Long-term expression

MSCs and TFbs were cultured in GM and GM_{msc}, respectively. Cells were trypsinized, washed, counted, and diluted for $\rho_0 = 20 \times 10^3$ cell/cm² in GM or GM_{msc} as appropriate. For each cell type, oxygen level, time point, and analysis type (messenger RNA (mRNA) or protein), cells were plated on $35\,mm$ dishes (BD Falcon®,

#353002, Becton Dickinson) in 1.5 mL medium. Dishes were cultured under normoxic or hypoxic conditions for 2, 4, 6, or 8 d after which monolayers were taken for either RNA or protein analysis.

4.2.4 Cell growth

Enumeration

On selected days, cells in standards plates were trypsinized, washed, counted by hemacytometer (Reichert Bright-Line, #1490, Hausser Scientific, Horsham, PA), and diluted over a range of concentrations spanning the expected unknown cell densities. Cell cultures in 96-well plates and standards in tubes were fixed with 70 % ethanol and permeabilized in 0.5 % Triton X-100 for 15 min each and stained with 0.5 μM SYTOX Green nucleic acid stain (#S7020, Invitrogen). SYTOX green, like most dead-cell stains, readily enters cells with compromised membranes but remains excluded from live cells. It undergoes a $> 500\times$ increase in fluorescence after binding to nucleic acids, resulting in an intense nuclear signal with very low cytoplasmic and extracellular background (even though it binds both deoxyribonucleic acid (DNA) and ribonucleic acid (RNA)) that does not require a wash step. Fluorescence was measured in a plate reader (GENios, Tecan, Mannedorf, Switzerland) until reaching steady state (1 h–2 h) with 485 nm excitation and 535 nm emission with cell density interpolated from linear regression of the standard curve ($R^2 \geq 0.95$).

Growth kinetics

The cell density ρ at time t for perfect exponential doubling from plating density ρ_0 is

$$\rho = \rho_0 \cdot 2^{t/\tau_{\mathrm{dbl}}}, \tag{4.1}$$

where τ_{dbl} is the population doubling time. If the number of population doublings N_{dbl} are given as

$$N_{\mathrm{dbl}} = \log_2 \frac{\rho}{\rho_0}, \tag{4.2}$$

then combining Eq. 4.1 and Eq. 4.2 yields

$$\underbrace{N_{\mathrm{dbl}}}_{y} = \frac{1}{\underbrace{\tau_{\mathrm{dbl}}}_{m}} \underbrace{t}_{x}. \tag{4.3}$$

The linear portion of the experimental growth curves constructed by Eq. 4.2 over 4 d was regressed linearly to Eq. 4.3. Due to natural plating inefficiencies and lag time, the $b = 0$ intercept constraint in Eq. 4.3 was relaxed during actual regression focusing instead on the slope m of the growth curve Eq. 4.2 such that

$$\tau_{\mathrm{dbl}} = \frac{1}{m}. \tag{4.4}$$

4.2.5   RNA analysis

All molecular biology reagents, buffers, and plasticware used were nuclease-free and prepared with deionized, sterile-filtered water (qH_2O).

Isolation

After the selected durations, cells were rinsed in DPBS and lysed directly in 350 µL guanidine thiocyanate buffer (Buffer RLT, #79216, QIAGEN, Valencia, CA). The lysates were scraped (Cell Lifter, #3008, Costar, Corning) and homogenized in QIAshredder spin columns (QIAGEN, #79654). The homogenates were combined 1:1 with 70 % EtOH and total RNA isolated with the RNeasy Mini Kit (#74104, QIAGEN) according to manufacturer's instructions. An on-column DNase I digestion step (RNase-Free DNase Set, #79254, QIAGEN) was included to minimize gDNA co-purification. RNA was eluted in qH_2O with 1–3 spins as necessary to concentrate the eluate.

Quantitation

Total RNA concentration was determined using a NanoDrop 1000 Spectrophotometer (Thermo Fisher Scientific, Wilmington, DE) with a $1.5\,\mu L$ quantitation volume according to $c_{\mathrm{rna}} = A_{260}/0.025\,\mathrm{ng/\mu L}$. Sample purity ratios A_{260}/A_{280} were 2.03 ± 0.003 among all samples indicating negligible protein co-purification. Samples were stored in qH$_2$O at -80 °C until ready for use.

Integrity

Integrity of total RNA samples was qualitatively assessed by agarose gel electrophoresis (AGE) (Tables 4.9 and 4.10). RNA samples were combined 1:1 with glyoxal sample buffer (#50560, Lonza, Rockland, ME) and loading dye (Blue/Orange Loading Dye, 6X, #G190A, Promega, Madison, WI). RNA markers ($0.5\,\mathrm{kbp}$–$9\,\mathrm{kbp}$, #50575, Lonza) and $0.5\,\mu g$–$2.0\,\mu g$ RNA samples were loaded and electrophoresed in a $1.0\,\%$ agarose (SeaKem GTG, #50070, Lonza) and $0.005\,\%$ ethidium bromide (EtBr) gel with a Kodak cell (BioMax MP1015) and $1\times$ MOPS buffer (#50876, AccuGENE, Lonza) at $60\,V$ for $2\,h$. Gels were visualized with transilluminating UV light in a chemiluminescent documentation system (FluorChem SP, Alpha Innotech, San Leandro, CA).

Reverse transcription

reverse transcription (RT) for first-strand synthesis of complementary DNA (cDNA) from RNA was done with the Omniscript RT Kit (#205111, QIAGEN) and prepared on ice. The reactions (Table 4.2) consisted of kit components $10\times$ Buffer RT ($2\,\mu L$), deoxy-nucleotide phosphates (dNTPs) ($2\,\mu L$), and reverse transcriptase ($1\,\mu L$) supplemented with RNaseOUT Recombinant Ribonuclease Inhibitor ($10\,U$ in $0.25\,\mu L$; #10777-019, Invitrogen), oligo dT$_{15}$ primers ($2\,\mu L$, Integrated DNA Technologies,

Coralville, IA), and RNA in qH$_2$O (1 µg MSC RNA or 2 µg TFb RNA in 12.75 µL).
The 20 µL reactions were carried out at 37 °C for 60 min, diluted to a final volume of
50 µL in qH$_2$O, and stored at -80 °C until ready for use.

Primer design

Primer-pairs for amplification gene-transcript–specific cDNAs were designed (with
the assistance of the Universal ProbeLibrary's Probefinder for Rat [264] and Primer3 [262])
to anneal to sequences flanking at least one intron to distinguish between cDNA and
contaminating genomic DNA (gDNA) amplification products (amplicons) and, when
possible, to span an intron-exon boundary so as to eliminate potential gDNA ampli-
fication altogether. Sequences and associated parameters are in Table 4.1.

Efficiency   The copy number N of a sequence of starting quantity N_0 at polymerase
chain reaction (PCR) cycle c with a primer set of efficiency E is

$$N = N_0 \left(1 + E\right)^c.$$ (4.5)

If the amplified copy number reaches a fixed threshold N^* (associated with a fluo-
rescence level f^*) at a threshold cycle c^*, a relative dilution series of cDNA can serve
as a sequence of N_0 and be used to construct a standard curve of c^*'s as a function
of $\log_2 N_0$. Rearranging Eq. 4.5,

$$\underbrace{c^*}_{y} = \underbrace{\frac{\log_2 N^*}{\log_2 1 + E}}_{b} + \underbrace{\frac{-1}{\log_2 1 + E}}_{m} \underbrace{\log_2 N_0}_{x},$$ (4.6)

so

$$E = 2^{-1/m} - 1,$$ (4.7)

and where m is the slope of the *efficiency standard curve* ($R^2 \geq 0.995$).

Table 4.1: Primer-pair sequences for qPCR analysis.

Gene	Local Symbol	RGD [261] Symbol	NCBI [267] Accession #	Forward (5'–3')	Reverse (3'–5')	l_{cdna} (bp)	l_{gdna} (bp)	E (%)
Smooth muscle α-actin	a-SMA	Acta2	NM_031004	gatctggcaccactccttct	gttggccttagggttcagc	94	94	93.0
Actin, β	β-Act	Actb	NM_031144	ccaaccgtgaaaagatgacc	accagaggcatacagggaca	98	564	94.7
Alkaline phosphatase, liver/bone/kidney	AP	Alpl	NM_013059	aggggcaactccatttttg	agacgttctccgttcacc	124	666	100.0
β-2 μglobulin	β2-μg	B2m	NM_012512	tgaccgtgatctttctggtg	atctgaggtgggtggaactg	151	2921	94.8
(Pro)collagen, type I, α1	Col1a1	Col1a1	NM_053304	cctggacagcgctggacttc	ccataggacatctgggaagc	95	1026	85.0
(Tropo)elastin	Eln	Eln	NM_012722	cggtggcttaggagtctcaa	cctggaagaccgacacaca	102	840	100.0
Glyceraldehyde-3-phosphate dehydrogenase	GAPDH	Gapdh	NM_017008	tggaaagctgtggcgtgat	tgcttcaccacctttgat	216	300	100.0
Hypoxanthine phosphoribosyl-transferase	HPRT	Hprt1	NM_012583	ctcctcagaccgcttttcc	tcataacctggttcatcatcactaa	93	9632	85.6
Myosin, heavy chain 10 (IIB), non-muscle	NMMHC	Myh10	NM_031520	agggacctgcaaaccagag	ctgcttccgctcatcctc	102	877	88.6
Osteocalcin/Bone γ-carboxyglutamate protein	Ocn	Bglap	NM_013414	tcaacccaattgtgacgag	gagtcctggagagtagccaa	138	0	100.0
60S ribosomal protein L13A	RPL13	Rpl13a	NM_173340	ggcagggtctaaaatgcaaa	aggaggtgggagatgttggt	126	632	100.0
Scleraxis	Scx	Scx	NM_001130508	ggcctccagctacatttctc	ctgtggaagaaagcgggtc	99	99	100.0
Tenomodulin	Tnmd	Tnmd	NM_022290	ctgggagaccatggcaaa	tccacaaatcttcagtgatttacg	109	274	95.4

Quantitative polymerase chain reaction

PCRs were prepared for quantitative, real-time analysis using the QuantiTect SYBR Green PCR Kit (#204143, QIAGEN). PCR components were prepared on ice as follows (Table 4.3): 12.5 µL 2× kit master mix, 0.75 µL each forward and reverse primers for gene-specific detection, and 11 µL qH$_2$O containing cDNA derived from 20 ng RNA template. Each gene-sample combination was prepared in tubes in excess for triplicate reactions and only then delivered to three wells of a 96-well PCR plate (#223-9441, Bio-Rad), and sealed with optically transparent film (Microseal 'B', #MSB1001, Bio-Rad). cDNA was amplified by PCR in a MyiQ real-time thermal cycler (Bio-Rad) according to the protocol in Table 4.4.

Product specificity

Single PCR-product verification was assessed by inspection for single peaks in the $-\partial f/\partial T$ melt curve (performed and calculated automatically in the iQ5 Optical System Software [238]; Figs. 4.12–4.16) and single bands at the predicted molecular weights by DNA AGE (Tables 4.11–4.15). PCRs not satisfying these criteria were removed from analysis. For DNA AGE, 20 µL of quantitative PCR (qPCR) products were combined with 4 µL loading dye; these samples and 100 bp DNA ladders (#G210A, Promega) were loaded and electrophoresed in a 2.0 % agarose and 0.005 % EtBr gel with a Kodak cell and 1× TBE buffer (#50843, AccuGENE, Lonza) at 100 V for 1 h. Gels were visualized with transilluminating UV light in a FluorChem SP chemiluminescent documentation system.

Gene expression

Relative mRNA levels were determined using the method of Pfaffl [260]. This is based on the traditional $\Delta\Delta C_t$ method of Livak and Schmittgen [254], but corrects

Table 4.2: RT reaction components.

Component	Initial	Final	Volume (µL)
Buffer RT	$10\times$	$1\times$	2
dNTP mix	$5\,\text{mM}$	$0.5\,\text{mM}$	2
oligo dT$_{15}$	$10\,\text{µM}$	$1\,\text{µM}$	2
Reverse transcriptase	$4\,^\text{U}/_\text{µL}$	$4\,\text{U}$	1
RNase inhibitor	$40\,^\text{U}/_\text{µL}$	$10\,\text{U}$	0.25
RNA + qH$_2$O	$\sim$	$1\text{-}2\,\text{µg}$	12.75
Total	$\sim$	$\sim$	20

Table 4.3: qPCR components.

Component	Initial	Final	Volume (µL)
Master mix	$2\times$	$1\times$	12.5
Forward primer	$10\,\text{µM}$	$0.3\,\text{µM}$	0.75
Reverse primer	$10\,\text{µM}$	$0.3\,\text{µM}$	0.75
cDNA + qH$_2$O	$\sim$	$20\,\text{ng}$	11
Total	$\sim$	$\sim$	25

Table 4.4: qPCR cycling protocol.

Step	Time	Temperature (°C)	Repetitions
DNA polymerase activation	$15\,\text{min}$	95	1
Denaturation	$15\,\text{s}$	94	
Annealing	$30\,\text{s}$	60	40
Extension and data acquisition	$30\,\text{s}$	72	
Melting curve	$10\,\text{sec}$	55–95, $\Delta = 1$	1

for non-unity primer-pair efficiencies. The *normalized relative expression* $m_{\Delta\Delta}$ of a target gene is given as

$$m_{\Delta\Delta} = \frac{(1+E)^{-\Delta c^*}}{(1+E_0)^{-\Delta c_0^*}}, \qquad\qquad \Delta c^* = c^* - c_0^*. \qquad (4.8)$$

Here, E is the efficiency of the target gene, E_0 is the efficiency of an endogenous reference gene, and c_0^* is the threshold cycle for an inter-run calibrator (IRC) sample to provide normalization across all plates of a particular cell type. Δc_0^* is calculated according to Eq. 4.8_2 referring to the difference in threshold cycles of the reference gene rather than the target gene. When $E = E_0 = 1$, Eq. 4.8_1 reduces to the classical Livak and Schmittgen [254] equation $m_{\Delta\Delta} = 2^{\Delta\Delta c^*}$.

The reference gene was chosen from a pool of housekeeping genes based on its minimal variation among experimental conditions in validation qPCRs (data not shown). For short-term ($< 24\,\mathrm{h}$) O_2 experiments, β_2-microglobulin (β_2-μg) provided the most stable reference for both MSCs and TFbs, while for long-term experiments β-actin (β-Act) was utilized.

4.2.6 Protein analysis

Extraction

After the selected durations, cells were rinsed in DPBS and lysed directly in $250\,\mu\mathrm{L}$–$500\,\mu\mathrm{L}$ sample buffer (SB) consisting of Laemmli's sample buffer (#161-0737, Bio-Rad) base with $5\,\%$ β-mercaptoethanol (#161-0710, Bio-Rad) and $5\,\%$ protease inhibitor cocktail (#P2714, Sigma, Sigma-Aldrich). The lysates were scraped, homogenized, heated at $95\,°\mathrm{C}$ for $10\,\mathrm{min}$, and stored at $-20\,°\mathrm{C}$.

Quantitation

Total protein concentration was determined using an *RC DC* protein assay kit (#500-0122, Bio-Rad). The *RC DC* (reducing agent-compatible, detergent-compatible)

technology enables the efficient removal of interfering reducing agents (β-mercaptoethanol) and detergents (sodium dodecyl sulfate (SDS)) present in sample buffer, followed by Lowry-like [255] copper-binding and Folin-reducing steps that develop a blue product for colorimetric detection . Samples and bovine serum albumin (#A2153, Sigma Life Science, Sigma-Aldrich) standards were prepared in duplicate assay tubes; two RC reagent washes were employed to minimize interfering carryover. Aliquots of the end product from each tube were then pipetted in triplicate onto a 96-well assay plate (#3370, Costar, Corning) and absorbance measured at 650 nm with a plate reader (GENios, Tecan). Unknown protein concentrations of samples were calculated by linear regression of the associated standard curve ($R^2 \geq 0.95$).

Immunoblot

Duplicate blots (gels and membranes) were carried out in parallel. A common MSC or TFb positive-control sample was included on every blot of each cell type to provide inter-membrane and IRC.

Electrophoresis   Samples were heated to 55 °C and diluted in SB to equal-protein concentrations. Molecular weight standards (Precision Plus Protein Standards Kaleidoscope, #161-0375, Bio-Rad) and equal–total-protein ((2.5 µ–15 µ)) samples were resolved by molecular weight by SDS-polyacrylamide gel electrophoresis (PAGE)) in 7.5 % Tris-HCl gels (Ready Gel, #161-1118, Bio-Rad) in Tris-Glycine-SDS (TGS; #161-0732, Bio-Rad) RB with a Mini PROTEAN®3 Cell (#, Bio-Rad) at 30 mA/gel for 60 min.

Electroblot/Protein transfer   Following SDS-PAGE, 0.45 µm pore-size PVDF membranes (Immobilon-P, #IPSN07852, Millipore, Burlington, MA) were activated

in 100 % EtOH for 1 min, rinsed in qH$_2$O for 5 min, and equilibrated for 10 min in transfer buffer (XB) consisting of 10× TGS diluted with 80 % qH$_2$O+20 % EtOH. Blot sandwiches were assembled and proteins electroblotted by tank transfer in XB with a Mini PROTEAN®3 Cell and Mini Trans-Blot Module transfer apparatus (#170-3935, Bio-Rad) at 100 V for 60 min.

Immunodetection   All blocking and primary antibody incubation steps were done overnight at 4 °C, while secondary antibody incubations were at room temperature for 60 min each, all with rocking. Membrane washes were done with T-TBS (0.1 % Tween 20 (#BP337-500, Fisher Scientific, Fair Lawn, NJ) in tris-buffered saline (#170-6435, Bio-Rad)).

Collagen I   Membranes were blocked with 1 % normal rabbit serum (RS) (#PLN5001, Invitrogen, Camarillo, CA) in Tween 20–tris-buffered saline (T-TBS). Membranes were rinsed briefly 3× and incubated with a biotinylated rabbit polyclonal anti-collagen I antibody (#ab6577, Abcam, Cambridge, MA) diluted 1:5000 in T-TBS with 0.5 % RS. Each membrane was rinsed 5× for 5 min each in T-TBS and then incubated with Vectastain Elite ABC (Standard) reagents (1 drop REAGENT A + 1 drop REAGENT B in 10 mL T-TBS per membrane; #PK-6100, Vector Laboratories, Burlingame, CA). The ABC technology couples the high-affinity of the avidin-biotin system with horseradish peroxidase (HRP) to produce, when combined with an enzyme substrate, a signal with extremely low background. Membranes were rinsed well 5× for 5 min, and then incubated under 3 mL (working) enhanced chemiluminescent (ECL) reagents (SuperSignal West Dura Extended Duration Substrate, #34075, Pierce Biotechnology, Thermo Scientific) for 3 min. Excess ECL substrate was removed and the membrane was imaged in a chemiluminescent docu-

mentation system (FluorChem SP, Alpha Innotech).

β-tubulin (β-Tub)   Following 3 brief washes, membranes were placed in stripping buffer (Restore™Western Blot Stripping Buffer, #21059, Pierce Biotechnology, Thermo Scientific, Rockford, IL) at 60 °C for 30 min. Stripped membranes were rinsed 3× for 5 min and re-blocked with 1 % heat-inactivated normal goat serum (GS) (#PCN5000, Invitrogen) in T-TBS. Membranes were rinsed briefly 3× in T-TBS and reprobed with mouse anti–β-tubulin IgG (#E7, Developmental Studies Hybridoma Bank, Iowa City, IA) 1:1000 in T-TBS with 0.5 % GS. After washing 5× for 5 min, membranes were incubated in goat anti-mouse IgG-HRP conjugate (#1858413, Pierce) 1:1000 in T-TBS with 0.5 % GS. Following 5 more 5 min washes, ECL detection and visualization proceeded as above for collagen I α1 (Col1α1).

Densitometry   Bands corresponding to the intracellular Col1α1 precursor at ∼ 150 kD were isolated from images, and intensity determined using the AlphaEaseFC software's 1D-Multi analysis module [236] and a non-aggressive (Rubber Band) background subtraction method. Normalized procollagen I content p_{Col1} of samples was then calculated by averaging the intensities $\bar{I}_1, \bar{I}_2$ from the duplicate blots normalized to each blot's calibration sample intensity I_0:

$$\bar{I} \equiv \frac{I}{I_0}, \qquad\qquad p_{\mathrm{Col1}} \equiv \frac{\bar{I}_1 + \bar{I}_2}{2} \qquad\qquad (4.9)$$

4.2.7   Statistics

Results are presented as mean (expected value) $E \pm$ standard error of the mean SE. Unpaired and paired Student's t-tests were employed as appropriate to determine significant changes under the 5 % ϕ_{O_2} condition as compared to 18 %, with $p < \alpha = 0.05$ considered significant and denoted with an asterisk (∗). Sample sizes

n represent independent experiments, with each experiment deriving cells from separate tissue extractions, cell isolations, and cell expansions.

4.3 Results

4.3.1 Cell growth

MSCs and TFbs were cultured in 96-well plates from various plating densities for up to 4 d. Plates were taken daily for cell enumeration, growth curves constructed, and τ_{dbl} calculated from the linear portion of the N_{dbl}-t curve (Fig. 4.1 and Fig. 4.3). For MSCs, τ_{dbl} was significantly lower (i.e., the growth rate faster) in hypoxia at both of the lower plating densities (Fig. 4.2a; 1.1 d at 5 % versus 1.7 d at 18 % for $\rho_0 = 2.5 \times 10^3$ cell/cm² and 1.2 d at 5 % versus 1.4 d at 18 % for 2.5×10^3 cell/cm²). When considered pairwise, the average doubling time difference $\Delta\tau_{\mathrm{dbl}}$ between hypoxia versus normoxia for cohort MSCs was significantly negative additionally at $\rho_0 = 10 \times 10^3$ cell/cm² (Fig. 4.2b). Differences in growth rates were not significant with 20×10^3 cell/cm². While, in general, τ_{dbl} is expected to increase with ρ_0 for cultures fed with the same amount of medium, interestingly, τ_{dbl} actually *decreased* with respect to ρ_0 in the case of normoxia for MSCs.

On the other hand, TFbs subjected to differential culture did not grow at significantly different rates no matter the plating density (Fig. 4.4). τ_{dbl} increased slightly under both gaseous conditions from $\sim$0.7 d to $\sim$0.9 d for $\rho_0 = 2.5 \times 10^3$ cell/cm² and 20×10^3 cell/cm², respectively. Furthermore, the growth of TFbs is clearly more rapid than MSCs at any ρ_0.
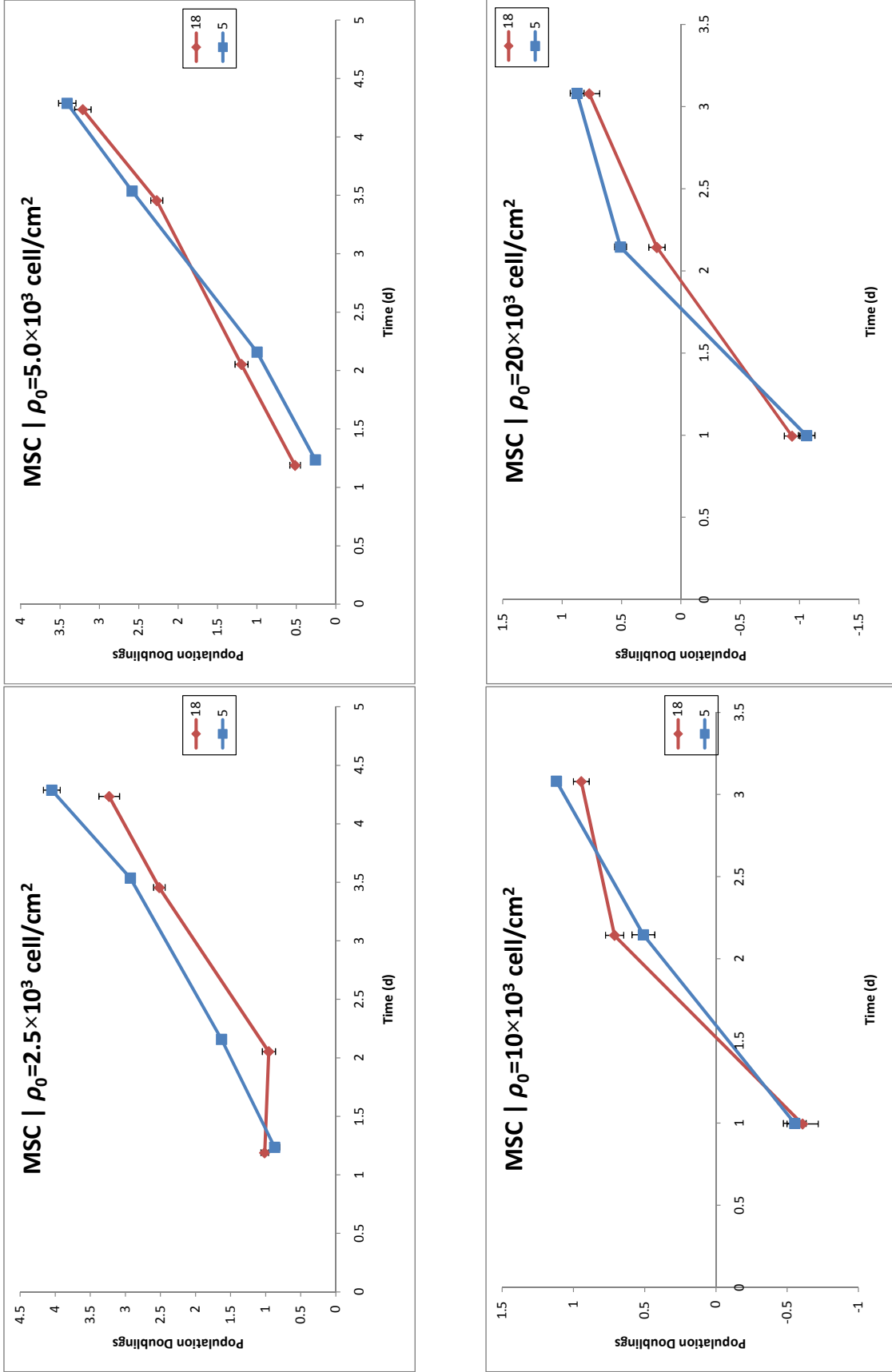
Figure 4.1: Representative growth curves of MSCs under differential ϕ_{O_2} culture for different plating densities. Population doublings N_{dbl} were calculated by $N_{dbl} = \log_2(\rho/\rho_0)$.
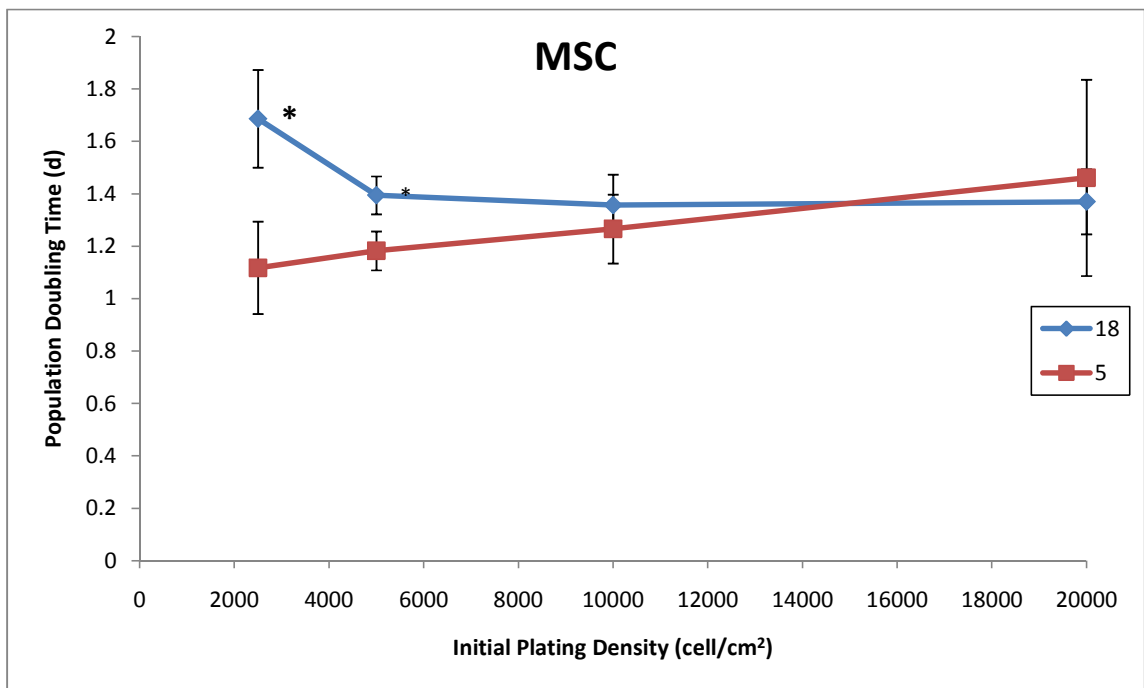
(a)
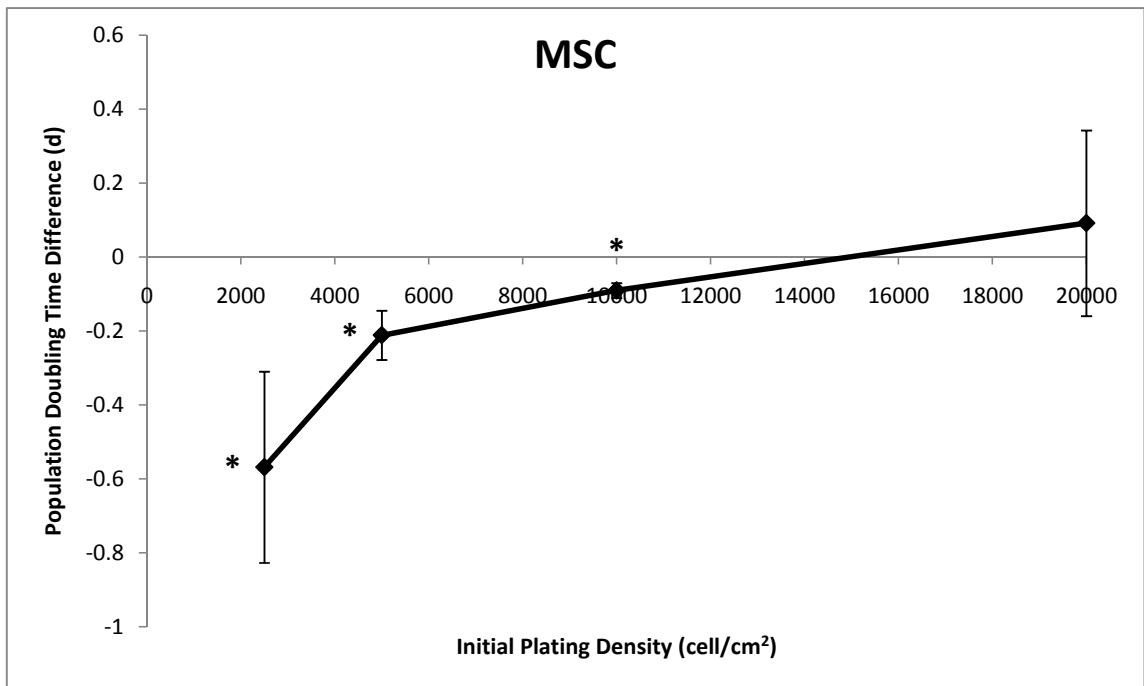
(b)

Figure 4.2: Population doubling times of MSCs under differential ϕ_{O_2} culture for different plating densities ($n = 5$).
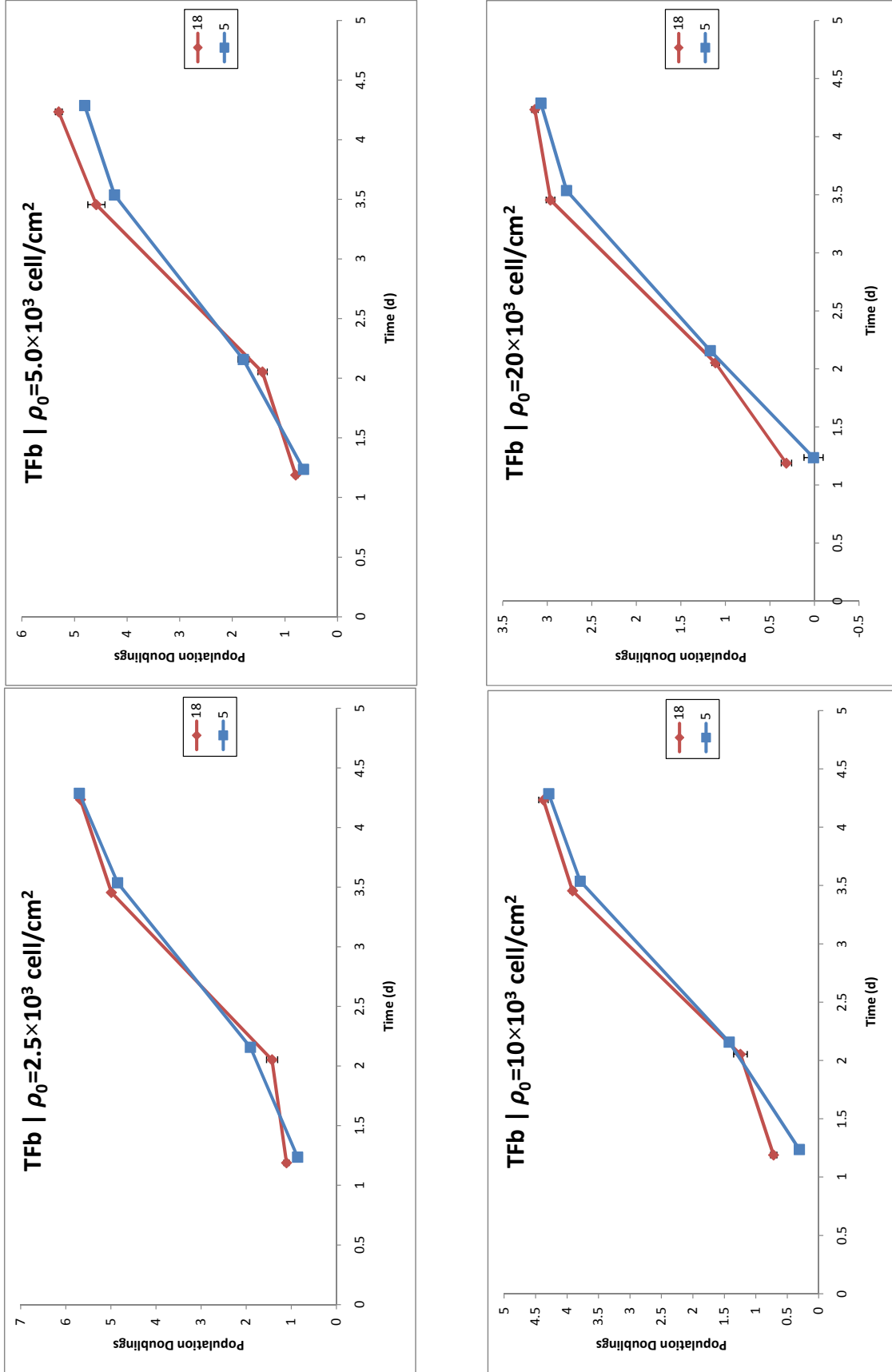
Figure 4.3: Representative growth curves of TFbs under differential ϕ_{O_2} culture for different plating densities. Population doublings N_{dbl} were calculated by $N_{dbl} = \log_2(\rho/\rho_0)$.
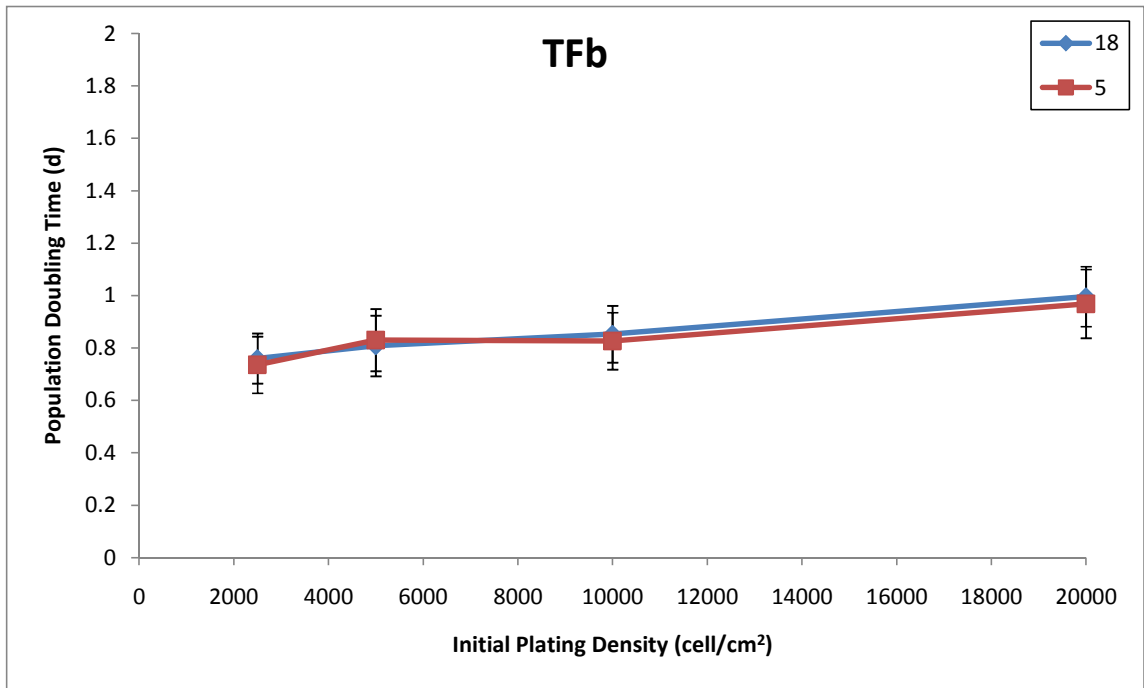
(a)
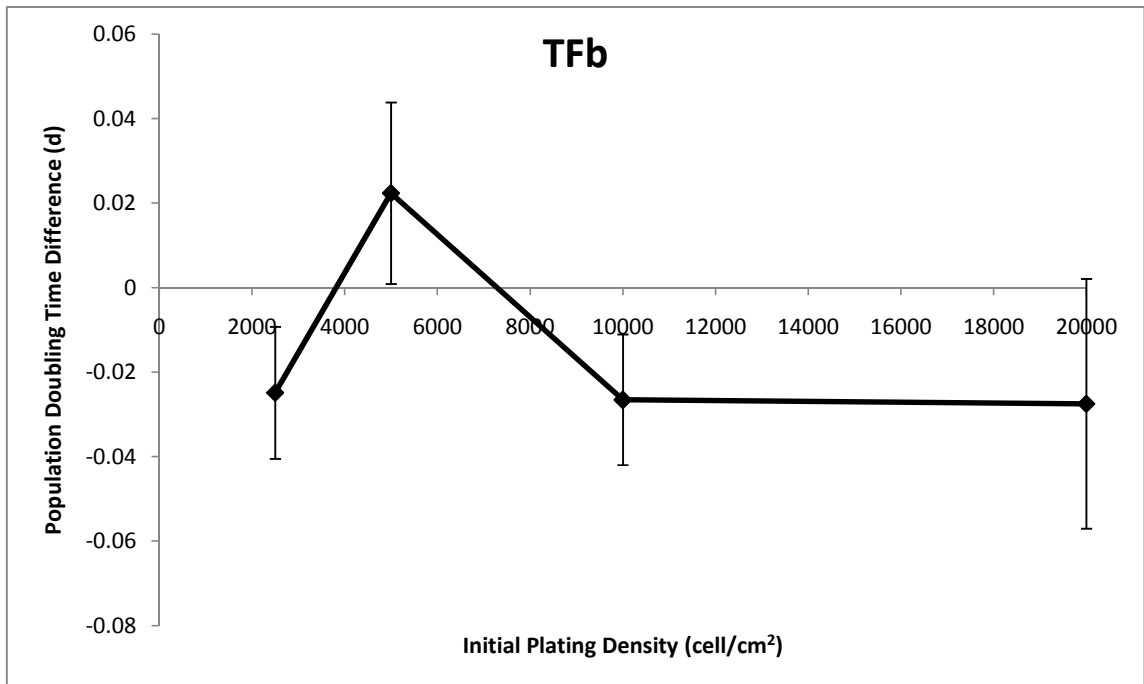
(b)

Figure 4.4: Population doubling times of TFbs under differential ϕ_{O_2} culture for different plating densities ($n \geq 4$).

4.3.2   Gene expression

Short-term expression

Subconfluent MSCs and TFbs were serum-starved for 24 h and then incubated under normoxia and hypoxia for 24 h. RNA was isolated from culture lysates, RNA samples were reverse transcribed, and cDNA products were amplified by PCR with real-time detection with primers specific for *Col1a1*, *Eln*, and *Scx* with β_2-γg as endogenous reference. This acute exposure to hypoxia resulted in nearly a doubling ($\log_2(m_{\Delta\Delta}) = 0.9$) of *Col1a1* and 40 % increase in *Eln* mRNA copy numbers with respect to normoxia for MSCs (Fig. 4.5a). *Scx* message level experienced virtually no change in these short-term experiments.

In contrast, for TFbs, *Col1a1* and *Eln* messages exhibited no significant differences between oxygenation conditions Fig. 4.5b. *Scx*, however, dropped significantly in level ($\log_2(m_{\Delta\Delta}) = -0.4$) by the end of 24 h hypoxia.

Long-term expression

To elaborate on the 24 h study, MSCs and TFbs were cultured for up to 8 d in differential oxygenation with samples taken for RNA analysis as above every 2 d. Cell monolayers were visually similar in terms of density and morphology by light microscopy over the time course of the experiments (Table 4.5 and Table 4.6).

Col1a1 expression in MSCs increased monotonically for the duration of the experiment (Fig. 4.6). When considering the paired changes in expression in the experiments, there was a biphasic upregulation of *Col1a1* in hypoxia: nearly a twofold increase at $t = 2$ d and a 75 % at 6 d (both significant). However, there were no such observed differences at days 4 and 8. For TFbs, the *Col1a1* message time course was also again generally increasing (Fig. 4.7). The paired differences, like MSCs, oscil-
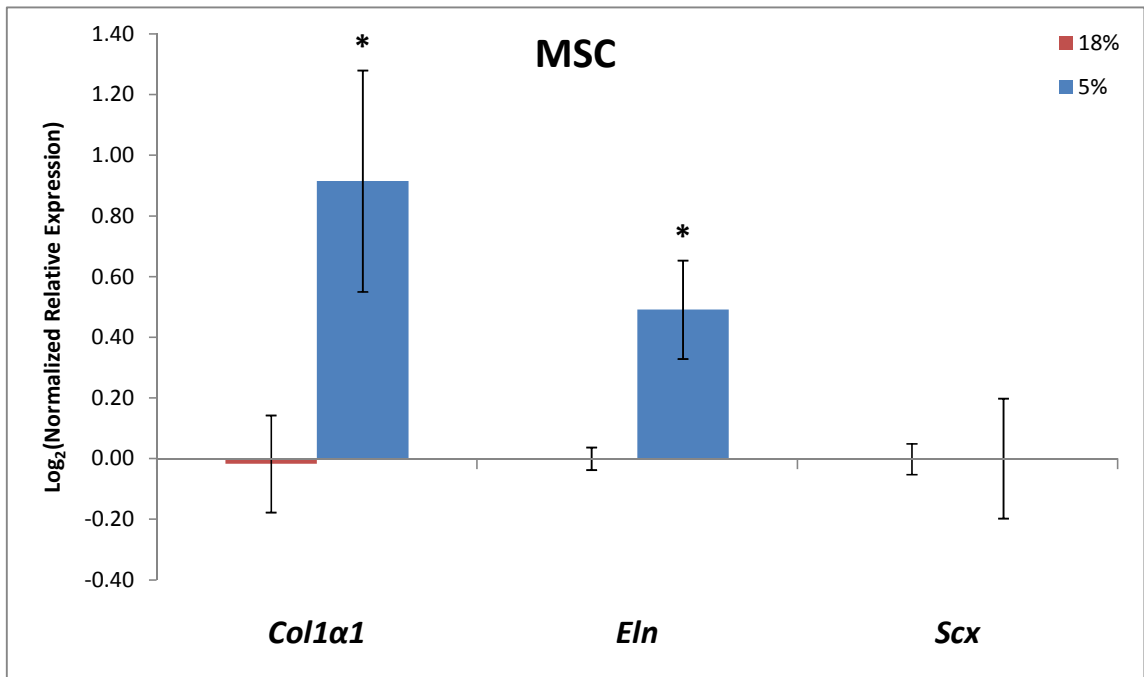
(a) MSCs.
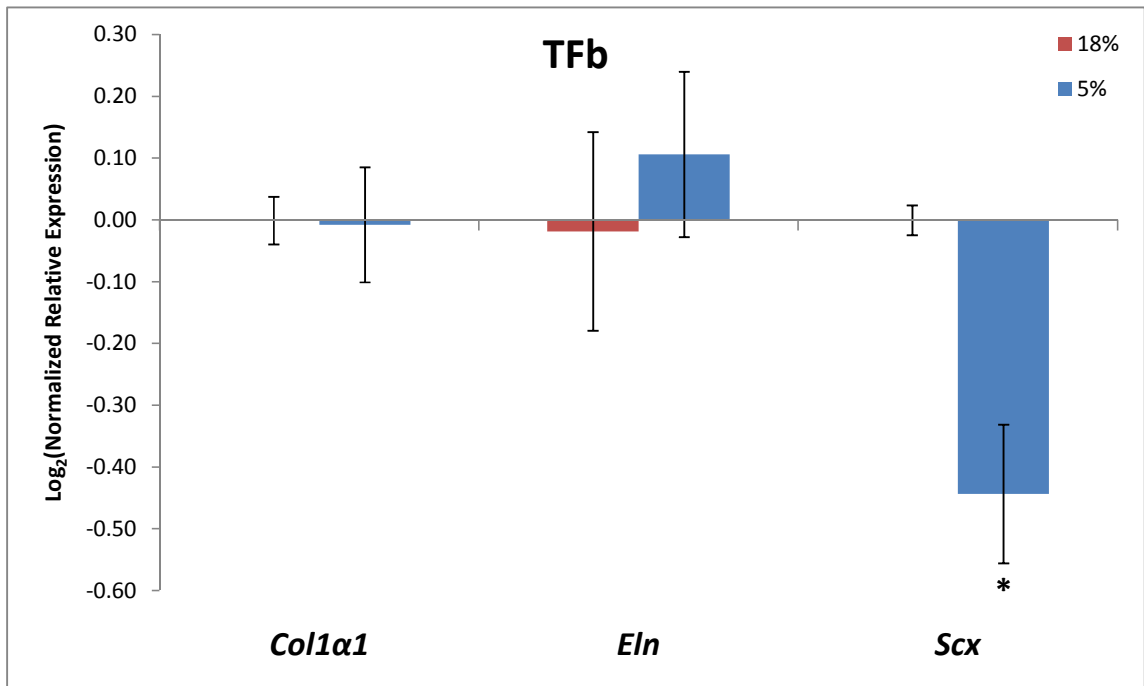
(b) TFbs.

Figure 4.5: mRNA levels as $\log_2(m_{\Delta\Delta})$ of fibroblastic genes in MSCs under short-term (24 h) differential ϕ_{O_2} culture ($n = 3$). $m_{\Delta\Delta}$ was determined relative to β_2-γg and normalized to the normoxic condition.

Table 4.5: Representative micrographs of MSC density and morphology from time-course study prior to sample collection.
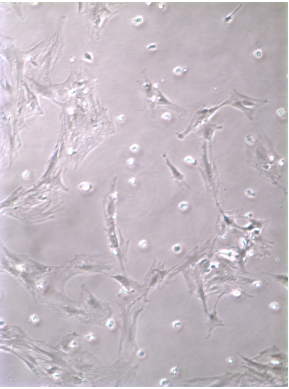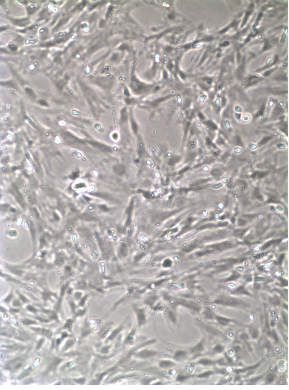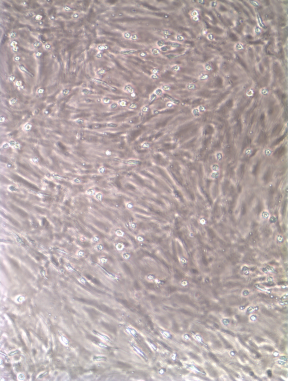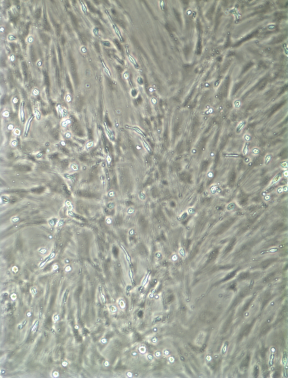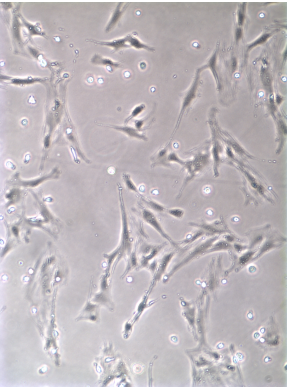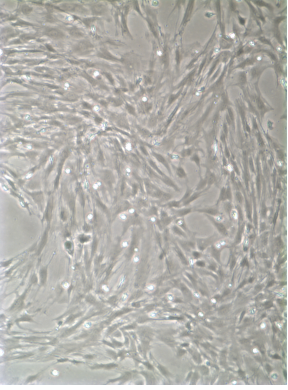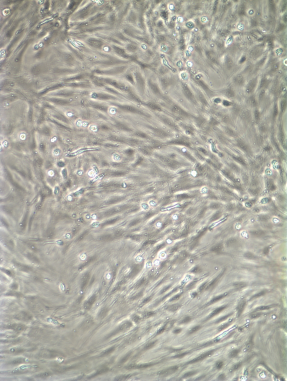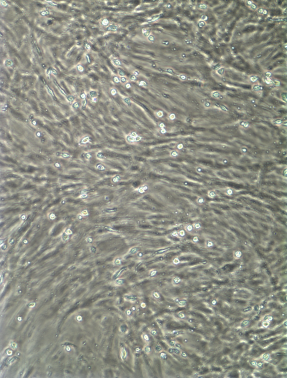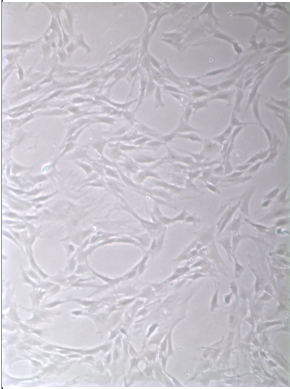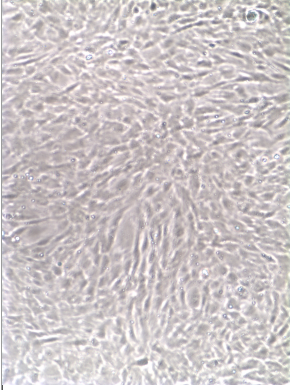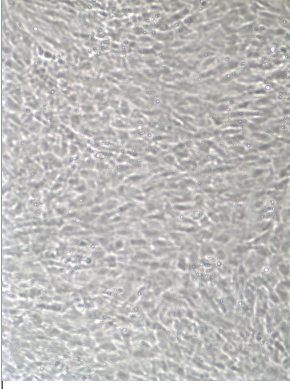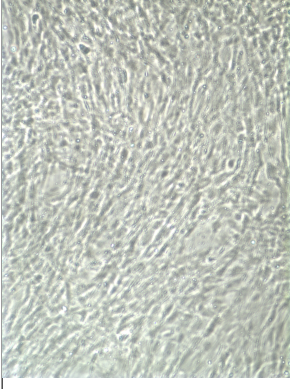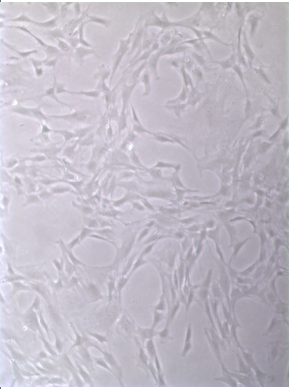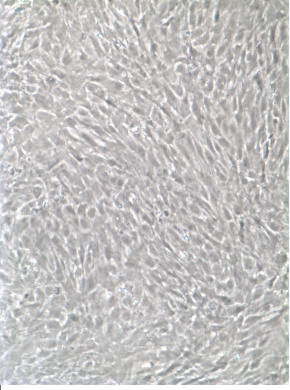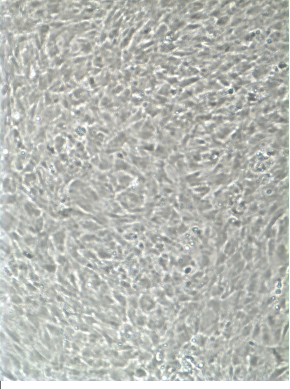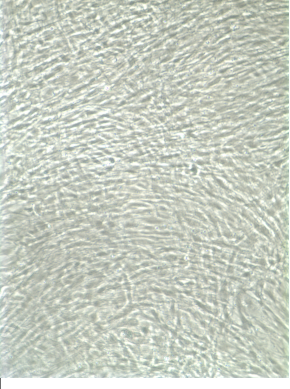
Table 4.6: Representative micrographs of TFb density and morphology from time-course study prior to sample collection.

ϕ_{O_2}	2 d	4 d	6 d	8 d
18 %				
5 %				

lated in time, with halving downregulation at 4 d, upregulation at 6 d, and reduction of more than half on day 8 d (all significant).

The overall levels of MSC *Scx* mRNA followed no obvious pattern in time (Fig. 4.8a). Pairwise (Fig. 4.8b), *Scx* expression increased significantly in the medium term (4 d and 6 d) while showing no significant changes at the beginning and end of the experiment. The 8 d data suggest that differential *Scx* mRNA is decreasing. The TFb *Scx* mRNA-time curves have no significant slope (Fig. 4.8a), but here again there is a transient pairwise upregulation at days 4 and 6 d, with the overall curve concave-down (Fig. 4.8b).
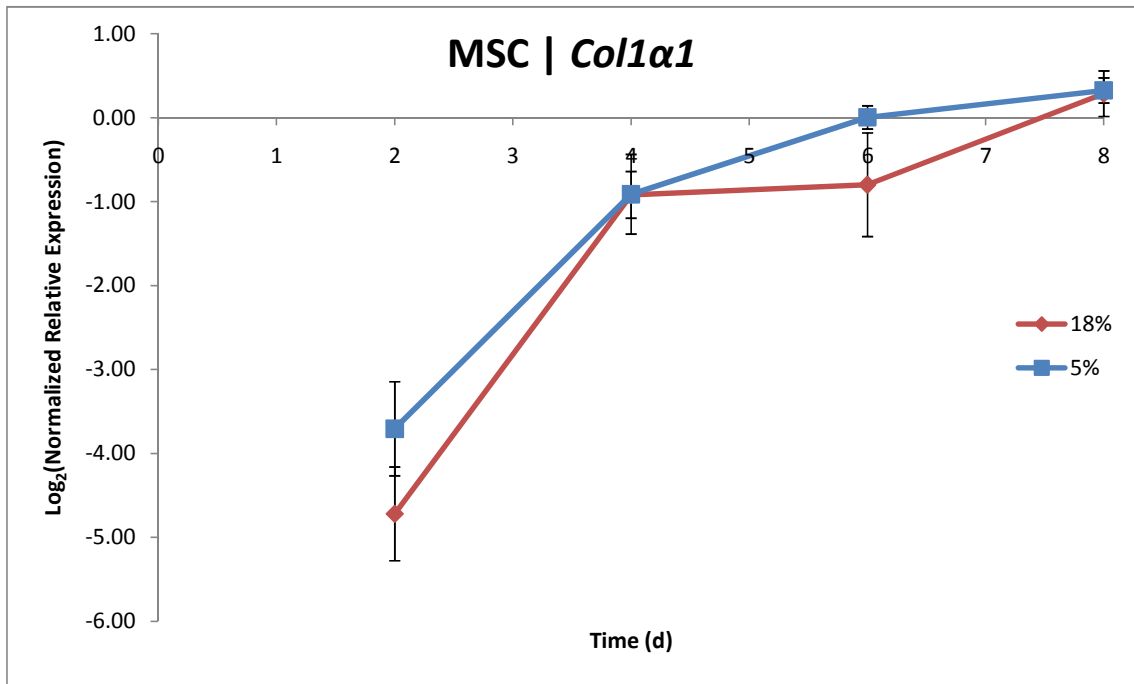
(a) Unpaired.
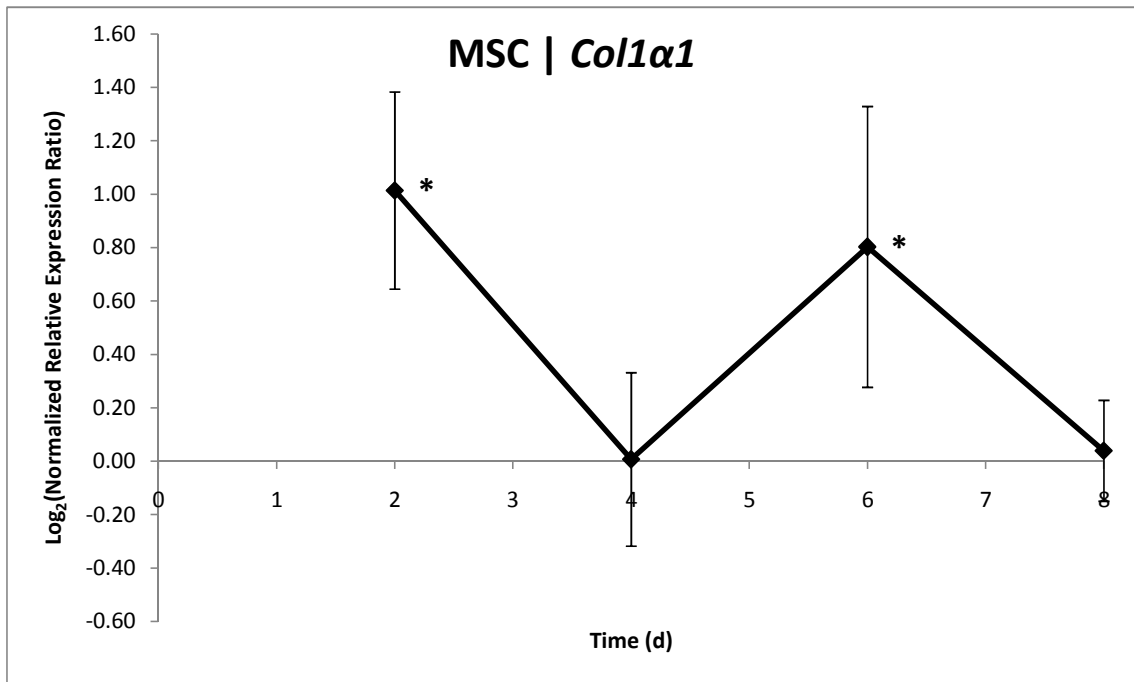
(b) Paired.

Figure 4.6: *Col1a1* mRNA levels in MSCs under extended differential ϕ_{O_2} culture ($n \geq 6$). $m_{\Delta\Delta}$ was determined relative to β-*Act* and normalized to an IRC.

(a) Unpaired.

(b) Paired.

Figure 4.7: $Col1a1$ mRNA levels in TFbs under extended differential ϕ_{O_2} culture $(n \geq 5)$. $m_{\Delta\Delta}$ was determined relative to $\beta\text{-}Act$ and normalized to an IRC.

112
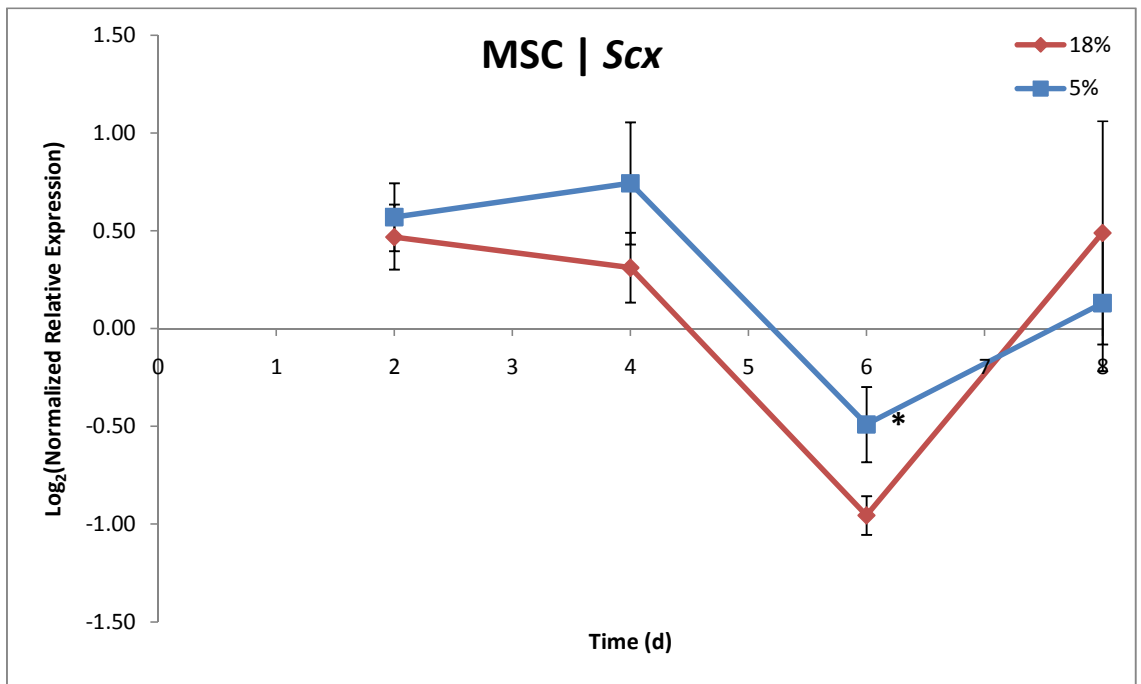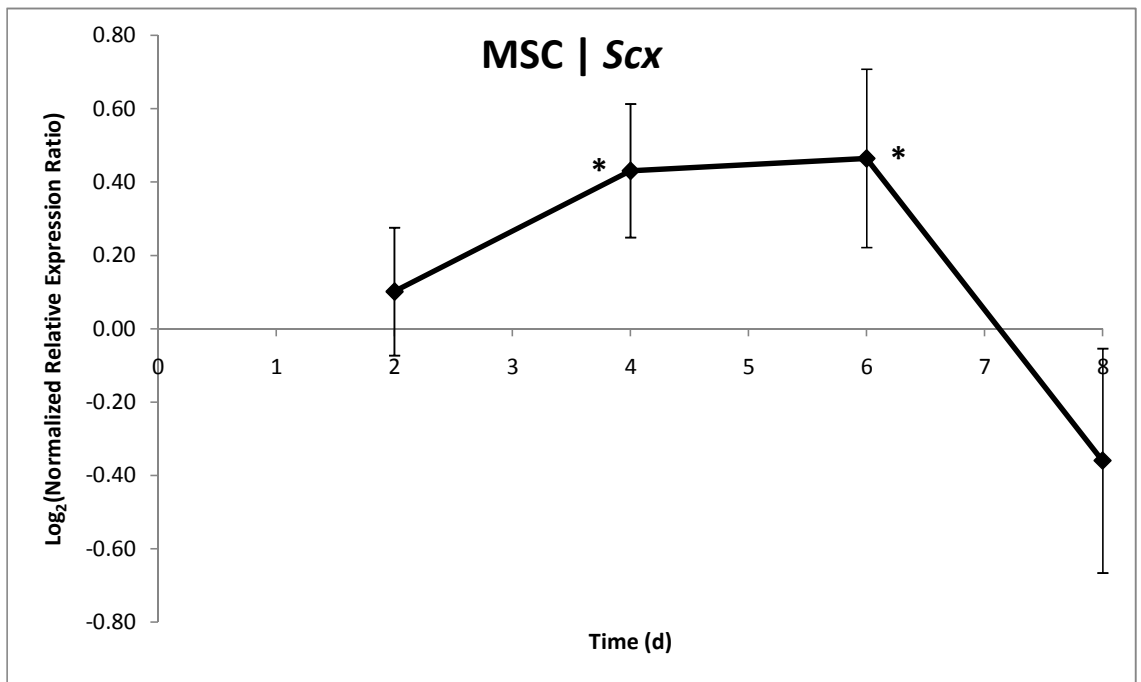
(a) Unpaired.

(b) Paired.

Figure 4.8: *Scx* mRNA levels in MSCs under extended differential ϕ_{O_2} culture ($n \geq 6$). $m_{\Delta\Delta}$ was determined relative to β-*Act* and normalized to an IRC.
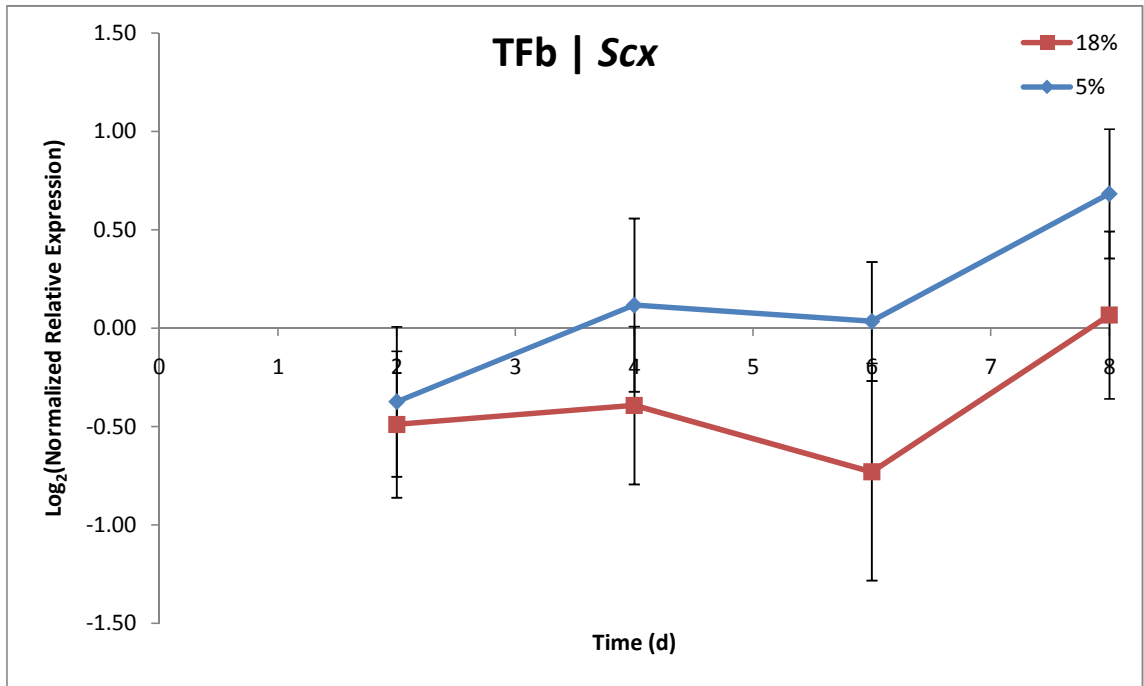
(a) Unpaired.
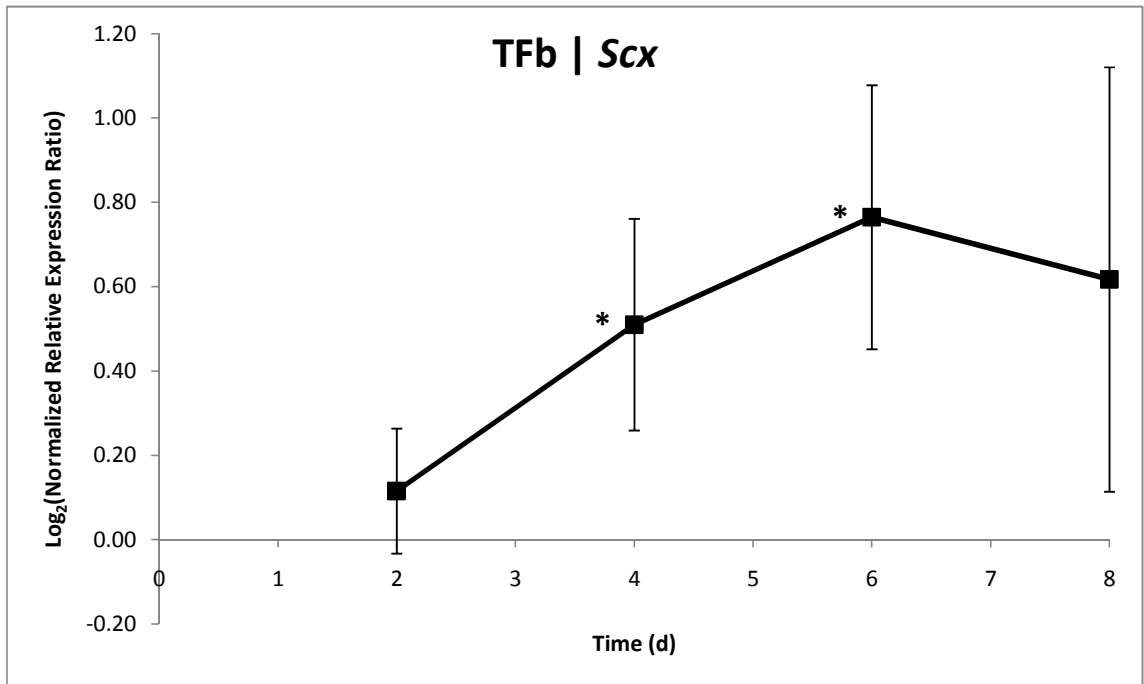
(b) Paired.

Figure 4.9: *Scx* mRNA levels in TFbs under extended differential ϕ_{O_2} culture ($n \geq$ 5). $m_{\Delta\Delta}$ was determined relative to β-*Act* and normalized to an IRC.

4.3.3 Protein content

In cohort with the time-course mRNA analysis, MSC and TFb samples were lysed for immunoblot: equal protein amounts were separated in duplicate by SDS-PAGE, transferred to polyvinylidene fluoride (PVDF) membranes, and probed for the Col1α1 precursor protein with a biotinylated collagen antibody and counterstained with β-Tub. Representative blots are shown in Table 4.7 and Table 4.8 and all analyzed blots are available in §4.4.1 in Tables 4.16 and 4.17. Overall MSC *Col1a1* content was oscillatory over time (Fig. 4.10), but there was a significant 40 % pairwise doubling at 2 d. No additional significant differences were found, but the oscillatory nature of the paired-ratio curve mirrors that of Col1α1 (Fig. 4.6b): levels are up at day 2, no or negative differences on 4 d or 8 d, with a possible increase at day 6. TFb Col1α1 content was similarly oscillatory overall, but exhibited no significant changes in normoxia versus hypoxia (Fig. 4.11).

Table 4.7: Representative immunoblots for Col1α1 target protein and β-Tub loading control in MSCs in time under differential ϕ_{O_2} .

Replicate	Protein	2 d		4 d		6 d		8 d		MW
		18 %	5 %	18 %	5 %	18 %	5 %	18 %	5 %	(kD)
1	Col1α1									150
	β-tub									55
2	Col1α1									150
	β-tub									55

Table 4.8: Representative immunoblots for Col1α1 target protein in TFbs in time under differential ϕ_{O_2} .

Replicate	Protein	2 d		4 d		6 d		8 d		MW
		18 %	5 %	18 %	5 %	18 %	5 %	18 %	5 %	(kD)
1	Col1α1									150
2	Col1α1									150
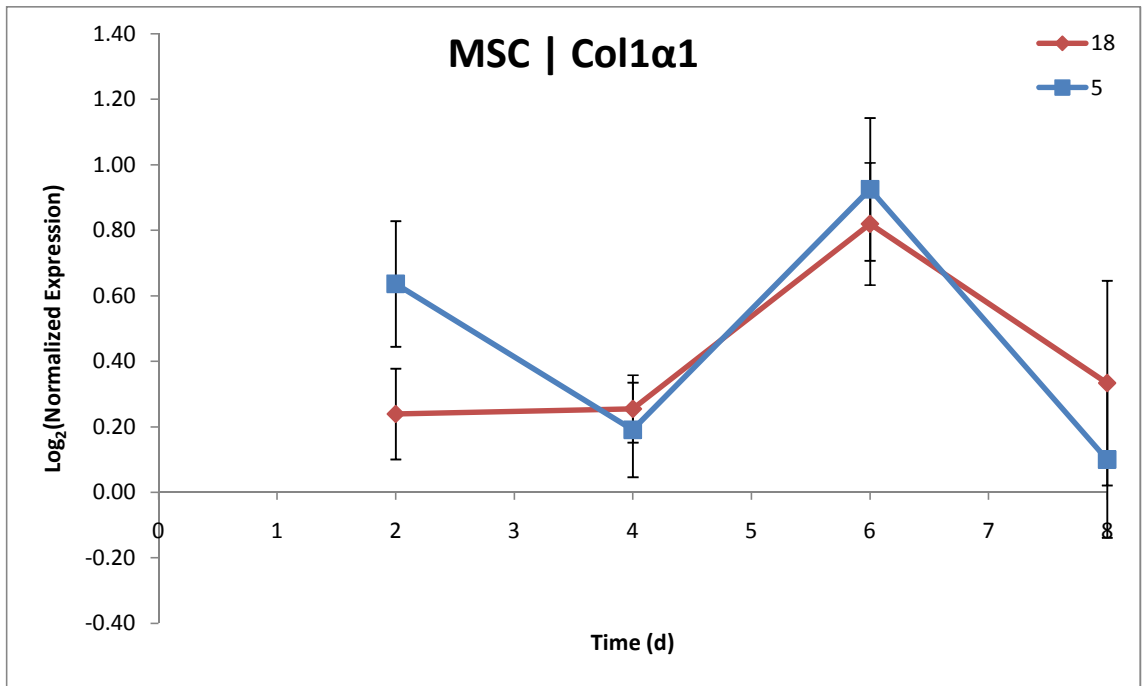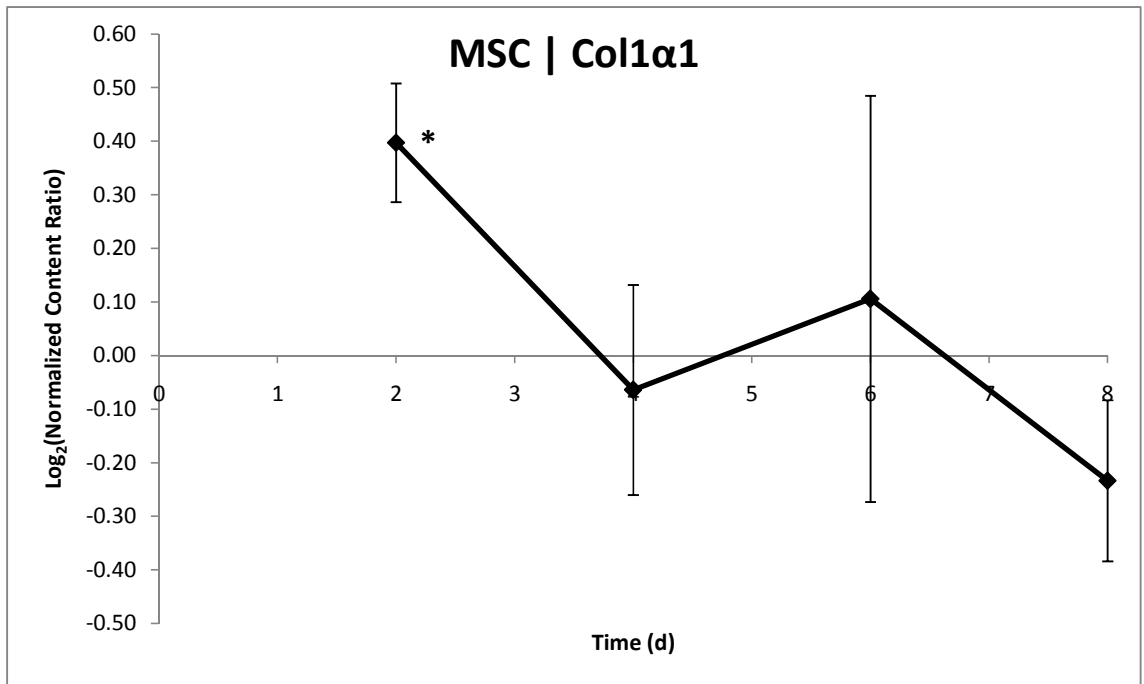
(a) Unpaired.

(b) Paired.

Figure 4.10: Col1α1 protein levels in MSCs under ϕ_{O_2} $(n = 5)$. p_{Col1} was determined normalized to an IRC.
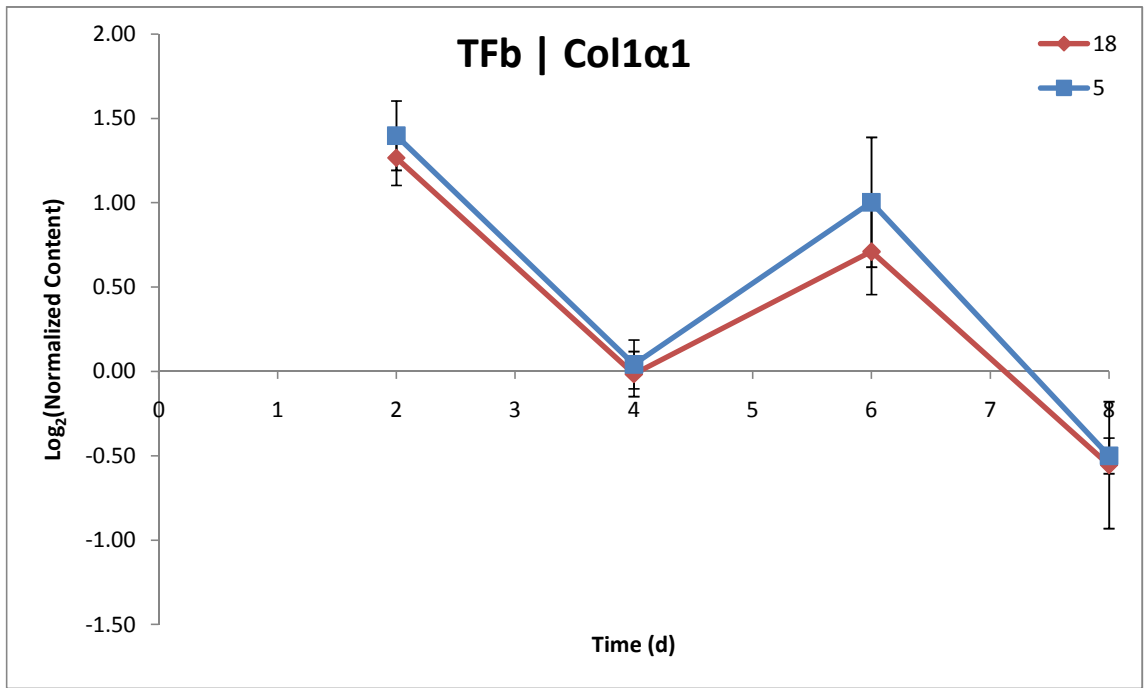
(a) Unpaired.
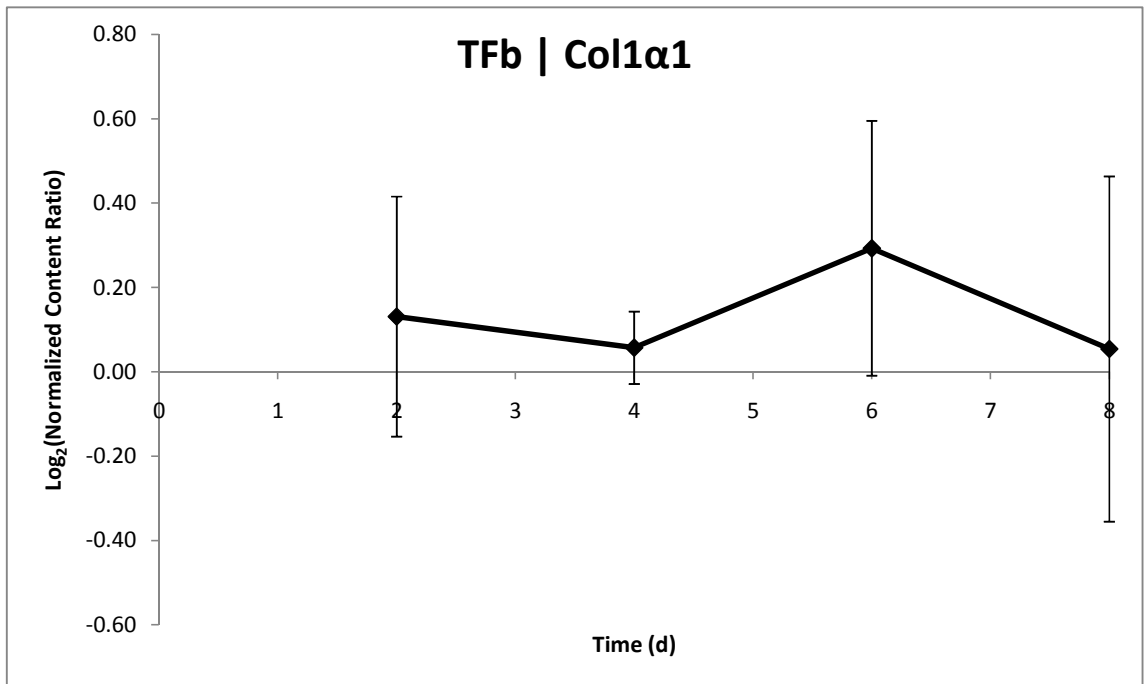
(b) Paired.

Figure 4.11: Col1α1 protein levels in TFbs under ϕ_{O_2} ($n = 5$). p_{Col1} was determined normalized to an IRC.

4.4 Discussion

The cell growth study revealed that MSCs have a lower population doubling time τ_{dbl} in hypoxia as compared to standard cell culture conditions when the plating density $\rho_0 \leq 10 \times 10^{3}\,\mathrm{cell/cm^2}$, with a ρ_0-dependent effect size $\Delta\tau_{\mathrm{dbl}}$. It should be noted that $20 \times 10^{3}\,\mathrm{cell/cm^2}$ is the plating density required for reliable formation of our laboratory's engineered tendon [239] and ligament [256] constructs, and this is the only ρ_0 at which there was no effect of hypoxia on growth rate. Furthermore, TFbs exhibited little to no variation between gaseous conditions, with the calculated $\Delta\tau_{\mathrm{dbl}}$ 10 to 100 times smaller than that of MSCs (Fig. 4.4b versus Fig. 4.2b). As mentioned above, τ_{dbl} and ρ_0 are expected to be positively correlated since there are a greater quantity of cells competing for the same number of resources. This bore out for all TFbs and MSCs under hypoxia, but normoxic MSCs actually grew *more* rapidly as ρ_0 increased. Here, it appears that hypoxia may have removed this reverse ρ_0-dependent behavior in MSCs. Interestingly, at very low plating densities ($\rho_0 \leq 16\,\mathrm{cell/cm^2}$), rat-derived MSCs have been shown the opposite: more yield with a lower ρ_0 [248].

All other things equal, the objective with regard to cell growth in a tissue-engineering context is to have the maximum number of functioning cells in order to minimize cell expansion and construct formation times *in vitro*. For this reason, the proliferative fraction (the proportion of actively dividing cells) was not considered critical in the current study. While the subtle (but statistically significant) changes in measured growth rate do not indicate cell-cycle changes, the qualitatively-distinct τ_{dbl}-ρ_0 behavior in MSCs in differential culture suggests a possible shift in mechanism.

Short-term (24 h) experiments were conducted as a first approximation of gene ex-

pression responses to 5% ϕ_{O_2} . These experiments showed quite clearly that MSCs initially react to this level of hypoxia by increasing the transcription of genes required produce the structural proteins of the tendon and ligament ECM, collagen I and elastin (Fig. 4.5a). The message level of *Scx*, however, remained unchanged. Interestingly, there is a significant reduction in *Scx* in adult TFbs exposed to short-term hypoxia (Fig. 4.5b).

While not directly comparable to the $24\,\text{h}$ data, the time course of MSC *Col1a1* differential expression appears consistent, upregulation peaking first at $t = 2\,\text{d}$ and again at $6\,\text{d}$, with no differential expression between or afterward (Fig. 4.6b). In contrast, the course of *Scx* differential expression over $8\,\text{d}$ is parabolic rather than oscillatory, demonstrating a transient upregulation under hypoxia that disappeared by the end of the experiment (Fig. 4.8b). The kinetics of TFb *Col1a1* expression are similarly biphasic as MSCs, but are shifted "downward" and actually result in suppression of *Col1a1* expression on days 4 and 8 (Fig. 4.7b). *Scx* levels in TFbs are also significantly upregulated in the middle of the time course (Fig. 4.6b). As *Col1a1* expression is a *downstream* target of Scx activity, these results are counterintuitive: *Scx* upregulation, if any, should precede *Col1a1* elevation, yet the opposite is observed here. Of course, it is possible that the sampling frequency is inappropriate, but the time scale of *Col1a1* and *Scx* variation appear consistent. Here, it should be reiterated that the role of Scx has not been well-studied in adult tissue. However, there is growing evidence that *Scx* expression is correlated with MSC commitment to a fibrogenic lineage at the exclusion of other mesenchymal lineages. In this case, like the transient upregulation of MyoD in myoblast differentiation, the role and appearance of Scx may be different in TFbs than that of MSCs. Indeed, the differing *Col1a1* histories with qualitatively similar *Scx* kinetics may in fact reflect a differential coupling of the

Scx-Col1α1 systems between the TFb, a (largely) terminally-differentiated cell, and MSCs, which have a known significant progenitor-cell subpopulation. Importantly, the product of early Col1α1 upregulation was confirmed by immunoblot (Fig. 4.10). While these outcomes do not directly measure the amount of secreted, stable Col1 in the monolayer ECM, it does suggest the beginning of an ECM secretory program under hypoxia. Likewise, the disappearance of Col1α1 or *Col1a1* elevation at later time points does not necessarily preclude the preservation of mature ECM Col1 induced by the early mRNA and protein spikes.

Additionally, it is worth noting that these studies aimed on initial growth and remodeling in a TE context. Given the rapid transcriptional response to external signals, a comprehensive investigation of the biology of MSC/TFb hypoxia would consider the time course of expression under 24 h. This is especially important since cell confluence, evident at 6 d and 4 d for MSCs and TFbs, respectivley (Table 4.5 and Table 4.6), can have a profound effect on cultured-cell behavior. This early-term behavior would also give insight into the *Scx-Col1* interaction that was not observable at 24 h.

Engineered-tissue technologies and mammalian cell culture exist in a complex milieu of soluble and insoluble factors, of which this study has primarily addressed the contribution of ϕ_{O_2} toward fibrogenesis. It is unknown what effect these treatments have on the expression of adipogenic (PPARγ, lipoprotein lipase), chondrogenic (aggrecan, collagen II), or osteogenic (alkaline phosphatase, osteocalcin) markers. Furthermore, it would be ideal if the results involving MSC upregulation of Col1 production could be repeated even in the presence of conflicting signals (i.e., known adipogenic or chondrogenic growth factors). For example, D'Ippolito et al. [243] were able to inhibit indications of osteogenesis when culturing MSCs in an osteogenic

120

(dexamethasone-containing) medium in $\phi_{O_2} = 3\%$. Such findings in the context of fibrogenesis cultured in 5% O_2 await further study.

The present investigation had primarily descriptive objectives with an eye toward optimizing engineered-tissue culture systems. The possible mechanisms behind the observed behaviors in response to lowered O_2 fall into three rough categories, no one of which is likely to operate in isolation: transcriptional activity by hypoxia-inducible factor-1 (HIF-1), the minimization of oxidative stress by cytosolic free radical reactive oxygen species (ROS), and the increased activity of membrane receptors and extracellular cytokines. HIF-1 mediates a variety of responses in different cell types of the body to oxygen deprivation including angiogenesis, erythropoiesis, vasodilation (though not in 2-D culture), as well as increased glycolytic enzyme activity. Dimerization of the α and β subunits enables the nuclear translocation of HIF-1 and its consequent transcriptional control. Active HIF-1 is itself controlled both transcriptionally and by the prolyl hydroxylase-dependent proteosomal degradation of the αsubunit [249]. In either of these scenarios, a direct cellular response to hypoxia could thus be determined by probing for the upregulation of *HIF-1α* or its encoded protein. Furthermore, treatment of MSCs with cobalt chloride(II), which mimics the effects of hypoxia by stabilizing HIF-1α [244, 246], could be used to additionally assess the similarity of responses observed in the current study.

Cytosolic superoxide anion ($O_2^{-\cdot}$) free radicals have numerous deleterious phenotypic effects. In $Sod1^{-/-}$ transgenic mice lacking the cytosolic Cu-Zn superoxide dismutase (CuZnSOD/SOD1) gene experience dramatic reductions in lifespan and muscle mass [257]. In cells not requiring high levels of aerobic metabolism, such as MSCs and TFbs, "normoxia" may actually cause adverse effects in cell culture such that "hypoxia" is associated with improved viability and function. Theoretically,

as part of ongoing studies on $Sod1^{-/-}$ mice in our laboratory, the experiments described here would be repeatable on wild-type and knockout mice. A non-additive amelioration of the ROS-induced phenotype and apoptosis in these cells beteeen ϕ_{O_2} levels would suggest a protective effect of culture hypoxia underlying the data of the present study. Unfortunately, no investigators to date have been able to successfully culture primary cells, even fibroblasts, from these animals. Current work, however, is underway to determine the feasibility of MSCs culture *ex vivo* isolated from $Sod1^{-/-}$ mice.

The current hypoxia levels could also indirectly contribute to the observed changes via the enhanced activity of extracellular signaling molecules or the potentiation of their associated cell-surface receptors. A two-factor experimental design varying a cytokine treatment and hypoxia state could elucidate if such an interaction exists or is in effect in cell culture. As an example, transforming growth factor β1 (TGF-β_1) is a disulfide-bond–linked homodimer but has little activity in monomeric form [237]. The O_2 saturation level can thus affect the oxidation-reduction state of the crosslink and its consequent biological activity for this and other factors in culture medium.

The inherent heterogeneity of MSCs purified solely by plastic adherence is an endemic difficulty encountered by investigators utilizing rodent cell culture. The immediate manifestations of this issue in the present work were the relatively large sample sizes needed and the need to employ paired *t*-tests (which have less statistical power) to obtain significant results. When contrasted with human MSCs, which do not exhibit such marked variability between experiments or even between patients [256], the current findings may indirectly carry stronger implications for human regenerative medicine than would be otherwise. Moreover, in contrast to various soluble growth factors used in tissue engineering for MSC expansion and differenti-

ation *ex vivo*, 5 % incubator ϕ_{O_2} is neither expensive to implement nor carcinogenic to cells.

4.4.1 Conclusion

In summary, the 2-D culture of MSCs under moderate (5 %) hypoxia yielded favorable outcomes for the purpose of engineering collagenous soft tissue in several biological modalities when compared to standard culture conditions : cell populations double in as little as 67 % the time, genes encoding major structural ECM proteins are upregulated by 24 h of culture, *Col1a1* gene expression and intracellular Col1α1 protein levels continue to be significantly elevated in early culture, and the tendon and ligament-specific transcription factor *Scx* is transiently upregulated over the course of a week. While the growth rates between hypoxia and normoxia are not significantly different when employing the particular plating density $(20 \times 10^3 \, ^{\text{cell}}/_{\text{cm}^2})$ in current use in Skeletal Tissue Engineering Laboratory (STEL)'s protocols for ETC formation, the waiting time during expansion (which employs sparser plating), could be reduced in the future by up to *one-third*, saving almost 5 d. Additionally, early Col1α1 gene and protein elevations under hypoxia disappear by mid-week in an extended culture setting. So, while the precise implications of these findings toward tendon and ligament engineering nor the underlying biological mechanisms are not clear from these studies, the use of hypoxic culture represents a promising improvement in the current state of the art by the important measures of growth rate and fibroblastic differentiation of MSCs.

Appendix

This section includes supplementary data for RNA sample integrity, PCR product specificity, and immunoblots.

Table 4.9: Assessment of MSC RNA sample integrity by agarose gel electrophoresis for time-course study. Distinct upper and lower bands corresponding to respective 28S and 18S ribosomal RNAs indicate intact total RNA prior to reverse transcription.
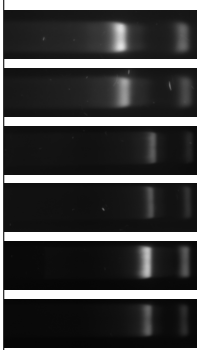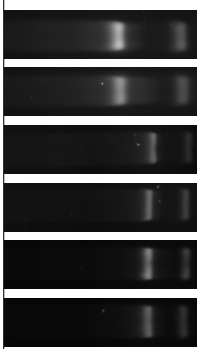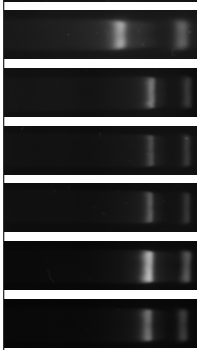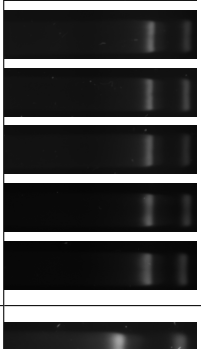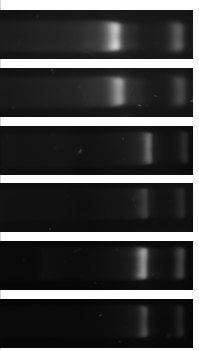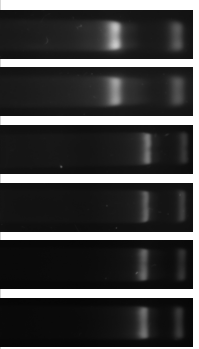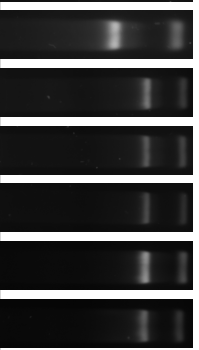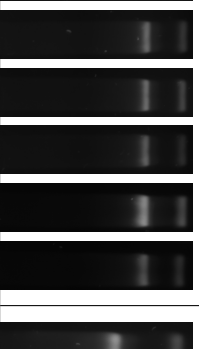
Table 4.10: Assessment of TFb RNA sample integrity by agarose gel electrophoresis for time-course study. Distinct upper and lower bands corresponding to respective 28S and 18S ribosomal RNAs indicate intact total RNA prior to reverse transcription.
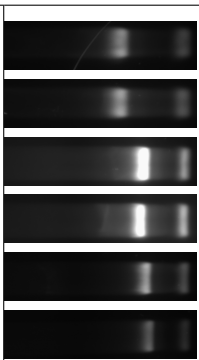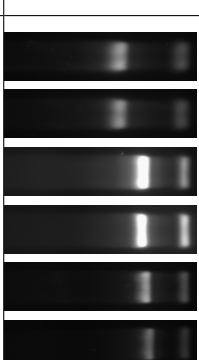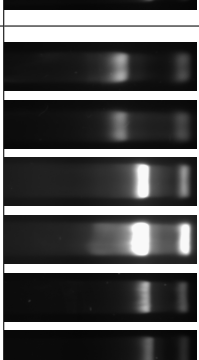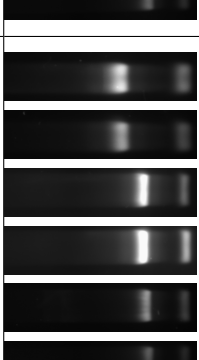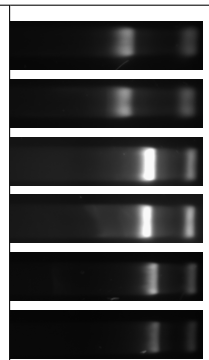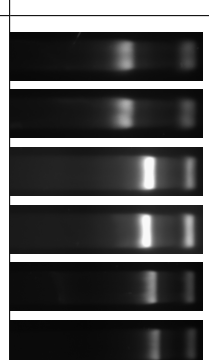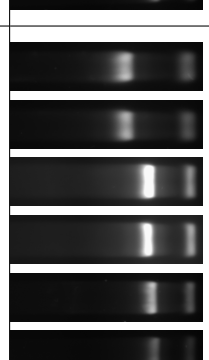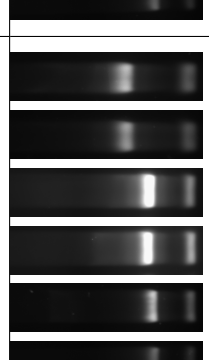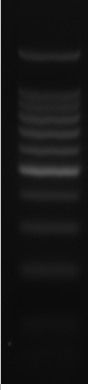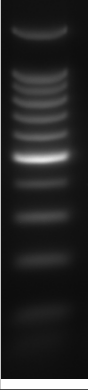
Table 4.11: Representative PCR product specificity by DNA AGE during determination of target gene primer-pair efficiency.
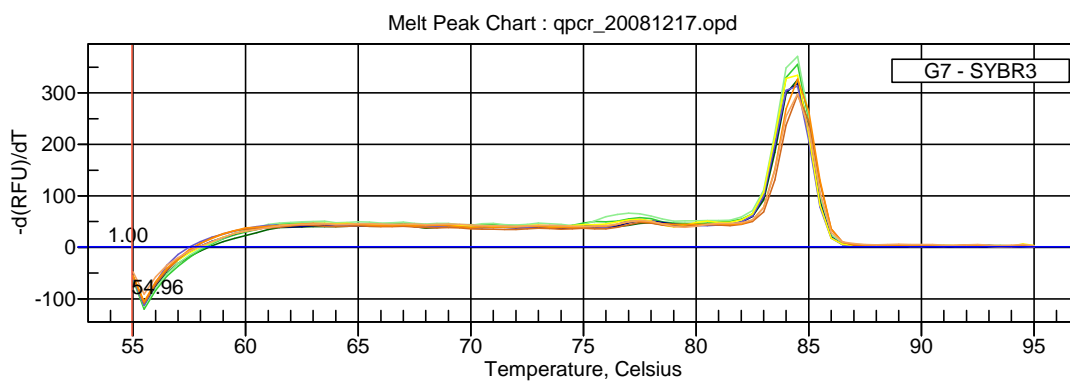
Gene	MW Std.	5 ng	25 ng	125 ng
Col1a1				
Eln				
Scx				
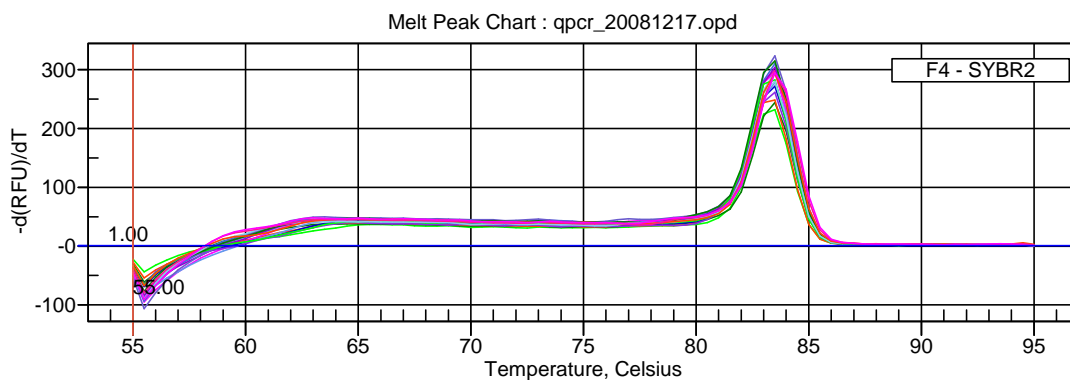
(a) *Col1a1*
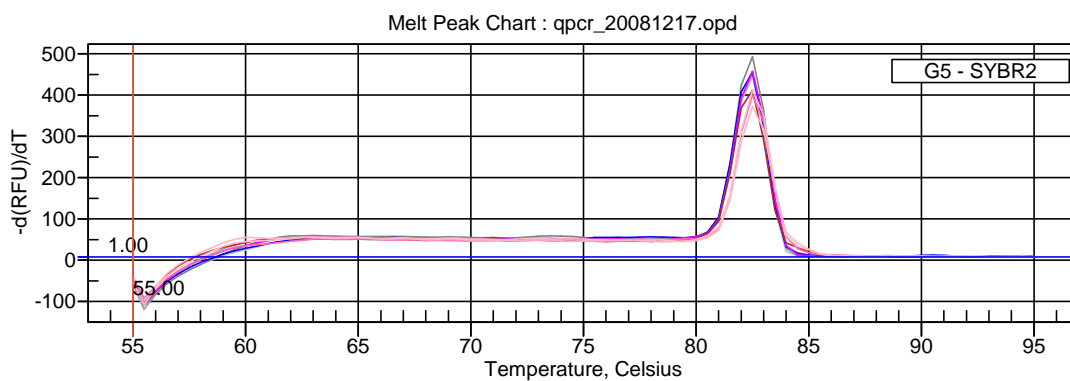
(b) *Eln*

(c) *Scx*

Figure 4.12: Representative qPCR melt curves demonstrating PCR product specificity during determination of target gene primer-pair efficiency.

Table 4.12: Representative PCR product specificity by DNA AGE for MSC gene expression under short-term differential ϕ_{O_2} culture.
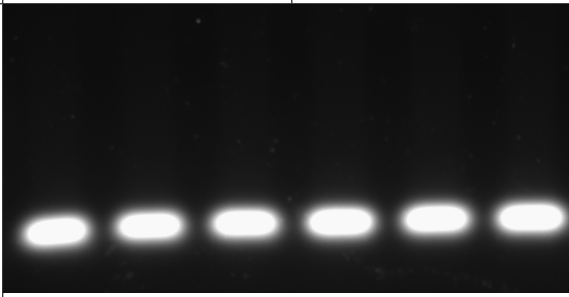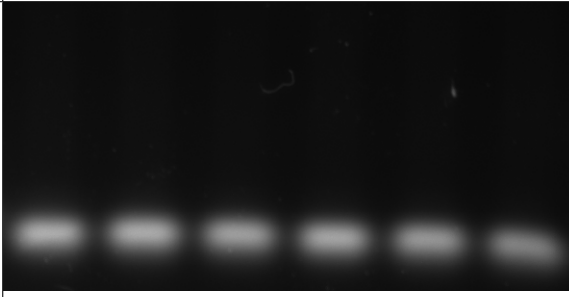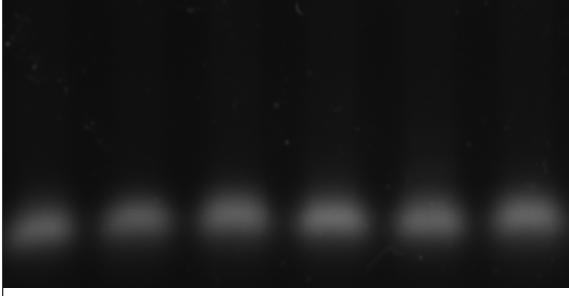
Gene	18 %	5 %
$\beta_2\text{-}\mu g$		
Col1a1		
Eln		
Scx		

Table 4.13: Representative PCR product specificity by DNA AGE for TFb gene expression under short-term differential ϕ_{O_2} culture.
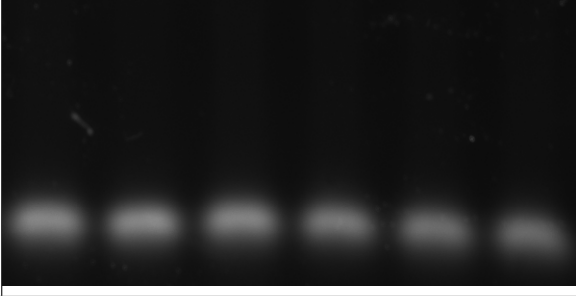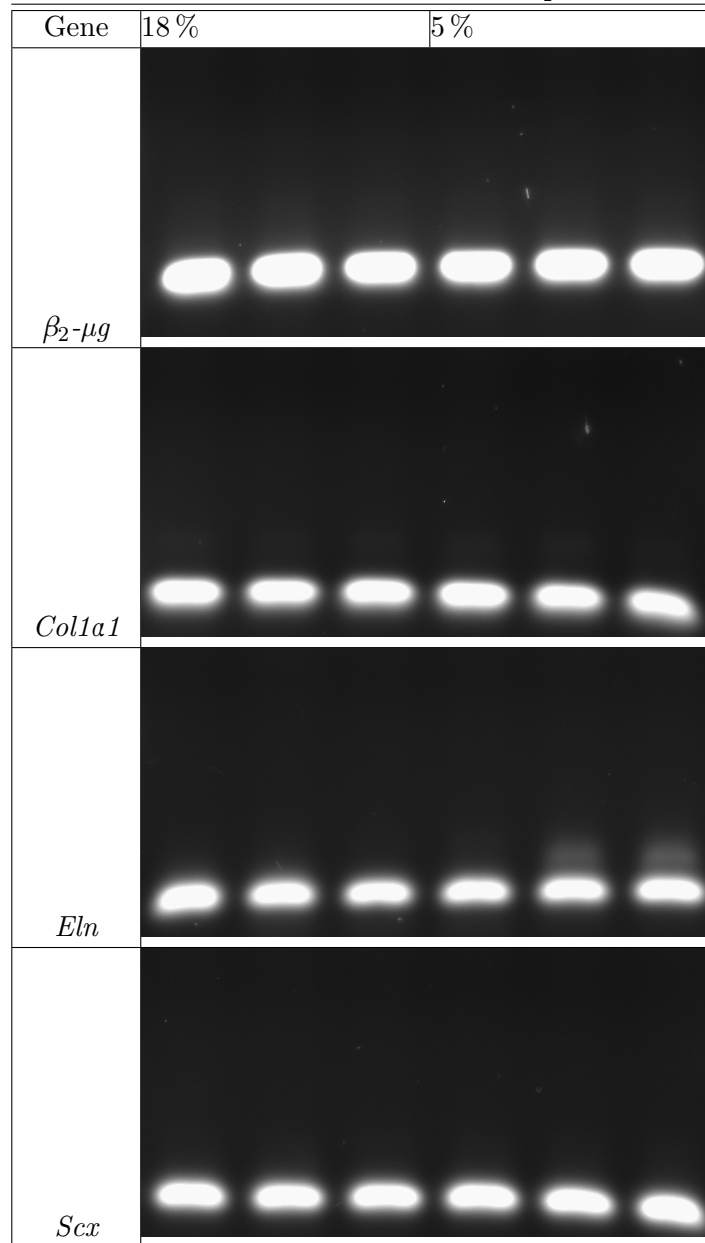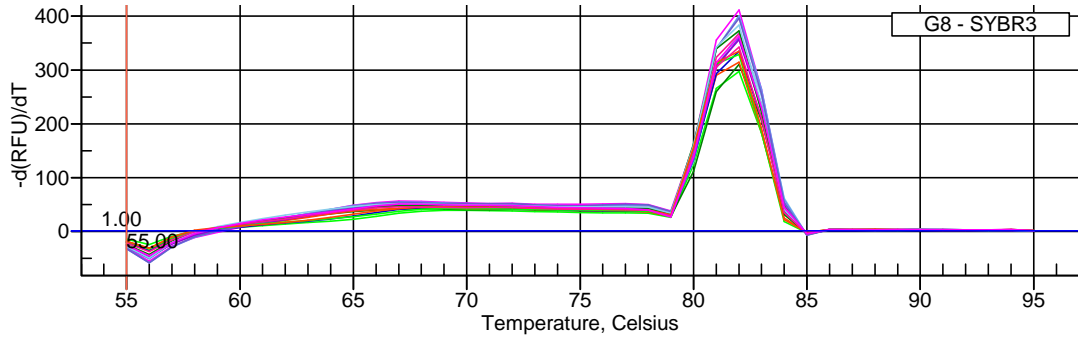

Gene	18 %	5 %
β_2-μg		
Col1a1		
Eln		
Scx		

(a) β_2-μg
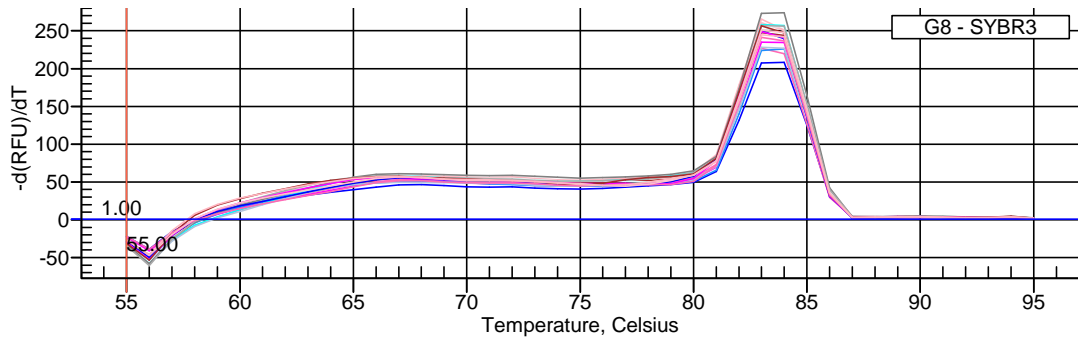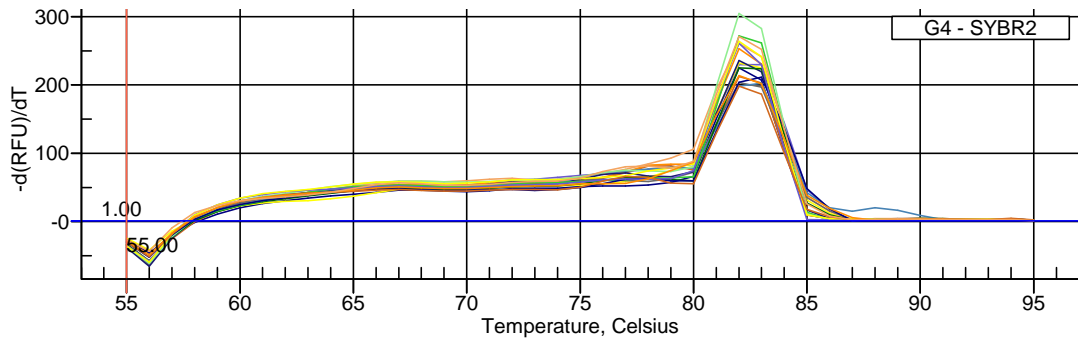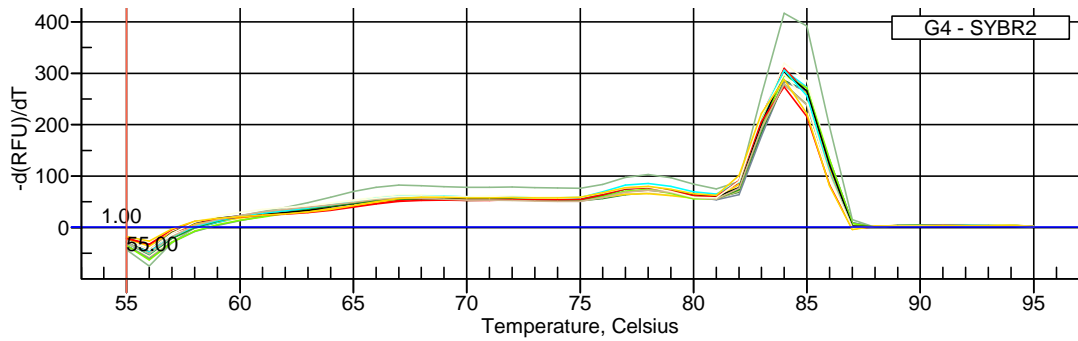
(b) *Col1a1*

(c) *Eln*

(d) *Scx*

Figure 4.13: Representative qPCR melt curves demonstrating PCR product specificity for short-term MSC gene expression experiments.

(a) β_2-μg
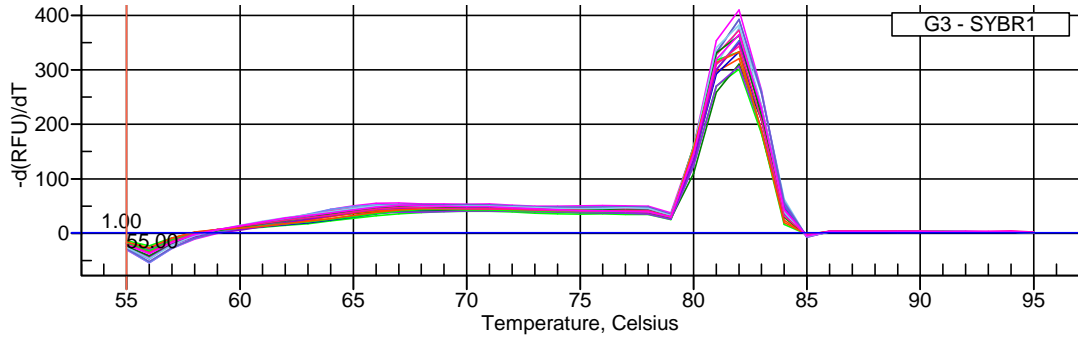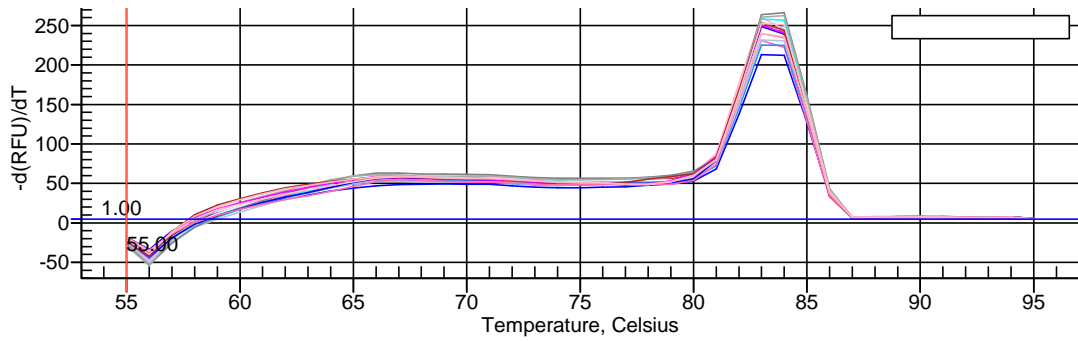
(b) *Col1a1*
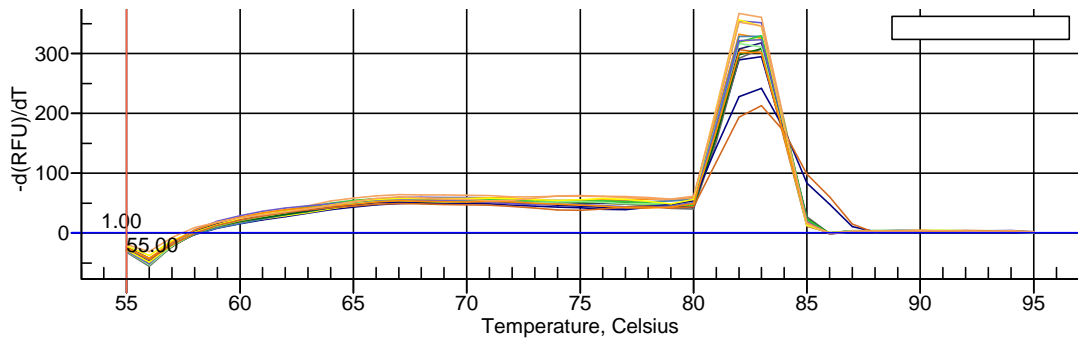
(c) *Eln*
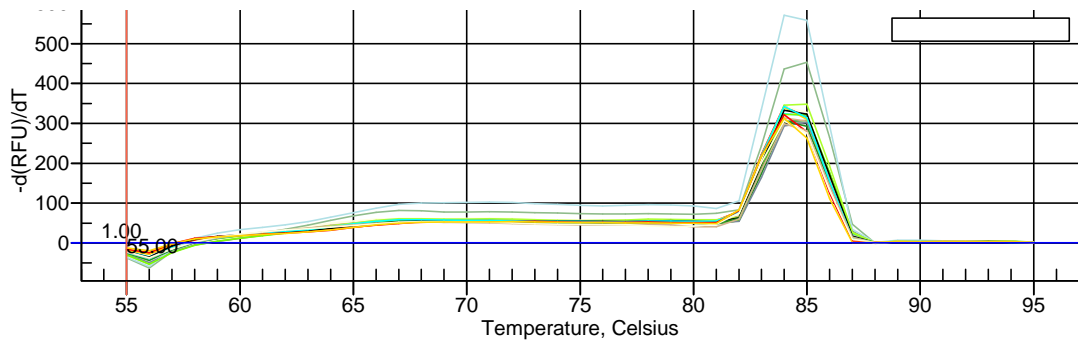
(d) *Scx*

Figure 4.14: Representative qPCR melt curves demonstrating PCR product specificity for short-term TFb gene expression experiments.

Table 4.14: Representative PCR product specificity by DNA AGE for MSC gene expression under extended differential ϕ_{O_2} culture.
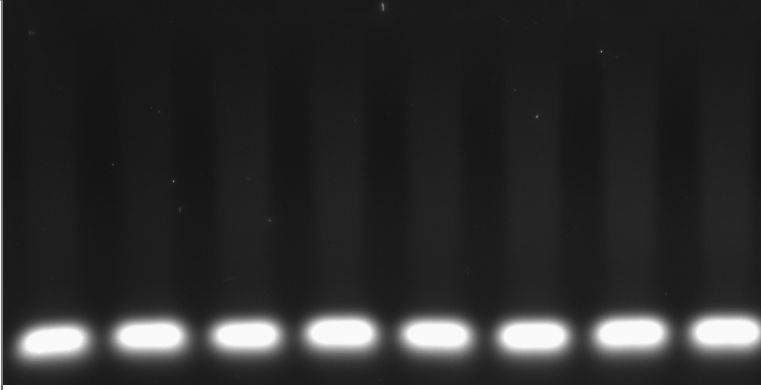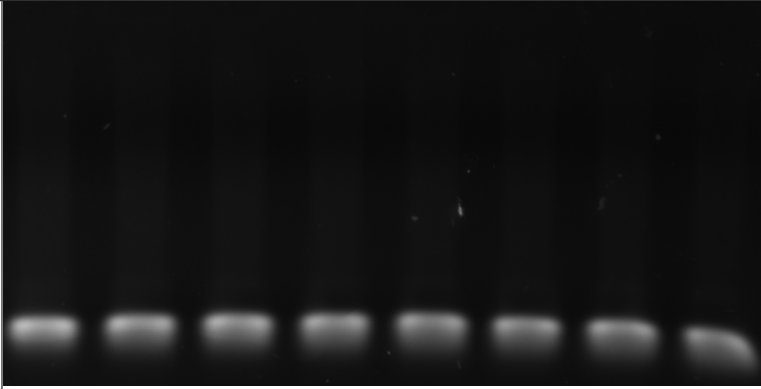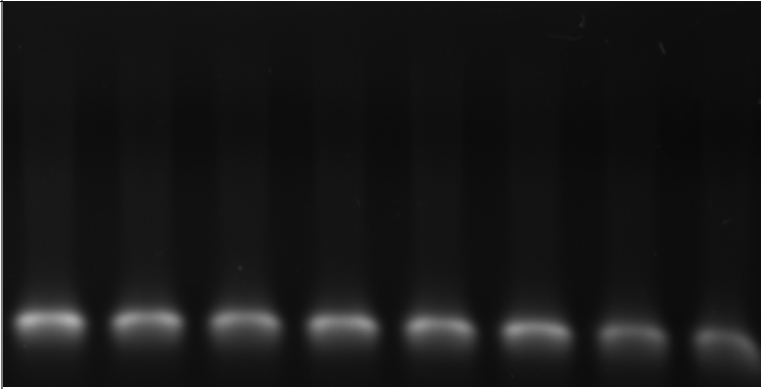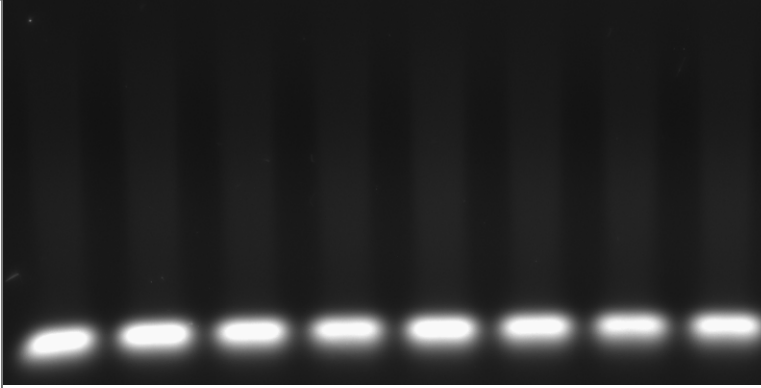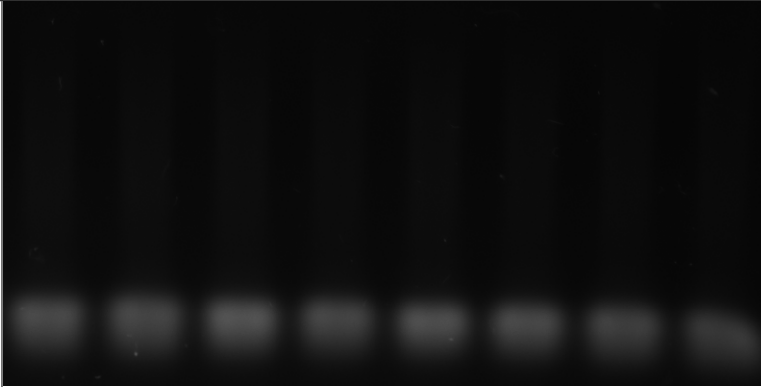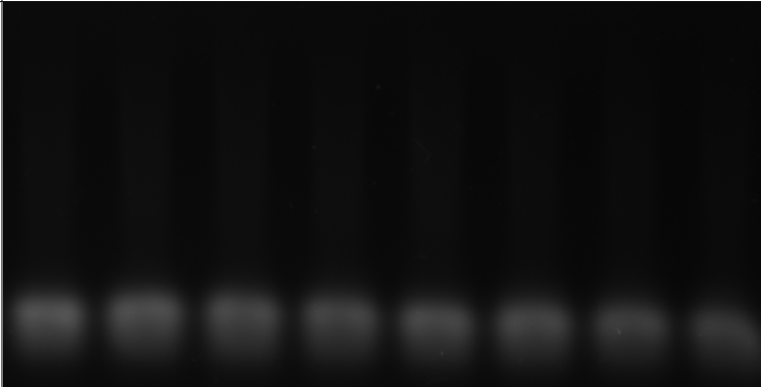
Gene	2 d		4 d		6 d		8 d	
	18 %	5 %	18 %	5 %	18 %	5 %	18 %	5 %
β-Act								
Col1a1								
Scx								

Table 4.15: Representative PCR product specificity by DNA AGE for TFb gene expression under extended differential ϕ_{O_2} culture.

| Gene	2 d		4 d		6 d		8 d	
	18 %	5 %	18 %	5 %	18 %	5 %	18 %	5 %
β-Act								
Col1a1								
Scx								

(a) *β-Act*

(b) *Col1a1*

(c) *Scx*

Figure 4.15: Representative qPCR melt curves demonstrating PCR product specificity for extended MSC gene expression experiments.

(a) *β-Act*
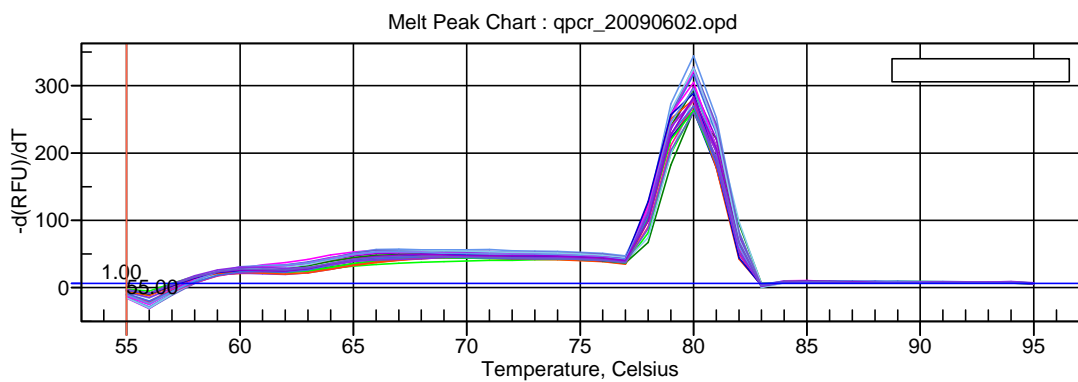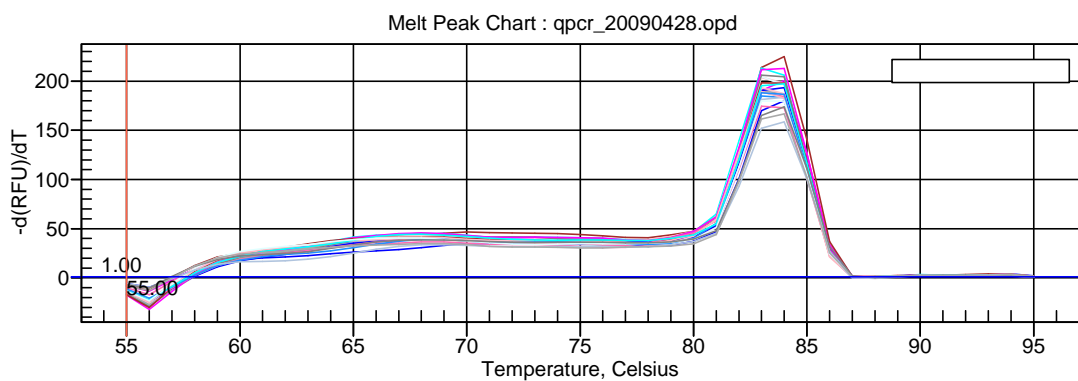
(b) *Col1a1*
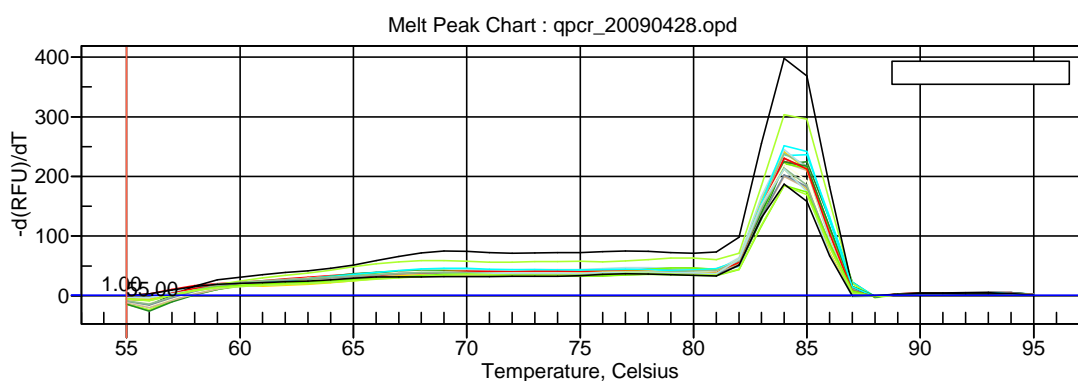
(c) *Scx*

Figure 4.16: Representative qPCR melt curves demonstrating PCR product specificity for extended TFb gene expression experiments.

Table 4.16: Comprehensive immunoblots for Collα1 target protein and β-Tub loading control in MSCs in time under differential ϕ_{O_2} .

t (d)	i	Protein	IRC	18%	5%	18%	5%	18%	5%	18%	5%	18%	5%	18%	MW (kD)
2	1	Collα1													150
		β-tub													55
	2	Collα1													150
		β-tub													55
4	1	Collα1													150
		β-tub													55
	2	Collα1													150
		β-tub													55
6	1	Collα1													150
		β-tub													55
	2	Collα1													150
		β-tub													55
8	1	Collα1													150
		β-tub													55
	2	Collα1													150
		β-tub													55

Table 4.17: Comprehensive immunoblots for Col1α1 target protein in TFbs in time under differential ϕ_{O_2} .

t (d)	i	Protein	IRC	18%	5%	18%	5%	18%	5%	18%	5%	18%	5%	MW (kD)
2	1	Col1α1												150
	2	Col1α1												150
4	1	Col1α1												150
	2	Col1α1												150
6	1	Col1α1												150
	2	Col1α1												150
8	1	Col1α1												150
	2	Col1α1												150

BIBLIOGRAPHY

[236] *FluroChem SP - AlphaEaseFC User's Manual.* Alpha Innotech Corporation, 2003. 99

[237] L. Attisano and J. L. Wrana. Signal transduction by the TGF-beta superfamily. *Science*, 296(5573):1646–1647, 2002. 122

[238] *iQ5 Optical System Software.* Bio-Rad Laboratories, 2.1 edition, 2005. 94

[239] S. Calve, R. G. Dennis, P. E. Kosnik, K. Baar, K. Grosh, and E. M. Arruda. Engineering of functional tendon. *Tissue Engineering*, 10(5-6):755–761, 2004. 86, 118

[240] D. C. Chow, L. A. Wenning, W. M. Miller, and E. T. Papoutsakis. Modeling pO(2) distributions in the bone marrow hematopoietic compartment. I. Krogh's model. *Biophysical Journal*, 81(2):675–684, Aug 2001. 83

[241] M. Csete. Oxygen in the cultivation of stem cells. In J. Ourednik, V. Ourednik, Sakaguchi D. S., and NilsenHamilton M., editors, *Stem Cell Biology: Development and Plasticity*, volume 1049 of *Annals of the New York Academy of Sciences*, pages 1–8. New York Acad Sciences, New York, 2005. doi: {10.1196/annals.1334.001}. 83

[242] M. Csete, J. Walikonis, N. Slawny, Y. W. Wei, S. Korsnes, J. C. Doyle, and B. Wold. Oxygen-mediated regulation of skeletal muscle satellite cell proliferation and adipogenesis in culture. *Journal of Cellular Physiology*, 189(2):189–196, Nov 2001. 83

[243] G. D'Ippolito, G. A. Howard, B. A. Roos, and P. C. Schiller. Isolation and characterization of marrow-isolated adult multilineage inducible (MIAMI) cells. *Experimental Hematology*, 34(11):1608–1610, Nov 2006. 120

[244] A. C. R. Epstein, J. M. Gleadle, L. A. McNeill, K. S. Hewitson, J. O'Rourke, D. R. Mole, M. Mukherji, E. Metzen, M. I. Wilson, A. Dhanda, Y. M. Tian, N. Masson, D. L. Hamilton, P. Jaakkola, R. Barstead, J. Hodgkin, P. H. Maxwell, C. W. Pugh, C. J. Schofield, and P. J. Ratcliffe. C-elegans EGL-9 and mammalian homologs define a family of dioxygenases that regulate HIF by prolyl hydroxylation. *Cell*, 107(1):43–54, OCT 5 2001. 121

[245] J. L. Grant and B. Smith. Bone marrow gas tensions, bone marrow blood flow, and erythropoiesis in man. *Annals of Internal Medicine*, 58(5):801–, 1963. 83

[246] V. T. Ho and H. F. Bunn. Effects of transition metals on the expression of the erythropoietin gene: Further evidence that the oxygen sensor is a heme protein. *Biochemical and Biophysical Research Communications*, 223(1):175–180, Jun 1996. 121

[247] J. G. Hunter, M. F. van Delft, R. A. Rachubinski, and J. P. Capone. Peroxisome proliferator-activated receptor gamma ligands differentially modulate muscle cell differentiation and MyoD gene expression via peroxisome proliferator-activated receptor gamma -dependent and -independent pathways. *Journal of Biological Chemistry*, 276(41), Oct 2001. 83

[248] E. H. Javazon, D. C. Colter, E. J. Schwarz, and D. J. Prockop. Rat marrow stromal cells are more sensitive to plating density and expand more rapidly from single-cell-derived colonies than human marrow stromal cells. *Stem Cells*, 19(3): 219–225, 2001. 118

[249] W. G. Kaelin. How oxygen makes its presence felt. *Genes & Development*, 16 (12):1441–1445, JUN 15 2002. doi: {10.1101/gad.1003602}. 121

[250] A. Kessinger and J. G. Sharp. The whys and hows of hematopoietic progenitor and stem cell mobilization. *Bone Marrow Transplantion*, 31(5), Mar 2003. 83

[251] H. Kofoed, E. Sjøntoft, S. O. Siemssen, and H. P. Olesen. Bone-marrow circulation after osteotomy - Blood-flow, pO$_2$, pCO$_2$, and pressure studied in dogs. *Acta Orthopaedica Scandinavica*, 56(5):400–403, 1985. 83

[252] R. Langer and J. P. Vacanti. Tissue engineering. *Science*, 260(5110):920–926, May 1993. 82

[253] D. P. Lennon and A. I. Caplan. Isolation of rat marrow-derived mesenchymal stem cells. *Experimental Hematology*, 34(11):1606–1607, 2006. 86

[254] K. J. Livak and T. D. Schmittgen. Analysis of relative gene expression data using real-time quantitative PCR and the 2(T)(-Delta Delta C) method. *Methods*, 25(4):402–408, Dec 2001. doi: {10.1006/meth.2001.1262}. 94, 96

[255] O. H. Lowry, N. J. Rosebrough, A. L. Farr, and R. J. Randall. Protein measurement with the folin phenol reagent. *Journal of Biological Chemistry*, 193 (1):265–275, 1951. 97

[256] J. Ma, K. Goble, M. Smietana, T. Kostrominova, L. Larkin, and E. M. Arruda. Morphological and functional characteristics of three-dimensional engineered bone-ligament-bone constructs following implantation. *Journal of Biomechanical Engineering-Transactions of the ASME*, 131(10), OCT 2009. doi: {10.1115/1.4000151}. 82, 118, 122

[257] F. L. Muller, W. Song, Y. H. Liu, A. Chaudhuri, S. Pieke-Dahl, R. Strong, T. T. Huang, C. J. Epstein, L. J. Roberts, M. Csete, J. A. Faulkner, and H. Van Remmen. Absence of CuZn superoxide dismutase leads to elevated oxidative stress and acceleration of age-dependent skeletal muscle atrophy. *Free Radical Biology And Medicine*, 40(11):1993–2004, Jun 2006. doi: {10.1016/j.freeradbiomed. 2006.01.036}. 121

[258] N. D. Murchison, B. A. Price, D. A. Conner, D. R. Keene, E. N. Olson, C. J. Tabin, and R. Schweitzer. Regulation of tendon differentiation by scleraxis distinguishes force-transmitting tendons from muscle-anchoring tendons. *Development*, 134(14):2697–2708, Jul 2007. 83

[259] S. Parrinello, E. Samper, A. Krtolica, J. Goldstein, S. Melov, and J. Campisi. Oxygen sensitivity severely limits the replicative lifespan of murine fibroblasts. *Nature Cell Biology*, 5(8), Aug 2003. 83

[260] M. W. Pfaffl. A new mathematical model for relative quantification in real-time rt-pcr. *Nucleic Acids Research*, 29(9), May 2001. 94

[261] K. Pruitt, T. Tatusova, and D. Maglott. *The Reference Sequence (RefSeq) Project*, chapter 18. National Library of Medicine (US), National Center for Biotechnology Information, Bethesda, MD, 2002. URL http://www.ncbi.nlm. nih.gov/bookshelf/br.fcgi?book=handbook. 93

[262] S. Rozen and H. Skaletsky. *Primer3 on the WWW for general users and for biologist programmers*, pages 365–386. Humana Press, Totowa, NJ, 2000. URL http://frodo.wi.mit.edu/primer3/. 92

[263] R. Schweitzer, J. H. Chyung, L. C. Murtaugh, A. E. Brent, V. Rosen, E. N. Olson, A. Lassar, and C. J. Tabin. Analysis of the tendon cell fate using scleraxis, a specific marker for tendons and ligaments. *Development*, 128(19):3855–3866, Oct 2001. 83

[264] Roche Applied Science. Universal ProbeLibrary for Rat, Universal ProbeLibrary Assay Design Center. URL http://qpcr.probefinder.com. 92

[265] M. J. Smietana, F. N. Syed-Picard, J. Ma, T. Kostrominova, E. M. Arruda, and L. M. Larkin. The effect of implantation on scaffoldless three-dimensional engineered bone constructs. *In Vitro Cellular & Developmental Biology-Animal*, 45(9):512–522, SEP 2009. doi: {10.1007/s11626-009-9216-3}. 82

[266] F. N. Syed-Picard, L. M. Larkin, C. M. Shaw, and E. M. Arruda. Three-dimensional engineered bone from bone marrow stromal cells and their autogenous extracellular matrix. *Tissue Engineering Part A*, 15(1):187–195, Jan 2009. doi: {10.1089/ten.tea.2007.0140}. 82

[267] S. N. Twigger, M. Shimoyama, S. Bromberg, A. E. Kwitek, H. J. Jacob, and RGD Team. The rat genome database, update 2007 - Easing the path from disease to data and back again. *Nucleic Acids Research*, 35(SI):D658–D662, Jan 2007. doi: {10.1093/nar/gkl988}. 93

CHAPTER 5

Conclusion

5.1 Summary

This dissertation described the development and investigation of theoretical and experimental models of growth and remodeling critical to scaffold-less, self-assembling biological soft tissue engineering.

5.1.1 Fiber reorientation and fusion (Chap. 2)

In the first study, the thermodynamics of a common class of fiber remodeling (including both reorientation and fusion) laws were investigated in detail. Working from first principles with minimal assumptions, it was found that purely mechanical formulations of remodeling that effect stiffening of the tissue inherently violate the reduced dissipation inequality and are thus thermodynamically inadmissible. A chemical energy term accounting for this imbalance, possibly provided by the explicit inclusion of a cell species, is at the very least required. This dissipation imbalance, termed the remodeling power, was quantified during the solution of the associated initial-boundary–value nonlinear elasticity problem with a 3-D cylindrical geometry representing a tendon undergoing uniaxial-stretch–driven fiber reorientation. The remodeling power was positive under both displacement and load control boundary conditions. Furthermore, via geometric construction, conditions were established under which this representative reorientation law in question is maximally dissipative,

an attractive feature for mathematical models of inelasticity and continuum physics. Similarly, the convexity of the chosen strain energy function with respect to fiber remodeling was investigated under canonical deformation states. The importance of addressing these balance and inequality-law issues must be emphasized and is relatively standard procedure in the development of constitutive models. This brand of analysis for remodeling laws had, to the best of our knowledge, largely been ignored in the literature.

5.1.2 Image analysis methods for fiber direction quantification (Chap. 3)

Proper anisotropy is of utmost importance for nascent *in vitro* soft tissue constructs to maximize stiffness and strength with scant biological resources. Following the theoretical work of the aforementioned reorientation studies, appropriate methods are necessary for analyzing corresponding experimental data. A novel image processing algorithm was developed to quantify directionality in planar and volumetric image data for incorporation into such continuum mechanical models of anisotropy. Unlike most methods, this formulation does not require the identification of discrete fibers or cells, making it suitable for microscopy images of sub-optimal quality or resolution. With only a single length-scale parameter needed for input, the method was validated in 2D against representative synthetic images of known fiber distributions and preliminarily applied to isotropic and fibroblast-aligned collagen gels imaged using reflection-mode confocal laser scanning microscopy (CLSM) to demonstrate its 3-D capabilities. The developed software is also suitable for assessing anisotropy in 3-D scaffold-less soft engineered tissue contructs (ETCs) imaged by an appropriate method, such as serialized scanning electron micrographs. It appears to be the only texture–intensity-gradient method utilized in a fully 3-D context.

5.1.3 Effect of hypoxia on the fibrogenesis of bone marrow stromal cells (Chap. 4)

To investigate cell growth and remodeling within the monolayer phase of the scaffold-less ETC culture system for tendon and ligament, the effects of gaseous oxygen level were studied on the early growth and fibroblastic differentiation of marrow stromal cells (MSCs) with respect to cohort tendon fibroblasts (TFbs). MSCs demonstrated a significantly shorter population doubling time under hypoxic conditions (5% O_2) compared to normoxia (18% O_2) that was plating-density dependent, while TFb growth was not affected by O_2 level. Moreover, collagen I mRNA and protein levels increased significantly up to 2 d in hypoxic MSC culture, while TFbs upregulated collagen I gene expression throughout 8 d of hypoxic culture without significant changes in protein. Additionally, both cell types demonstrated elevated mRNAs encoding the tendon and ligament-associated transcription factor scleraxis from 4 d–6 d under hypoxia. Other studies have investigated the effects of hypoxia on MSCs and multipotent subpopulations *or* their response to other experimental variables on biological measures relevant to soft tissue engineering, but by combining the two, this work is unique in its parameter and outcome assessment. While hypoxia was not expected to have a direct effect on the reorientation brand of remodeling, a possible indirect link between ϕ_{O_2} level and reorientation could exist through the activity of proteins such as α-smooth muscle actin (α-SMA) known to induce tractional alignment in cell-seeded collagen gels and ETCs. Moreover, ϕ_{O_2} may also have a direct effect on collagen fibril fusion.

5.2 Future work and open issues

5.2.1 Fiber reorientation and fusion (Chap. 2)

The analysis presented in this dissertation regarding the thermodynamics of continuum mechanical models of biological remodeling establish restrictions and and guidelines but does not propose any models itself. Following these recommendations will require at the very least constitutive models for the chemical and strain energy storage of cells. Understanding the detailed thermodynamics of the cytoskeleton-cell-extracellular matrix (ECM) interactions will also require experimental data on cell metabolism and heat production during tractional fibril reorientation. Current work in our group is addressing these cell-level modeling issues for its integration with our tissue-scale formulation [269].

5.2.2 Image analysis methods for fiber direction quantification (Chap. 3)

A key feature of the described method is the gradient-of-gaussian low-pass filter. In this case, the filtered images represent solutions to the isotropic heat equation. More sophisticated approaches to image enhancing and/or denoising that allow for nonlinear and anisotropic diffusion exist [270, 271], as well vector-based models [272] These methods may allow for higher-quality filtering of the input images prior to the directional analysis.

While the validation established reliable detection of orientation distributions in 2-D, it remains to be seen whether fiber directions in 3-D space can be recovered with equivalent quantitative precision. This would require some effort in developing software for synthetic image-volume generation as well as significant computational resources to generate the volumes and run the analysis. Further still, a truly practical validation would entail the quantitative correlation of the microstructural anisotropy

(as determined by image analysis) of a test sample with its direction-dependent mechanical properties. This latter study would be especially challenging, since it is not known what the representative volume element should be in order for acquired and calculated data to be continuum-hypothesis–appropriate.

This work demonstrated only one possible 3-D application, that of collagen gels imaged by CLSM. It can readily be applied to CLSM-obtained 3-D datasets as diverse as colloidal suspensions of ordered and non-ordered anisometric rods [268] or, using micro computed tomography, the trabecular bone microstructure of mouse models of connective tissue disorders like Ehlers-Danlos syndrome.

There are also microscopy-specific issues that present opportunities for method refinement. The limited working distance of many high-magnification objectives often limits the maximum specimen thickness, but the scattering of light by the sample itself is generally quite significant. Ideally, these analysis tools should have an option to correct for this situation heuristically. Also, the confocal point spread function tends to cause elongation or axial "smearing" of specimen features. This method does not currently account for this phenomenon through deconvolution, but could be added as a pre-processing step programmatically or in a separate application.

5.2.3 Effect of hypoxia on the fibrogenesis of bone marrow stromal cells (Chap. 4)

MSCs grown at 5% ϕ_{O_2} doubled more rapidly than those at 5% at low and medium plating densities. As described before, however, it is worthwhile to assess the possible roles of proliferation and apoptosis behind the observed differential cell growth properties.

The hypoxia studies focused on expression kinetics over the course of a week, the time frame of monolayer growth our ETC system prior to administration of

differentiation medium and 3-D self-assembly. It is evident, however, that cultures of both MSCs and TFbs reach confluence long before 8 d. Additionally, in order to address the complex and non-intuitive results between *collagen I α1 (Col1a1)* and *scleraxis (Scx)* (§4.4), this same expression behavior needs to be examined over the course of hours, not days.

Broadly speaking, multiple overlapping cellular mechanisms potentially underlie the observed enhancement in MSC fibrogenesis under hypoxia. Most straightforwardly, the activity of hypoxia-inducible factor-1 (HIF-1) or its downstream targets could be testing in existing samples to confirm whether or not the cells actually recognize the 5 % as hypoxia. Regarding the role of reactive oxygen species (ROS), a two-factor study employing differential ϕ_{O_2} culture combined with wild-type and $Sod1^{-/-}$-derived MSCs that lack a key enzyme providing effective ROS protection would lend insight into the interaction between incubator ϕ_{O_2} and ROS. Unfortunately, few efforts to culture $Sod1^{-/-}$ have been successful. Finally, it would be useful to test for the redox potentiation of soluble growth factors or their associated membrane receptors; an interaction between ϕ_{O_2} and the absence/presence of a factor in culture would suggest at least one mechanism independent of a direct cellular response.

5.2.4 Effect of oxygen tension on the formation of self-assembling, parallel-fibered, three-dimensional engineered soft tissue by bone marrow stromal cells

This dissertation described studies investigating the effect of hypoxia on the monolayer expansion phase of an ETC *prior* to 3-D self-assembly (Fig. 5.1). Since the chief objective of tissue engineering (TE) efforts is to design and fabricate constructs that are functionally-equivalent, the most immediate and important work follow-

ing this dissertation is to evaluate ETCs fabricated under differential ϕ_{O_2} culture in terms of their overall composition, microstructural organization, and, above all, mechanical properties. These interrelated aspects are all critical to a tendon/ligament replacement that is physiologically appropriate, even if mechanically sound. In particular, the potential graft tissue must be conducive to repopulation by host cells for permanent incorporation. It also means that there should not be gain in mechanical stiffness or strength due to calcification in the soft tissue which would likely be at cost to the viscoelaticity crucial to proper tissue function. To subsume the 3-D tendon/ligament formation regime into the strategy of ϕ_{O_2} optimization along with 2-D fibrogenesis, it should be sufficient here to characterize early 3-D ETCs shortly after self-assembly, as the majority of the ECM synthesis occurs during the monolayer phase.

The difference between hypoxic and normoxic ETCs is qualitatively apparent. ETC cultured under hypoxia have a greater success rate than that under normoxia and are noticeably more robust during routine manipulations. Specifically, the elastic and viscoelastic mechanical properties of ETC would be determined by low–strain-rate cyclic uniaxial extension and stress relaxation, respectively (Fig. 5.2). Since the cells at the inner core of ETCs cultured in $5\%\ \phi_{O_2}$ are especially vulnerable to true hypoxia, it will be necessary to examine the viability of ETC by immunohistochemistry of the 3-D cross section. The ETC microstructural morphology would be further characterized by scanning electron microscopy. This would yield image data suitable for the 3-D anisotropy quantification methods described in Chap. 3. Finally, the compositional properties of the ETC would be evaluated in terms of hydroxyproline content [273], an imino acid present in proportion to the amount of mature, hydroxylated collagen in the construct.
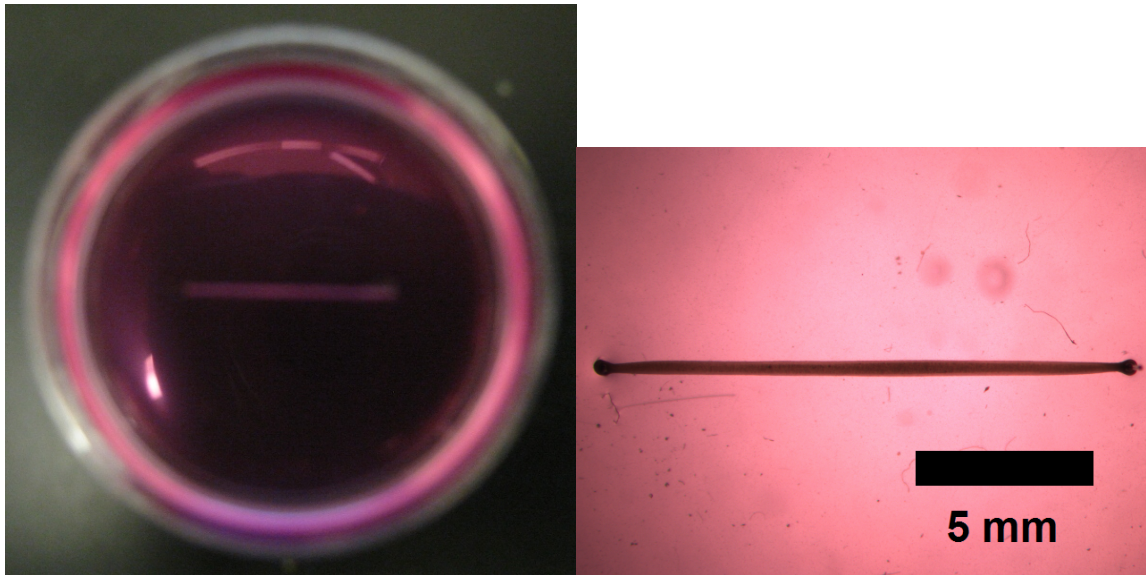
(a) Macro view. (b) Micro view.
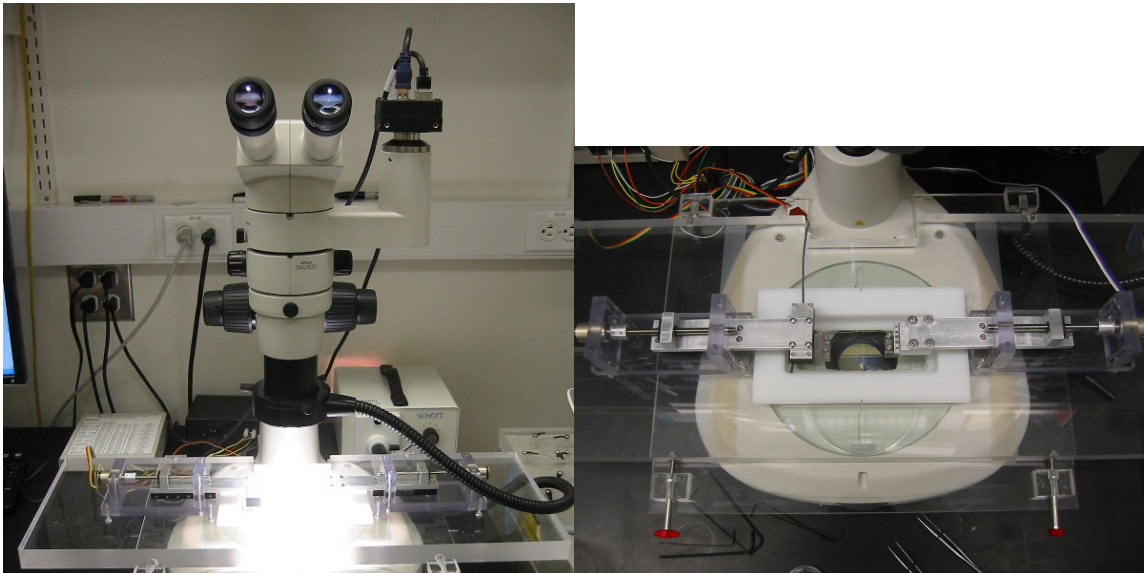
Figure 5.1: Mature, MSC-derived, 3-D ETC.

Figure 5.2: High-resolution tensiometer for mechanical characterization of compliant and ultra-compliant native and engineered biological tissues with integrated dissecting microscope and digital camera for optical strain measurement.

5.3   Final remarks

This work has addressed the biological growth and remodeling of parallel-fibered soft tissue in multiple hierarchical and temporal contexts. Specifically, the results of the first study (Chap. 2) have and continue to inform the development and refinement of multiphysics, cell-based constitutive models of growth and remodeling in immature tissue [269]. The kinetics of hypoxic exposure studied in Chap. 4 can further be used to design rate laws for chemical and protein deposition by cells in these models. In their computational implementation, these models can be extended to arbitrarily complex geometries and loading and boundary conditions necessary for individual patient design. Additionally, the image analysis methods (Chap. 3), combined with the suitable imaging modality could be used in the future to monitor the anisotropy of ETCs *ex* or *in vitro*, especially given the possibility of low image quality. Taken together, the ability to model and simulate complex cell and tissue behaviors—both computationally and experimentally—portends not only patient-specific engineered tissue therapies using "computer-aided tissue engineering", but also enables the testing of hypotheses related to important biological questions not directly approachable via conventional experiments.

BIBLIOGRAPHY

[268] A. Mohraz and M. J. Solomon. Direct visualization of colloidal rod assembly by confocal microscopy. *Langmuir*, 21(12):5298–5306, 2005. 146

[269] H. Narayanan, E. M. Arruda, K. Grosh, and K. Garikipati. The micromechanics of fluid-solid interactions during growth in porous soft biological tissue. *Biomechanics and Modeling in Mechanobiology*, 8(3):167–181, Jun 2009. doi: {10.1007/s10237-008-0126-1}. 145, 150

[270] P. Perona and J. Malik. Scale-space and edge-detection using anisotropic diffusion. *IEEE Transactions On Pattern Analysis And Machine Intelligence*, 12 (7):629–639, Jul 1990. 145

[271] L. I. Rudin, S. Osher, and E. Fatemi. Nonlinear total variation based noise removal algorithms. *Physica D*, 60(1-4):259–268, Nov 1992. 145

[272] J. Weickert. Theoretical foundations of anisotropic diffusion in image processing. *Computing Supplement*, 11:221–236, 1996. 145

[273] J. F. Woessner. Determination of hydroxyproline in tissue and protein samples containing small proportions of this imino acid. *Archives of Biochemistry and Biophysics*, 93(2):440–, 1961. 148